A Study of the $^{6}Li(\pi^{+},{}^{3}He)^{3}He$ Reaction at 60, 80 and 100 MeV

by

Brian James McParland
B.A.Sc., The University of British Columbia, 1979
M.Sc., The University of British Columbia, 1981

A THESIS SUBMITTED IN PARTIAL FULFILLMENT OF
THE REQUIREMENTS FOR THE DEGREE OF
DOCTOR OF PHILOSOPHY

in

THE FACULTY OF GRADUATE STUDIES
Department of Physics

We accept this thesis as conforming
to the required standard

22

THE UNIVERSITY OF BRITISH COLUMBIA
July, 1985

In presenting this thesis in partial fulfilment of the requirements for an advanced degree at the University of British Columbia, I agree that the Library shall make it freely available for reference and study. I further agree that permission for extensive copying of this thesis for scholarly purposes may be granted by the head of my department or by his or her representatives. It is understood that copying or publication of this thesis for financial gain shall not be allowed without my written permission.

Department of Physics

The University of British Columbia
1956 Main Mall
Vancouver, Canada
V6T 1Y3

Date July 11 /85

A Study of the $^6Li(\pi^+,{}^3He)^3He$ Reaction at 60, 80 and 100 MeV

Abstract

An experimental study of the pion-induced fission, $^6Li(\pi^+,{}^3He)^3He$, has been performed at TRIUMF using 60, 80 and 100 MeV pions. Angular distributions for this reaction at these energies, along with the energy dependence at fixed center-of-mass angles, are presented. Two theoretical models of this reaction predict widely differing angular and energy dependences. Prior to this experiment, the available data on the $^6Li(\pi^+,{}^3He)^3He$ reaction (and its inverse, $^3He(^3He,\pi^+)^6Li$) were insufficient to determine which of the two calculations better represent the reaction. The new data presented here have thoroughly tested these two models in this energy regime and have determined their suitability in their descriptions of the $^6Li(\pi^+,{}^3He)^3He$ reaction.

From these data (and from results previously published for the inverse $^3He(^3He,\pi^+)^6Li$ reaction at an equivalent pion energy of 15.4 MeV), the differential cross-sections were fit to an orthogonal Legendre polynomial series at each energy. These fits allowed the total cross-section to be extracted as a function of pion energy between 15.4 and 100 MeV. The total cross-section, and the center-of-mass differential cross-section at a fixed center-of-mass angle,

were found to exhibit an exponential decrease with pion energy over this range. The coefficients of these polynomial fits also clearly show the growing importance of higher-order partial-waves with increasing energy.

Finally, a phenomenological search for systematics in the world data of the $^{6}Li(\pi^{+},{}^{3}He)^{3}He$ and $^{3}He({}^{3}He,\pi^{+})^{6}Li$ reactions was made. This attempt was successful in finding a dependence of the reaction upon the spin-state of the exit channel which is similar to that previoulsly seen in (p,π^{+}) experimental data.

Table of Contents

List of Tables

List of Figures

Acknowledgments

The execution of a typical modern-day nuclear physics experiment usually demands the coherent effort of several physicists. The experiment described in this dissertation is no exception. My thesis supervisor, Ed Auld, offered much advice and guidance during the preparation of this experiment and in the data analysis and interpretation stages. Garth Jones' experience in experimental physics and electronics was a welcome help during the design and execution of the experiment. Many individuals contributed much time, expertise and effort during the preparation and data-collection periods : Fondas Aslanoglou, Geoff Bree, Pierre Couvert, Gord Giles, Dave Gill, Garth Huber, George Lolos (who originally proposed the experiment), Ishrat Naqvi, Dave Ottewell, Zisis Papandreou, Eric Szarmes, Pat Walden, Stan Yen and Bill Ziegler.

The apparatus used in this experiment was built by Charles Chan, Steve Chan, Chris Stevens and Ivor Yhap. Their expertise and help is gratefully acknowledged. I would also like to thank Dorothy Sample, who introduced me to the FIOWA software analysis package, and Jean Holt, who prepared the diagrams in this thesis, for their help.

One of the major functions of the work described in this thesis was to provide an experimental test of two theoretical models. Colin Wilkin (University College, London), Jean-Francois Germond (Universite de Neuchatel) and

Bernard Metsch (Universitat der Bonn) graciously provided the numerical results of their calculations.

On a more personal level, my parents have given much support in helping me to achieve the opportunity that this thesis represents. Their help cannot be adequately acknowledged.

My wife, Brenda, has provided the support and understanding often needed by a graduate student. I am deeply indebted to the inestimable patience that she has exhibited these past four years.

Finally, I would like to acknowledge the Natural Sciences and Engineering Research Council for providing financial support through IEP grant 74, and the University of British Columbia for awarding me a University Graduate Fellowship.

Brian J. McParland,
July, 1985,
Vancouver, B.C.

1 INTRODUCTION

Since the advent of the meson factories and their high intensity beams, more precise data on pion production and absorption reactions in nuclei have been accumulated. Because of these higher beam fluxes, it is now possible to make accurate measurements of the rare processes involving pions and nuclei. The study of such processes may provide some unique insight into the dynamics of the nucleus, and it is one of these low cross-section reactions that is the subject of this thesis.

Using the pion as a nuclear probe, or observing it as a reaction product, are potentially elucidating ways of extracting nuclear structure information. An extensive review of pion-nucleus interactions can be found in Eisenberg and Koltun [1980] and in the proceedings of the recent I.U.C.F. workshop [Bent, 1982].

Of particular relevance to the work described in this thesis are proton-induced pion production reactions from nuclei which leave the daughter nucleus in a bound state (exclusive production). Comprehensive reviews of the theoretical and experimental aspects of the $A(p,\pi)A+1$ reaction are given by Hoistad [1979], Measday and Miller [1979] and Fearing [1981]. If the resultant nucleus is left in a bound state, the reaction kinematics dictate that the momentum transfer be relatively large - ranging from about 400 to 1600 MeV/c at intermediate energies. As a

consequence, the (p,π) reaction will be a good probe of the high-momentum components of the nuclear wavefunction providing, of course, that the reaction mechanism is understood. Unfortunately, this mechanism is far from being completely understood and one now finds that the interest in the (p,π) reaction as a tool for nuclear structure study has been superseded by the interest in determining the nature of the reaction mechanism.

One empirical approach, in attempting to clarify the (p,π) mechanism, has been taken by groups at Orsay and Saclay which have looked at exclusive pion production using light nuclear projectiles (^{2}H and ^{3}He) rather than protons [Hibou, 1983]. These groups have expressed the hope that a study of these reactions (which transfer more than one nucleon to the nucleus) would yield some additional clues to understanding the (p,π) mechanism. A priori, however, such reactions would be expected to be rarer and more complicated than those with proton beams. Beyond (hopefully) improving the understanding of the (p,π) reaction, these exclusive (A,π) reactions are interesting in their own right, particularly when the bombarding beam energy is below that required for pion production in a free nucleon-nucleon interaction (about 290 MeV per bombarding nucleon). At such energies, pion production in these nucleus-nucleus collisions is termed as being 'subthreshold'.

In order for pion production to occur with the beam energy below the free NN -> NNπ threshold, the Fermi momentum of the struck nucleon must supply the extra energy

necessary to create a real pion. As the beam energy is further decreased, progressively higher Fermi momenta are demanded with the result being that far below the free NN -> NNπ threshold (125 MeV per bombarding nucleon, say), this nucleon-nucleon picture becomes insufficient to explain the pion production process. At 125 MeV per nucleon, more than just a single pair of nucleons from the projectile and target nuclei would be required to participate - the limiting condition of course being the coherent participation of all the nucleons. For the (p,π) case, which involves only a single nucleon projectile, this condition is termed 'singly coherent' production. When the projectile is a nucleus, and a pion is produced whilst leaving the daughter nucleus intact, the process is termed 'doubly coherent' production or 'pionic fusion' to reflect the combined involvement of the projectile and target nucleons [Shyam and Knoll, 1984]. This strict doubly coherent requirement would suggest a severely suppressed cross-section. Despite this, several experiments have been conducted which have detected such a pion production reaction. The following discussion shall be restricted to (A,π) reactions with deuteron, ^{3}He or ^{4}He beams; for subthreshold pion production with heavier projectiles, see the review lectures given by Rasmussen [1983] and the references therein.

Subthreshold inclusive (A,π) reactions, in which the pion is detected regardless of whether or not the final nucleus is bound, have been observed for almost forty years.

In fact, pions were first artificially produced in 1948 [Gardner and Lattes] at Berkeley by bombarding a variety of targets (copper, beryllium, carbon and uranium) with 300 and 380 MeV ^{4}He's. At these beam energies of 75 and 95 MeV per bombarding nucleon (or MeV/A), the pions were produced well below the free NN -> NNπ threshold. In the mid-1970's, Wall, et. al. [1976], observed the coherent production of neutral pions at Maryland using a ^{3}He beam. That group measured cross-sections for the ^{12}C(^{3}He,π^0)X and ^{208}Pb(^{3}He,π^0)X inclusive reactions at the 1 pb/sr-MeV level for 180 and 200 MeV ^{3}He's (or 60 and 67 MeV/A, respectively).

The first attempt to detect doubly coherent pion production was performed by Eggermann, et. al. [1975], at Julich. They irradiated a ^{181}Ta foil stack with 173 MeV ^{4}He's (or 43 MeV/A) and then radiochemically extracted the ^{185}Os that would have presumably been produced via the ^{181}Ta(^{4}He,π^-)^{185}Os reaction. The observed levels of ^{185}Os fixed the upper limit of the total reaction cross-section at 100 nb.

Further suggestive evidence for doubly coherent pion production was observed by Amann, et. al. [1978]. That group measured the ^{12}C(π^+,d)^{10}C reaction at 49.3 MeV with the ^{10}C nucleus left in either the 0^+ ground state or the 2^+(2.35 MeV) excited state. At a lab angle of 30°, the lab differential cross-section for both states was quoted as 650(±250) nb/sr. For the inverse reaction, ^{10}C(d,π^+)^{12}C, the deuteron energy would be 193.4 MeV (or 96.7 MeV/A). A few years later, deuteron-induced exclusive pion production was

directly observed at Saturne by Aslanides, et. al. [1982], who bombarded a ^{6}Li target with 300 and 600 MeV deuterons. Only the 300 MeV deuteron beam (150 MeV/A) was below the free NN -> NNπ threshold. The ^{6}Li(d,π^-)^{8}B reaction was measured by detecting the pions with a magnetic spectrometer. The measured cross-sections for the ground and first two excited states of ^{8}B were of the order of 100 pb/sr to 1 nb/sr and decreased with increasing deuteron energy.

The most comprehensive studies of doubly coherent pion production have been performed with ^{3}He projectiles. At CERN, Aslanides, et. al. [1979], bombarded a ^{6}Li target with 910 MeV ^{3}He's and detected the produced π^-'s at 0°. An enhancement in the π^- production spectrum at a specific pion momentum was attributed to the exclusive ^{6}Li(^{3}He,π^-)^{9}C reaction. Doubts raised by Nagamiya and Gyulassy [1984] about the statistical interpretation of this enhancement as being due to an exclusive reaction led the same group to repeat the experiment with an improved detection apparatus several years later [Bressani, et. al., 1984]. Evidence for the reaction was much more clearly seen at the same angle and incident energy. The double differential cross-section, $d^2\sigma/d\Omega\cdot dp$, at 0° was integrated over the pion momentum range corresponding to that expected for the pions from the ^{6}Li(^{3}He,π^-)^{9}C reaction. This integrated cross-section for the ^{9}C ground state and first excited state was 0.6(±0.25) pb/sr (a ^{7}Li target was also used in this latter experiment and an upper limit of 0.3 pb/sr for the

center-of-mass differential cross-section, $d\sigma/d\Omega^*$, of the $^7Li(^3He,\pi^-)^{10}C$(g.s.) reaction was obtained). In a similar experiment, at the same beam energy and lab angle, Aslanides, et. al. [1983], noted a similar production enhancement for the inclusive pion spectrum of the $^9Be(^3He,\pi^-)X$ reaction which could have been indicative of $^9Be(^3He,\pi^-)^{12}N$. The resolution was poor, but the integrated cross-section was again of the order of 1 pb/sr. Strictly speaking, though, the ^3He beam energy, at 303 MeV/A, was just slightly above the free NN -> NNπ threshold.

An extensive program for measuring doubly coherent pion production using a ^3He beam and various targets at energies far below the free NN -> NNπ threshold has been conducted during the past few years at Orsay. This program first began with measurements of the $^3He(^3He,\pi^+)^6Li$ reaction at 268.5 and 282 MeV (89.5 and 94 MeV/A) using a magnetic spectrometer to detect the pions [LeBornec, et. al., 1981]. The 1^+ ground state, and 3^+ and 0^+ excited states, of ^6Li were discernible and had reaction cross-sections of the order of tens of nb/sr. Using the Saturne ^3He beam, in a collaboration with Saclay, the Orsay group also measured the energy dependence of $^3He(^3He,\pi^+)^6Li$, for the 1^+ ground state and the 3^+ first excited state of ^6Li, for ^3He energies between 350 and 600 MeV at two fixed lab angles [LeBornec, et. al., 1983]. Over this energy range, the cross-section dropped by about an order of magnitude at a fixed angle. A rough survey of the dependence of the $(^3He,\pi^+)$ reaction upon the target's atomic mass number was performed using ^4He, ^6Li

and ^{10}B targets at ^{3}He energies between 235 and 282 MeV [Bimbot, et. al., 1982; Willis, et. al., 1984]. For ^{4}He, the reaction cross-section was of the same magnitude as that for the ^{3}He target, but dropped by approximately a factor of one thousand for the heavier targets. Finally, comparisons were made between the $(^{3}He,\pi^{+})$ and $(^{3}He,\pi^{-})$ exclusive reactions on ^{7}Li and ^{12}C at 235 MeV [Bimbot, et. al., 1984]. The π^{-} production cross-section was suppressed by about an order of magnitude relative to that for π^{+} production.

That doubly coherent pion production reactions with ^{3}He projectiles and light nuclear targets could occur with sizeable cross-sections had been hinted at by observations of the pionic capture process $^{6}Li(\pi^{-},^{3}H)^{3}H$, which is the charge-symmetric and time-reversed analog of the $^{3}He(^{3}He,\pi^{+})^{6}Li$ process. Cohen, et. al. [1965], measured a branching ratio of $2(\pm1) \times 10^{-4}$ for this fission channel. Minehart, et. al. [1969], later improved the value to $3.4(\pm0.5) \times 10^{-4}$. In a more recent experiment performed at SIN, Sennhauser, et. al. [1982], obtained a value of $6.5(\pm1.0) \times 10^{-4}$ for the branching ratio. No reason for the fact that this result was a factor of 2 to 3 times greater than those obtained from the earlier measurements was apparent.

Related $(\pi^{+},^{3}He)$ reactions resulting in two-body final states have been measured using ^{6}Li and ^{7}Li targets. Experiments employing this 'pionic fission' channel have significant advantages over those going in the time-reversed $(^{3}He,\pi^{+})$ 'pionic fusion' direction. These include a larger

reaction cross-section due to phase space and the attainment of comparatively higher center-of-mass energies for lower beam energies. Of course, the greatest disadvantage resides in the restriction of only the nuclear ground state being available for study. At LAMPF, Barnes, et. al. [1983], have measured the $^6Li(\pi^+,{}^3He)^3He$ and $^7Li(\pi^+,{}^3He)^4He$ reactions for pion energies of 39 and 59.3 MeV. Additionally, three-body final states resulting from π^+ absorption on the two lithium isotopes were also observed. The $^6Li(\pi^+,{}^3He)^3He$ pionic fission has also been measured at 60, 75 and 90 MeV at a single angle at TRIUMF [Lolos, et. al., 1983].

In addition to complementing the doubly coherent data obtained with ^3He beams, these $(\pi^+,{}^3He)$ reactions may also have some impact upon the study of pion absorption in nuclei. Due to the conservation of energy and momentum, a pion cannot be absorbed by a free nucleon. However, it is possible for a pion to be absorbed by a nucleon bound in a finite nucleus. If a pion with kinetic energy T_π and momentum p_π is absorbed in a nucleus and releases a single nucleon, the nucleon will have a kinetic energy,

$$T_N = p_N^2/2M = T_\pi + m - BE - T_{REC}$$

where p_N is the nucleon's momentum, M and m are the nucleon's and pion's rest-masses, respectively, and BE is the nuclear binding energy. T_{REC} is the recoil kinetic

energy of the daughter nucleus. The momentum transfer to the nucleon is,

$$\vec{q} = \vec{p}_N - \vec{p}_\pi$$

Since the pion only brings in a momentum $\vec{p}_\pi$, the nuclear potential must supply the remaining momentum $|\vec{q}|$ to the nucleon. As an example, for a stopped pion ($T_\pi = 0$) being absorbed on a single nucleon, the nuclear potential must supply, neglecting the binding and recoil kinetic energies,

$$|\vec{q}| = |\vec{p}_N| = \sqrt{(2Mm)} = 510 \text{ MeV/c}$$

Because this value is too large to expect for a single nucleon's Fermi momentum, it would be reasonable to conclude that the $A(\pi,N)A-1$ reaction would have a suppressed cross-section. If, instead, the pion was scattered off-shell from one nucleon and then absorbed on another, the momentum transfer per nucleon is reduced. For pion absorption on two correlated nucleons, the momentum supplied by the nuclear potential is of the order $\sqrt{(Mm)} = 360$ MeV/c per nucleon. This lower momentum transfer would make absorption on two nucleons more probable than that on a single nucleon.

There is considerable experimental evidence to suggest that pion absorption on even a nucleon pair may not be the most dominant mechanism [Schiffer, 1981, 1985]. McKeown,

et. al. [1980], have measured (π^+,p) and (π^-,p) inclusive reactions on ^{12}C, ^{27}Al, ^{58}Ni and ^{181}Ta for 100, 160 and 220 MeV pions and have concluded that the average number of nucleons involved ranges from 3 to about 6, with the number increasing with the size of the target nucleus. In another experiment, Altman, et. al. [1983], concluded that absorption upon a single correlated p-n pair (through the $\pi NN \rightarrow N\Delta \rightarrow NN$ chain) accounts for less than a quarter of the total absorption cross-section for $^{12}C(\pi^+,2p)$ at 165 and 245 MeV. In a review talk given at the recent tenth international conference on "Particles and Nuclei", Redwine [1985] describes other possible conclusions that can be made from these two experiments. For (π^+,^{3}He) reactions, the pion's momentum, by necessity, is transferred to at least three nucleons. Thus, these reactions could prove to be useful probes of the mechanism for pion absorption on more than two nucleons or, at the very least, provide experimental constraints for theories describing such a mechanism.

On the theoretical front, two independent attempts (detailed in the next chapter) have been made to explain the doubly coherent (^{3}He,π^+) reactions and their inverses and have been largely applied to the $^3He(^3He,\pi^+)^6Li$ and $^4He(^3He,\pi^+)^7Li$ reactions. The resulting models predict different energy and angular dependences for the reaction cross-sections. Prior to the work described in this thesis, there was a paucity of (^{3}He,π^+) and (π^+,^{3}He) data, especially in the energy regime above 300 MeV ^{3}He's for the

fusion direction or 24.5 MeV pions for the fission direction. Because of this scarcity of data, it was not possible to conclude which of the two models presented a more acceptable description of the reactions.

These higher energies are more readily attained by measuring the $(\pi^+,{}^3He)$ reaction. With this in mind, the work described in this dissertation was begun in the hope of obtaining the first measurements of the angular distribution of the ${}^6Li(\pi^+,{}^3He){}^3He$ reaction at pion energies of 60, 80 and 100 MeV. These pion energies correspond to 371, 411 and 451 MeV equivalent ${}^3He$ energies (or 124, 137 and 150 MeV/A).

It was decided to study the ${}^6Li(\pi^+,{}^3He){}^3He$ reaction for this thesis as it was its time-reversed analog, ${}^3He({}^3He,\pi^+){}^6Li$, that was the most extensively studied $({}^3He,\pi^+)$ reaction near threshold. A consistent and detailed examination of this particular reaction, in conjunction with the fusion data, offered the best prospect for a reasonable comparison to be made of the models.

In Chapter 2 of this dissertation, the two theoretical models that have been developed to describe the doubly coherent $({}^3He,\pi^+)$ reactions will be discussed. The experimental apparatus and techniques used in this work are detailed in Chapter 3. Chapter 4 outlines the analysis and results, and Chapter 5 presents the conclusions resulting from this thesis. Three appendices have also been included. Appendix A describes a quantitative calculation of the non-linear response of the NE-102 scintillator used in this experiment's detectors. Appendix B details a Monte Carlo

code developed for this experiment, and a particular pion beam normalization technique used in this work is described in Appendix C.

2 THEORETICAL CONSIDERATIONS OF ^{3}He-INDUCED DOUBLY COHERENT PION PRODUCTION

"The skeptics argued that if this coherence worked as advertised, the best way of making pions would be to drop an elephant into a pit - total energy well above threshold and a tremendous number of nucleons to act coherently"

-J.O. Rasmussen on coherent pion production in nucleus-nucleus collisions [1983]

Two models have been introduced to describe doubly coherent (^{3}He,π^+) reactions. The first of these is a microscopic calculation which assumes that the fundamental mechanism resides within the NN -> NΔ -> NNπ chain and explicitly couples this mechanism to the center-of-mass motion of the two approaching nuclei. The second model is phenomenological and takes a ^{3}He(p,π^+)^{4}He subprocess as its pion production mechanism and uses measured data for ^{3}He(p,π^+)^{4}He as input. The salient features of both of these models germane to ^{3}He(^{3}He,π^+)^{6}Li are reviewed in this chapter. Note that an asterisk "*" refers to a center-of-mass quantity, unless otherwise noted.

(2.1) A Microscopic Calculation : the Erlangen-Bonn Model

It would be natural to expect that in a nucleus-nucleus collision below the free NN -> NNπ threshold the incoming kinetic energy would simply be randomly distributed (thermalized) among all the nucleons. Experimental data,

however, have shown that such a collision can yield a pion. This phenomenon infers the existence of a highly coherent cooperation between the colliding nucleons. Consequently, a model for such a reaction must contain a specific mechanism that directly couples the kinetic energy of the entrance channel to the pion field. A microscopic calculation, developed by Huber and his colleagues at the University of Erlangen-Nurnberg and then at the University of Bonn, suggests that such a cooperative mechanism exists in the excitation of a nucleon to a Δ_{33} resonance during the collision. This Δ_{33} is free to propagate through the intermediate state and eventually decay to yield a pion [Klingenbeck, et. al., 1981; Huber, et. al., 1982, 1983; Hupke, et. al., 1984].

The premise behind the Erlangen-Bonn (EB) model is that the thermalization of the energy carried by the incoming nucleus among the nucleons' external degrees of freedom can be circumvented by funnelling the energy into a quark degree of freedom within a single nucleon. Specifically, if the collision was to induce a spin-isospin flip of a quark within either a projectile or target nucleon (creating a Δ_{33}), then the energy of the collision would be stored without heating up the intermediate state.

Figure (1) schematically represents the application of the model to the $^3He(^3He,\pi^+)^6Li$ reaction. The processes shown in this figure are described below.

Figure (1)

The Resonant Transition Amplitude
From the Erlangen-Bonn Model of
the $^3He(^3He,\pi^+)^6Li$ Reaction

(Terms in the figure are discussed in the text)

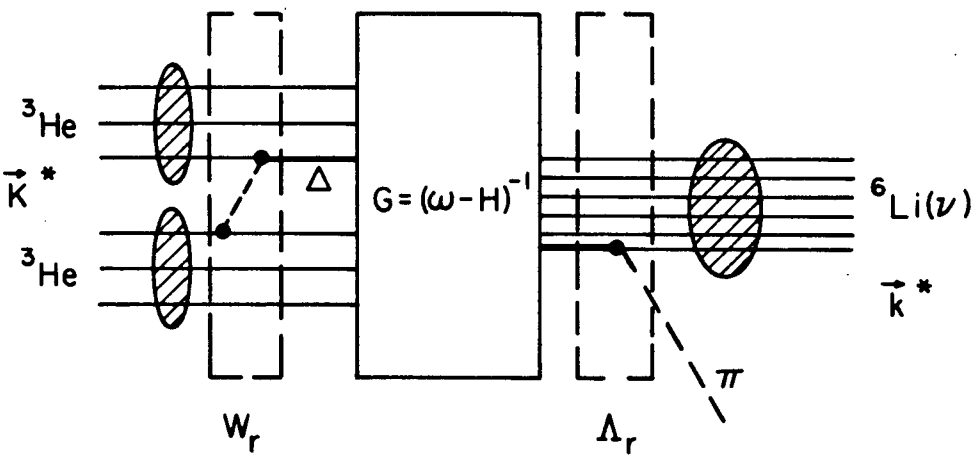

The transition matrix element for this reaction is,

$$T_{fi} = \langle {}^6Li(\nu),\pi^+; \vec{k}^* \mid T \mid {}^3He,{}^3He; \vec{K}^* \rangle \qquad (2.1)$$

where T is the transition matrix, $\vec{K}^*$ and $\vec{k}^*$ are the center-of-mass momenta of the ^{3}He and the pion, respectively, and ν represents the particular final state of ^{6}Li. The EB model separates the nuclear configuration space into one subspace that contains only nucleons and another that has at least one excited nucleon. This separation allows the transition matrix to be split into the corresponding resonant and non-resonant terms,

$$T = T_r + T_{nr} \qquad (2.2)$$

The most significant resonance created at intermediate energies is the Δ_{33} and it is the only one accounted for in the resonant term, T_r. The non-resonant term, T_{nr}, accounts for all the NN -> NNπ processes in which there is no Δ_{33} produced. As the NN -> NΔ -> NNπ chain is presumed to be dominant in this reaction, the non-resonant factors given in T_{nr} are neglected by the Erlangen-Bonn calculation. Restriction to the configuration space which contains a Δ_{33} serves to simplify the calculation. This simplification, though, produces an uncertainty in the model's results.

T_r is factorized in terms of the three processes shown in Figure (1),

$$T_r = \Lambda_r \; G \; W_r \tag{2.3}$$

The 'ignition' operator, W_r, describes the interaction between the two approaching ^{3}He nuclei and is the sum of the elementary NN -> NΔ interactions between all the nucleons in each nucleus,

$$W_r = \sum_{i=1}^{3} \sum_{k=1}^{3} w_{ik} \tag{2.4a}$$

The elementary NN -> NΔ interaction between nucleons 'i' and 'k', i.e., the emission of a virtual pion from nucleon 'i' and its absorption upon nucleon 'k' which is then raised to a Δ_{33}, is described by,

$$w_{ik} = (2\pi)^{-3}(ff^*/m_\pi^2) \int d^3\vec{q}\; \Gamma(\vec{q}) \exp(i\vec{q}\cdot\vec{r}_{ki}) \; \Sigma(\vec{q}) \tag{2.4b}$$

f and f* are the coupling constants for the NNπ and ΔNπ vertices, respectively, and m_π is the pion rest-mass. $\vec{r}_{ki}$ is the relative separation betweeen nucleons 'i' and 'k' and is

given by the model as,

$$\vec{r}_{ki} = \vec{r}_k - \vec{r}_i = \vec{u}_k(\rho) - \vec{u}_i(\eta) + \Xi_{12}\vec{R} \qquad (2.4c)$$

where ρ and η are the internal coordinates of the two nuclei and $\vec{R}$ is the distance between the two ^{3}He's centers-of-mass. The Ξ_{12} factor for two colliding nuclei composed of A_1 and A_2 nucleons is,

$$\Xi_{12} = \sqrt{((A_1+A_2)/(A_1A_2))} \qquad (2.4d)$$

For the ^{3}He-^{3}He entrance channel,

$$\Xi_{12} = \sqrt{(2/3)}$$

Equation (2.4c) explicitly couples the center-of-mass motion of the two nuclei (via $\vec{R}$) to the elementary NN -> NΔ transition.

For clarity, the vertex functions are grouped within $\Gamma(\bar{q})$,

$$\Gamma(\vec{q}) = F_1(\vec{q})\cdot v(\vec{q})\cdot F_2(\vec{q}) \qquad (2.4e)$$

where $F_1(\vec{q})$ and $F_2(\vec{q})$ are the form-factors of the πNN and πNΔ vertices, respectively, and are measures of the finite size of the nucleon. $v(\vec{q})$ is the pion propagator and $\vec{q}$ is the pion's momentum. The spin-dependent and isospin-dependent terms are grouped within $\Sigma(\vec{q})$ for

conciseness,

$$\Sigma(\vec{q}) = (\vec{\sigma}_i \cdot \vec{q})(\vec{S}^{\uparrow}_k \cdot \vec{q})(\vec{\tau}_i \cdot \vec{T}^{\uparrow}_k) \tag{2.4f}$$

$\vec{\sigma}_i$ and $\vec{\tau}_i$ are the spin and isospin operators acting on nucleon 'i' emitting the virtual pion, and $\vec{S}^{\uparrow}_k$ and $\vec{T}^{\uparrow}_k$ are those for nucleon 'k' absorbing this pion and being elevated to a Δ_{33}.

The propagator, G, describing the Δ-nuclear intermediate system is,

$$G = (\omega - H)^{-1} \tag{2.5a}$$

where H is a general nuclear Hamiltonian that accounts for excited nucleons within the nucleus, and ω is the total energy in the center-of-mass system. The eigenmodes, $|\mu>$, of this Δ-nuclear intermediate system are,

$$H\,|\mu> = \epsilon_\mu\,|\mu> \tag{2.5b}$$

where ϵ_μ are the corresponding eigenenergies. A complete set of these eigenmodes can be inserted into equation (2.5a) to give,

$$G = \sum_{\mu} | \mu > (\omega - \epsilon_{\mu})^{-1} < \mu | \qquad (2.5c)$$

For calculation purposes, the model assumes that all of the values for ϵ_{μ} can be approximated by an average value ϵ_{C} (known as the 'closure energy'), as in the isobar-doorway model of Kisslinger and Wang [1976]. This 'closure approximation' yields,

$$G = (\omega - \epsilon_{C})^{-1} \qquad (2.5d)$$

The free π-N Δ_{33} excitation energy is about 315 MeV. Within the nuclear medium, this resonance is experimentally observed to be shifted down by about 50 MeV from that amount [Klingenbeck, 1981]. In the EB model, ϵ_{C} is chosen to account for this phenomenological energy shift. The eigenenergies and closure energy are all complex due to the Δ_{33}'s finite width.

The decay of the Δ_{33} and the creation of a real pion is described by the 'emission' operator, Λ_{r}, which is summed over all the $\Delta \rightarrow N\pi$ interactions in the final nucleus,

$$\Lambda_r = \sum_{j=1}^{6} \lambda_{\Delta N\pi}(j) \tag{2.6a}$$

where the $\Delta \rightarrow N\pi$ vertex for nucleon 'j' is described by,

$$\lambda_{\Delta N\pi}(j) = (2\pi)^{-3/2} (f^*/m_\pi) \int d^3k' \; F_3(\vec{k}') \exp(-i\vec{k}'\cdot\vec{r}_{j\pi}) \; \Sigma(\vec{k}') \tag{2.6b}$$

where f^* is the $\Delta N\pi$ coupling constant and m_π is the pion rest-mass and

$$\vec{r}_{j\pi} = \vec{r}_j - \vec{r}_\pi \tag{2.6c}$$

$F_3(\vec{k}')$ is the $\Delta N\pi$ vertex form-factor. The spin-dependent and isospin-dependent terms are again grouped together for clarity,

$$\Sigma(\vec{k}') = (\vec{S}_j^{\downarrow}\cdot\vec{k}')(\vec{T}_j^{\downarrow}\cdot\hat{\phi}_\pi) \tag{2.6d}$$

$\vec{S}_j^{\downarrow}$ and and $\vec{T}_j^{\downarrow}$ are the spin and isopsin operators, respectively, for the Δ_{33} going to nucleon 'j' and $\hat{\phi}_\pi$ is the pionic field operator.

For calculating the $^3He(^3He,\pi^+)^6Li$ reaction cross-sections, the Erlangen-Bonn model describes the ground and low-lying excited states of ^6Li in terms of a ^3He-^3H

clustering scheme. Harmonic-oscillator functions are used in the description of the ^{6}Li nuclear wavefunction. Using the closure approximation for G (equation (2.5d)) and omitting the reaction's non-resonant components given by T_{nr} introduces an estimated factor of 2 uncertainty into the final results. Another factor of 2 uncertainty is reported by the authors to be generated by off-shell effects and by neglecting interactions in the entrance channel. Effects due to pion distortion in the resonant channel are said to be approximately accounted for in the selection of the closure energy, ϵ_C.

In summary, then, because a microscopic description of the ^{3}He(^{3}He,π^+)^{6}Li reaction can become complicated, the Erlangen-Bonn model simplifies the calculation in three fundamental ways : neglecting those terms not involving a Δ_{33} resonance (i.e., s-wave and non-resonant p-wave scattering), invoking a closure approximation for the Δ-nuclear intermediate state propagator and neglecting entrance channel interactions.

The Erlangen-Bonn model has also been applied to the ^{4}He(^{3}He,π^+)^{7}Li and the ^{6}Li(d,π^-)^{8}B reactions. Predictions resulting from the EB model in its description of the ^{3}He(^{3}He,π^+)^{6}Li(g.s.) reaction are discussed in Section (2.3).

(2.2) A Phenomenological Calculation : the Germond-Wilkin Model

Because of the simplifications necessarily introduced into the EB Model as described above, another useful description of this reaction may perhaps be given by a phenomenological model which avoids those approximations. In such a model, the calculation's complexity is reduced by grouping those various factors which are not easily calculable within an experimentally measured quantity. This phenomenological quantity is then treated as an empirical input parameter. The caveat here is that the phenomenological approach simplifies the problem in order to allow insight into some particular aspects of that problem; it does not achieve the final goal of a detailed description of the reaction - which, of course, is obtainable only through a microscopic calculation. Such a phenomenological approach has been applied in calculations of the (p,π^+) reaction on light nuclei [Fearing, 1981; and references therein]. The cross-sections of these reactions may be related to the more 'fundamental' pp -> π^+d cross-section using a distorted wave impulse approximation (applied primarily to reactions such as $^2H(p,\pi^+)^3H$, $^3He(p,\pi^+)^4He$ and $^{12}C(p,\pi^+)^{13}C$, this model has been able to give a reasonable representation of the data at energies below 500 MeV).

Germond and Wilkin [1981,1982a,1982b,1984] have phenomenologically described exclusive $(^3He,\pi^+)$ reactions using two basic assumptions. It is assumed, firstly, that an

alpha cluster exists within the daughter nucleus and, secondly, that the 'fundamental' pion production mechanism is a $^3He(p,\pi^+)^4He$ subreaction. For example, in the $^3He(^3He,\pi^+)^6Li$ reaction, the ^6Li nucleus is described as being composed of a ^4He 'core' coupled to a valence deuteron. Therefore, by treating the $^3He(p,\pi^+)^4He$ reaction as the pion production mechanism, experimentally measured data for that reaction can be used as empirical input to the calculation.

Figure (2) summarizes the general features of the Germond-Wilkin (GW) model applied to the $^3He(^3He,\pi^+)^6Li$ reaction. In this model, the ^3He projectile interacts with a proton from the ^3He target, leaving behind a spectator deuteron. At the proton-^3He interaction vertex, the pion is produced via a $^3He(p,\pi^+)^4He$ reaction. The ^4He then undergoes a final-state interaction with the spectator deuteron to form a ^6Li nucleus.

The GW model assumes a linear relationship between the transition matrix elements of the measured $^3He(p,\pi^+)^4He$ reaction and that of the $^3He(^3He,\pi^+)^6Li$ process. With respect to Figure (2), the transition matrix element for $^3He(^3He,\pi^+)^6Li$ can be expressed as,

$$T_{fi} = X_{\alpha} X_{p} \int d\vec{K}\, d\vec{\eta}\, \Phi^{*}_{Li}(\vec{K}-\vec{Q},\vec{\eta}) T_{p-He}\, \Phi_{He}(\vec{K},\vec{\eta}) \qquad (2.7a)$$

X_{α} and X_{p} are spectroscopic factors related to the number of ^{4}He's and protons in the ^{3}He and ^{6}Li nuclei that contribute to the reaction. Φ_{Li} and Φ_{He} are the ^{6}Li and ^{3}He nuclear wavefunctions (note that the asterisk here refers to the complex conjugate), $\vec{\eta}$ are the internal variables of the spectator deuteron and $\vec{K}$ is the proton's momentum relative to the deuteron. $\vec{Q}$ is a momentum transfer variable defined by,

$$\vec{Q} = (1 - (m_{p}/m_{He}))\vec{p}_{He} - (1 - (m_{\alpha}/m_{Li}))\vec{p}_{Li} \qquad (2.7b)$$

where m_{p}, m_{He}, m_{α} and m_{Li} are the proton, ^{3}He, ^{4}He and ^{6}Li rest-masses, respectively, and where $\vec{p}_{He}$ and $\vec{p}_{Li}$ are the ^{3}He and ^{6}Li momenta, respectively.

T_{p-He} is the transition matrix element for the $^{3}He(p,\pi^{+})^{4}He$ subprocess,

$$T_{p-He} = \langle \vec{k}_{\pi}, \vec{K}+\vec{p}_{Li} - (1-m_{p}/m_{He})\vec{p}_{He} \,|\, T_{sub} \,|\, \vec{k}_{He}, \vec{K}+(m_{p}/m_{He})\vec{p}_{He} \rangle \qquad -(2.7c)$$

Figure (2)

The Germond-Wilkin Model of the $^3He(^3He,\pi^+)^6Li$ Reaction

(Terms in the figure are discussed in the text)

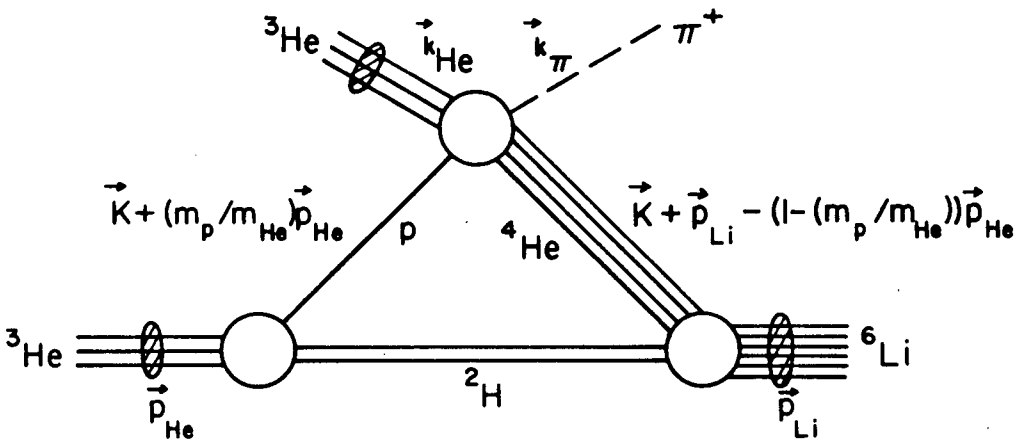

where T_{sub} is the transition matrix for the $^3He(p,\pi^+)^4He$ subprocess. This transition matrix element can be removed from the integral in equation (2.7a) using a factorization approximation. The product of the two nuclear wavefunctions,

$$\Phi^*_{Li}(\vec{K}-\vec{Q},\vec{\eta}) \cdot \Phi_{He}(\vec{K},\vec{\eta})$$

peaks at a value of the loop momentum, $\vec{K}_{PEAK}$. In this approximation, T_{p-He} is evaluated at $\vec{K}_{PEAK}$ and extracted from the integral.

From this basic representation, Germond and Wilkin derive a linear relationship between the $^3He(p,\pi^+)^4He$ and $^3He(^3He,\pi^+)^6Li$ cross-sections,

$$d\sigma/d\Omega^*\{^3He(^3He,\pi^+)^6Li\} = c \mid F(\vec{Q}) \mid^2 d\sigma/d\Omega^*\{^3He(p,\pi^+)^4He\} \quad -(2.8)$$

where c is a kinematic factor and $F(\vec{Q})$ is a complicated form factor that incorporates the ^3He and ^6Li nuclear wavefunctions and the ^4He and proton spectroscopic factors. A Gaussian form is assumed for the ^3He wavefunction; but it was reported that the model's results were relatively insensitive to the details of this wavefunction. The ^6Li nucleus in the 1^+ ground state is taken to be a ^4He nucleus coupled to a deuteron in an L = 0 relative angular momentum state. Two forms are used in this model for the ^6Li

wavefunction. The first type is calculated using a harmonic-oscillator potential. This result would be expected to be a poor representation of the real nuclear wavefunction due to the harmonic-oscillator potential's failure to reproduce the high-momentum components of the nuclear wavefunction that are probed in this reaction [Donnelly and Walker, 1969]. To improve their calculation, Germond and Wilkin have also evaluated the ^{6}Li wavefunction using a Woods-Saxon potential which gives a better reproduction of the high-momentum tail than does the harmonic-oscillator. Additionally, the Woods-Saxon potential is more realistic than the harmonic-oscillator in that it reproduces the saturation of the nuclear forces and decreases exponentially with increasing distance. The harmonic-oscillator potential, in contrast, increases with the square of the radius and, hence, requires a cut-off to be applied near the surface of the nucleus [Marmier and Sheldon, 1970]. These two wavefunction types yield widely varying results in the Germond-Wilkin model, as shown later.

For calculation purposes, the ^{3}He(p,π^+)^{4}He subreaction amplitude is parameterized. The differential cross-section for this subreaction is,

$$d\sigma/d\Omega^* = (2s_{^3He}+1)^{-1}(2s_p+1)^{-1}\cdot(k^*_\pi/k^*_{^3He})\ \Sigma\ |\ f\ |^2 \qquad -(2.9a)$$

where s_i is the spin of particle 'i' ($s_{^3He} = s_p = 1/2$), f is

the transition amplitude and the summation is over all the spin projections (f is the product of the transition matrix element of equation (2.7c) and a kinematic factor). From the conservation of angular momentum and parity, it can be shown that the proton and ^{3}He must be in a spin-triplet state. In the GW model, f is decomposed,

$$f = f_1(\vec{S}\cdot\vec{k}^*_{^3He}) + f_2(\vec{S}\cdot\vec{k}^*_{\pi}) \qquad (2.9b)$$

where the complex amplitudes f_1 and f_2 can be extracted from the measured $^3He(p,\pi^+)^4He$ data. For example, substituting equation (2.9b) into (2.9a) yields (for the S = 1 state),

$$d\sigma/d\Omega^* = (k^*_{\pi}/4k^*_{^3He})\cdot\,|\,f_1\vec{k}^*_{^3He} + f_2\vec{k}^*_{\pi}\,|^2 \qquad (2.9c)$$

Hence, a measurement of the differential cross-section does not allow f_1 or f_2 to be individually determined. Polarization observables (such as the analyzing power A_y and the spin-correlation parameter C_{xz}) yield other expressions in f_1 and f_2 [Ohlsen, 1972] which enable these amplitudes to be found. However, the polarization data for the $^3He(p,\pi^+)^4He$ reaction (and the related $^1H(^3He,\pi^+)^4He$, $^4He(\pi^+,p)^3He$, and $^4He(\pi^-,n)^3H$ reactions) are scant and simplifications of equation (2.9b) are consequently required. Because of the $\vec{k}_{\pi}$ factor in equation (2.9b), the f_1 term is expected to dominate at low energies and, hence,

the f_2 amplitude is neglected. The f_1 term is parameterized in terms of its zeros in the complex cos θ plane, where $\theta = \pi - \theta^*$ and θ^* is the center-of-mass angle for the (p,π^+) reaction. Two complex zeros are explicitly accounted for in this parameterization. The available experimental data do not fix the signs of these zeros' imaginary components, however, the model's authors report that the calculation is sensitive at most only to the relative signs of these two components.

The Germond-Wilkin model has also been applied to the $^4He(^3He,\pi^+)^7Li$ and $^6Li(^3He,\pi^+)^9Be$ reactions [Bimbot, et. al., 1982; Willis, et. al., 1984]. In the former case, the ^7Li nucleus is described in terms of an alpha core and a valence triton and in the latter, the ^9Be nucleus is assumed to be composed of two ^4He clusters and a neutron. The model's predictions for the $^3He(^3He,\pi^+)^6Li(g.s.)$ reaction are discussed in the next section.

(2.3) Comparison of the Erlangen-Bonn and Germond-Wilkin Calculations for $^3He(^3He,\pi^+)^6Li(g.s.)$

The two models just reviewed approach the $^3He(^3He,\pi^+)^6Li$ reaction with different philosophies. It is the purpose of this section to see how the models' predictions for this reaction compare by looking at the

energy and angular dependence of the calculated differential cross-section. Only the ground state of ^{6}Li will be considered here.

Figure (3) shows the energy dependence of these two calculations for ^{3}He(^{3}He,π^+)^{6}Li(g.s.) at $\theta^* = 30^\circ$. Several observations can be made from this plot. The $d\sigma/d\Omega^*$ predicted by the EB model peaks at about 380 MeV and then slowly decreases until about 425 MeV where it begins to drop off exponentially. This peaking is a manifestation of the Δ_{33} resonance within the nucleus. The GW predictions shown are for the harmonic-oscillator and Woods-Saxon wavefunction types used to describe the ^{6}Li nuclear wavefunction. Although the shapes of the Germond-Wilkin calculations are somewhat similar, the calculations vary considerably in magnitude. Each wavefunction type is further split up into two subsets (labelled + and -) corresponding to the relative signs of the imaginary parts of the complex zeros used in the ^{3}He(p,π^+)^{4}He input parameterization. The effect of these sign variations are small relative to that generated by the wavefunction realizations.

The Germond-Wilkin model calculations all peak at about 25 MeV above the physical threshold of 251 MeV and then sharply drop off. This peaking is about 100 MeV below that calculated by the Erlangen-Bonn model. Above 375 MeV, the GW Woods-Saxon and the Erlangen-Bonn calculations agree closely with each other, whereas the GW harmonic-oscillator calculation is about an order of magnitude less than the other two.

Figure (3)

Erlangen-Bonn and Germond-Wilkin Models' Predictions of the Energy Dependence of the $^3He(^3He,\pi^+)^6Li(g.s.)$ Reaction at $\theta^* = 30°$

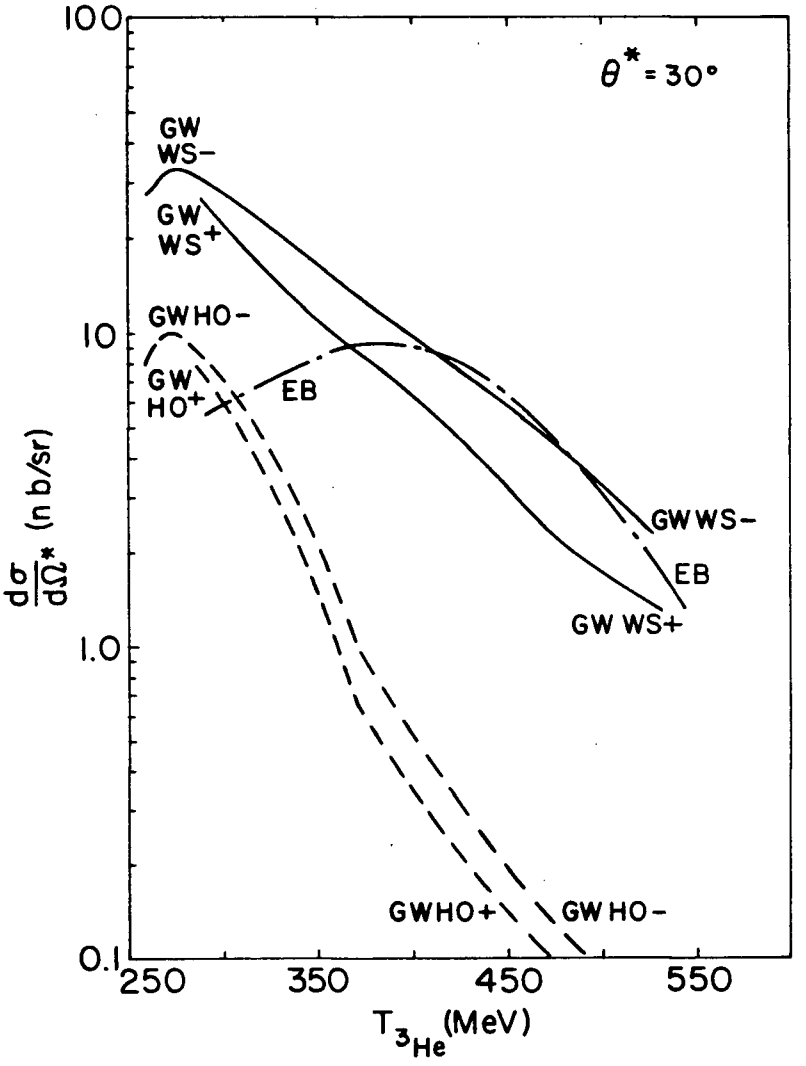

EB : Erlangen-Bonn model

GW HO : Germond-Wilkin model with harmonic-oscillator form

GW WS : Germond-Wilkin model with Woods-Saxon form

+/− : Relative signs of the imaginary parts of the complex zeros used in the $^3He(p,\pi^+)^4He$ parameterization for the Germond-Wilkin model.

Figure (4)

Erlangen-Bonn and Germond-Wilkin Models' Predictions of the Angular Dependence of the $^3He(^3He,\pi^+)^6Li(g.s.)$ Reaction at $T_{^3He} = 371$ MeV

(Same conventions used as in Figure (3))

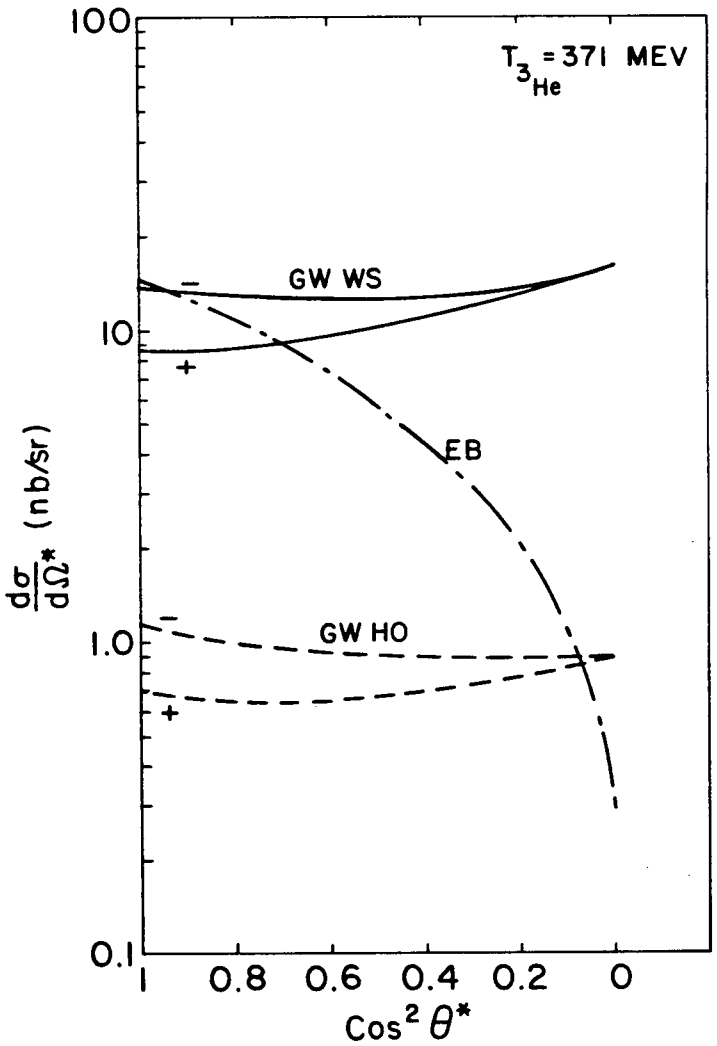

Angular distributions from both models for $^3He(^3He,\pi^+)^6Li(g.s.)$ at 371 MeV are shown in Figure (4). This energy corresponds to T_π = 60 MeV for the time-reversed fission $^6Li(\pi^+,^3He)^3He$. Because of the identical nature of the two ^3He's, the distributions are shown as functions of $\cos^2\theta^*$. The Erlangen-Bonn prediction decreases monotonically with $\cos^2\theta^*$ and, at about $\cos^2\theta^* = 0.4$, it begins to drop off sharply. In direct contrast, all of the Germond-Wilkin calculations show relatively little dependence upon $\cos^2\theta^*$. For both ^6Li wavefunction types, the $d\sigma/d\Omega^*$ decreases slightly with $\cos^2\theta^*$ and then starts to rise.

As discussed in Chapter 1, the bulk of the data (prior to that in this thesis) for $^3He(^3He,\pi^+)^6Li(g.s.)$ lay below 300 MeV. Beyond 300 MeV, or 24.5 MeV pion energy for the time-reversed $^6Li(\pi^+,^3He)^3He$ reaction, the data was scant. At these higher energies, the Erlangen-Bonn and Germond-Wilkin harmonic-oscillator calculations diverge, as shown in Figure (3). But, the EB excitation function agrees reasonably well with that for the GW Woods-Saxon result above 350 MeV (at least for $\theta^* = 30^0$). Figure (4) emphasizes the need for a measurement of angular distributions at these higher energies in order to differentiate between the models.

(2.4) Fusion vs Fission and Detailed-Balance

Theoretical and experimental studies of (^{3}He,π^+) reactions were triggered by interest in the pion production mechanism. But, as previously discussed, the time-reversed (π^+,^{3}He) reactions offer technical advantages over those in the (^{3}He,π^+) direction, in addition to providing data on pion absorption on more than two nucleons in a nucleus. The experiment described in this thesis is the pionic fission ^{6}Li(π^+,^{3}He)^{3}He and, hence, data from the corresponding pionic fusion, ^{3}He(^{3}He,π^+)^{6}Li(g.s.), must be transformed via detailed-balance in order to be compared with the results from this thesis.

From detailed balance, the center-of-mass differential cross-section for the reaction A(a,b)B is related to that of the time-reversed reaction B(b,a)A at the same total energy in the center-of-mass by [Segre, 1977],

$$d\sigma/d\Omega^*\{B(b,a)A\} = R\,(k_a^*/k_b^*)^2\, d\sigma/d\Omega^*\{A(a,b)B\} \qquad (2.10a)$$

where

$$R = \{(2s_a+1)(2J_A+1)\}/\{(2s_b+1)(2J_B+1)\} \qquad (2.10b)$$

and where s_i is the spin of particle 'i' and J_K is the nuclear spin of the nucleus 'K'. The spin of the ^{3}He nucleus

is 1/2, that of the pion is 0 and that of the ^{6}Li in the ground state is 1. Then, for the ^{3}He(^{3}He,π^+)^{6}Li(g.s.) and ^{6}Li(π^+,^{3}He)^{3}He reactions, equation (2.10a) reduces to,

$$d\sigma/d\Omega^*\{^6\mathrm{Li}(\pi^+,{}^3\mathrm{He})^3\mathrm{He}\} = (4/3)(k_{^3\mathrm{He}}{}^*/k_{\pi}{}^*)^2 \cdot d\sigma/d\Omega^*\{^3\mathrm{He}(^3\mathrm{He},\pi^+)^6\mathrm{Li}(\mathrm{g.s.})\} \qquad -(2.11)$$

Equation (2.11) will be used in this thesis to transform the ^{3}He(^{3}He,π^+)^{6}Li(g.s.) differential cross-sections to those for ^{6}Li(π^+,^{3}He)^{3}He.

3 EXPERIMENTAL APPARATUS AND PROCEDURES

(3.1) TRIUMF and the M11 Secondary Beamline

TRIUMF (Tri-University Meson Facility) (Figure (5)) is a sector-focussing cyclotron providing two simultaneous beams of protons with energies of up to 520 MeV and (unpolarized) currents approaching 130 μA in 43 nanosecond period bursts [Craddock, et. al., 1977]. The M11 secondary beamline, on which the experiment described in this thesis was performed, transports medium-energy pions produced at the target location T1 on the 1A primary beamline in the Meson Hall.

In detail, the M11 channel (Figure (6)) was designed to produce a π^+ or π^- beam with energies between 50 and 350 MeV at rates of 10^6 to 4×10^8 pions/second [Stinson, 1980]. During this experiment, 500 MeV unpolarized protons, at currents between 100 and 130 μA, bombarded the pion production target. For the 60 and 80 MeV pion energy data, this was a 10 mm thick water target; for the 100 MeV pion energy data, the target was 10 mm thick pyrolytic graphite.

There are fifteen magnetic elements in the M11 channel between the production target and the final focus. The primary proton beam is refocussed after passing through the production target by the 1AQ9 quadrupole magnet. Because of the pions' lower momenta, the quadrupole bends them into a septum magnet (11S1) away from the proton beam.

Figure (5)

TRIUMF

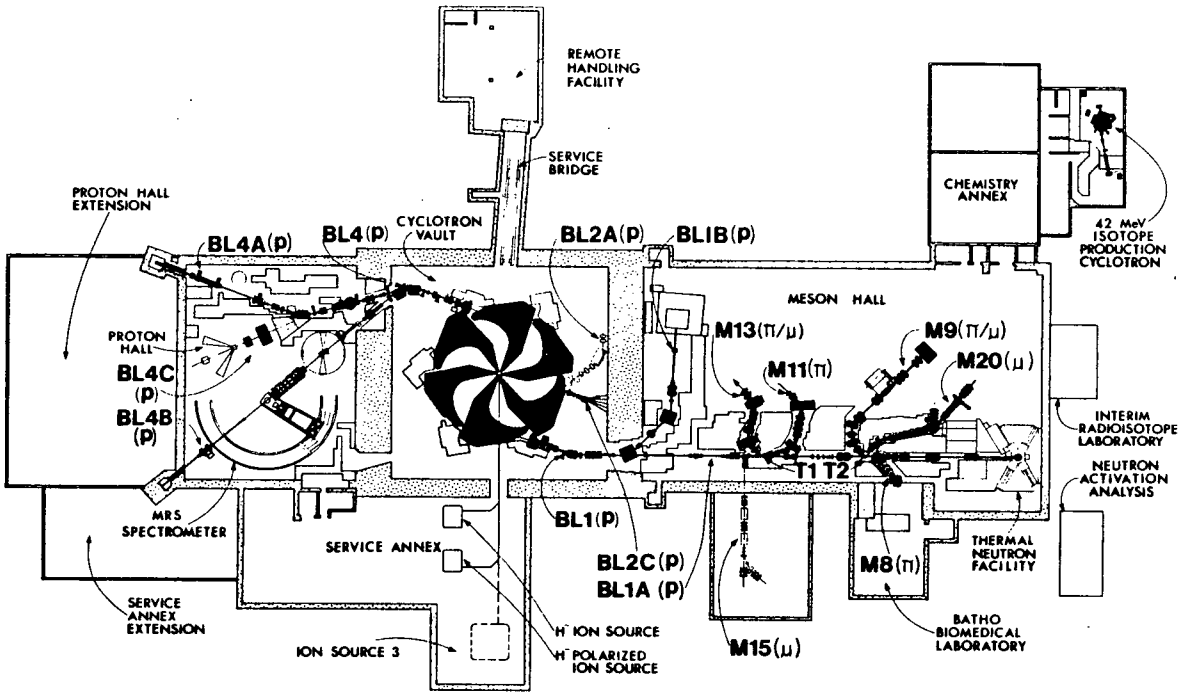

The experiment described in this thesis was performed on the M11 secondary beamline in the Meson Hall.

Figure (6)

The M11 Secondary Beamline

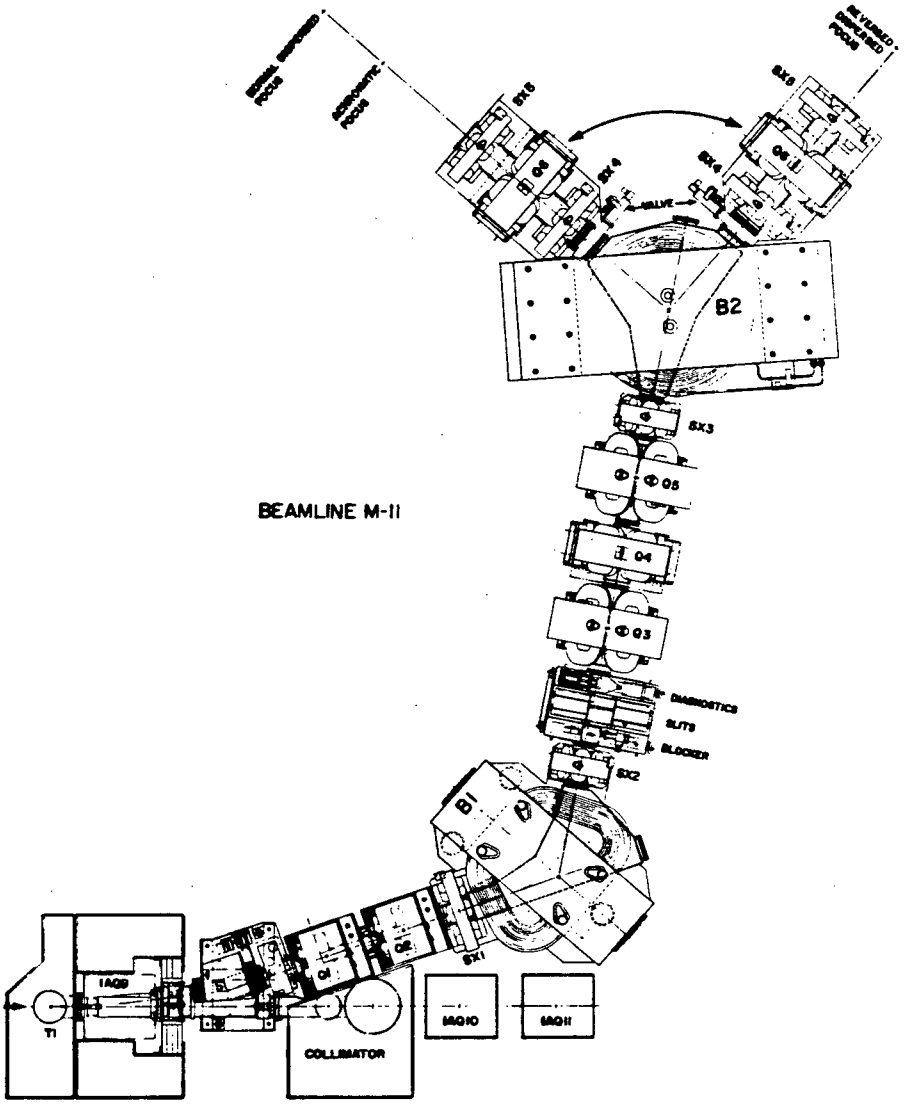

Elements in this beamline are discussed in the text.

After the septum is a set of jaws for varying the pion flux acceptance of the channel. Once through these jaws, the pions are focussed by a quadrupole doublet (11Q1 and 11Q2) and bent through a dipole magnet (11B1). This dipole produces a dispersed focus at a set of slits positioned at the exit of the dipole. These slits can be set to choose the momentum 'bite' ($\Delta p/p$) of the pion beam, which was typically about 5% during the course of the experiment. Also at this point, known as the mid-plane focus, a degrader may be introduced in order to reduce the number of protons contaminating the beam. The protons suffer a greater energy loss passing through this degrader than do the pions and, due to the larger reduction of their momentum upon exiting the degrader, the second dipole magnet (11B2) sweeps them away from the pion beam. For this experiment, the degrader was a 0.020" thick slice of polyethylene. Between the mid-plane focus and the second dipole is a quadrupole triplet (11Q3, 11Q4 and 11Q5) providing horizontal and vertical focussing. The second dipole bends the beam through a final quadrupole (11Q6) to the target position. Interspersed throughout the channel are five sextupoles (11SX1 through 11SX5) providing second-order corrections to the beam optics.

An achromatic focus was attained at the ^{6}Li target position producing a beam spot with a 3.5 cm full width horizontally and 3 cm full width vertically. This spot size was measured by placing a multiple-wire proportional chamber at the focus whilst tuning the beam. The only observed beam

contaminants were muons (from $\pi \rightarrow \mu\nu$ decay) and electrons generated via pair production by the γ-rays from π^0 decay at the production target. How the relative populations of these contaminants were determined is described in Section (3.3).

(3.2) Apparatus

(3.2.1) Detectors

Detecting and differentiating between charged particles with a counter system is possible with a detector thin enough for the incident particles to pass through followed by one sufficiently thick to stop them [Goulding and Harvey, 1975]. The energy deposited in the passing counter by a heavy charged particle, ΔE, is related to the total incident energy, E, by an approximation to the Bethe-Bloch equation,

$$\Delta E = kZ^2 \cdot \sqrt{(M/E)} \qquad (3.1)$$

where k is a constant of proportionality and where M and Z are the particle's mass and charge, respectively. For a sufficiently thin transmission counter, ΔE is small and E can then be closely approximated by the energy deposited in the stopping counter. Determining ΔE and E will thus yield a measure of $Z^2 \cdot \sqrt{M}$.

A variant of this ΔE-E telescope that was designed for this experiment included a second passing counter for redundancy. All of these counters were made from plastic NE-102 scintillator. Over the kinematic region explored, the stopping counter was thick enough to stop the pionic fission ^{3}He nuclei (which had a maximum range of 1.4 cm), but also thin enough to allow more penetrating background particles (predominantly pions and protons) to pass through. A veto counter (V), placed behind the E scintillator, was used in anticoincidence so as to reject these particles.

The two ΔE counters, denoted by ΔE_1 and ΔE_2, were both (0.1 x 9 x 30) cm^3, whereas the E counter was (2.54 x 8 x 30) cm^3 and the veto counter was (0.8 x 9 x 30) cm^3. These dimensions were selected as a large detection solid angle was required for the low cross-section ^{6}Li(π^+,^{3}He)^{3}He reaction. Being narrower and further away from the ^{6}Li target than either ΔE scintillator, the E counter defined the telescope's solid angle.

The first three scintillators of each telescope were sheathed in only 22 μm aluminum sheet so as to minimize the dead space between counters. All of the scintillators were coupled to Philips XP2230H photomultiplier tubes (PMT). The ΔE_1, E and V scintillators were connected to their PMTs via Lucite light-guides. Because of space restrictions within the telescope stand, the ΔE_2 scintillator was coupled to its photomultiplier tube by a set of three flexible fiber-optic cables [Yang, et. al., 1981; Huber, et. al., 1984].

Figure (7)

Experimental Arrangement

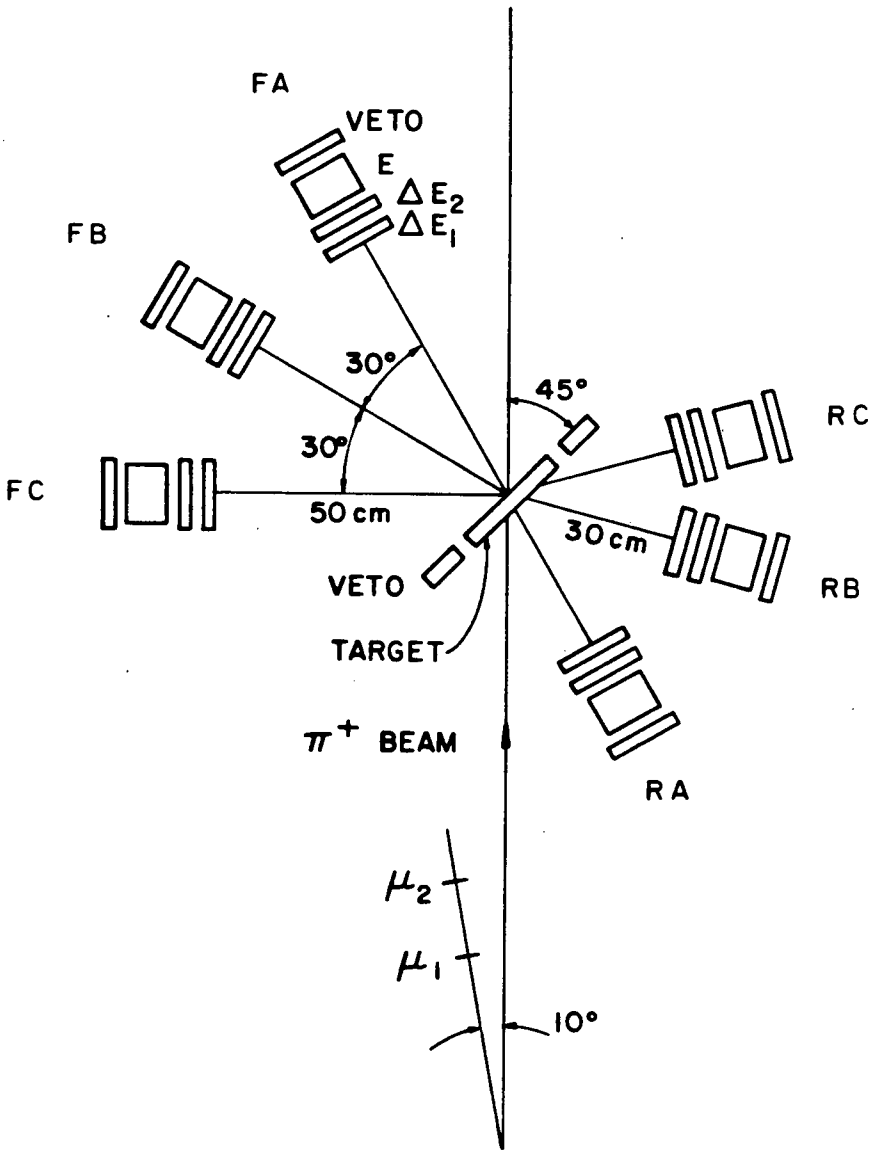

The $(\mu_1 \cdot \mu_2)$ counters are mounted at a 90° azimuthal angle; 'A', 'B' and 'C' refer to the conjugate arms and 'F' and 'R' refer to 'Front' and 'Rear'.

Figure (7) shows the overall arrangement of the experimental apparatus. Due to the expected low reaction rate of the pionic fission, beam time was optimized by simultaneously counting at three angles (arms A, B and C) with three pairs of coincident telescopes. The forward telescopes (F) were set at 30° intervals in the lab frame and at a distance of 50 cm from the target while the rear telescopes (R) were placed at the kinematic conjugate angles and 30 cm from the target. For the one case of the forward telescope set at a lab angle of 15°, its conjugate (at about -165°) was placed 35 cm away from the ^{6}Li target so as to avoid intercepting any incident beam halo. This arrangement assured that the forward telescope defined the conjugate pair's total solid angle. The angular width and height of the front telescope, defined by the face of the E counter closest to the ^{6}Li target, were 9.2° and 33.4°, respectively.

An effective solid angle, $\Delta\Omega_{eff}$, for a telescope pair was estimated using a Monte Carlo code (described in Appendix B) which incorporated the apparatus geometry, the finite size beam spot, the reaction kinematics and the mean energy losses of the ^{3}He nuclei in the target, air and detectors. A mean value of about 75 msr was obtained for $\Delta\Omega_{eff}$ in the lab. $\Delta\Omega_{eff}$ varied as a function of pion energy and detector angle, as shown in Figure (8). These variations were due to the ^{3}He nuclei stopping prior to reaching the

Figure (8)

Effective Lab Solid Angle vs Front Telescope Lab Angle

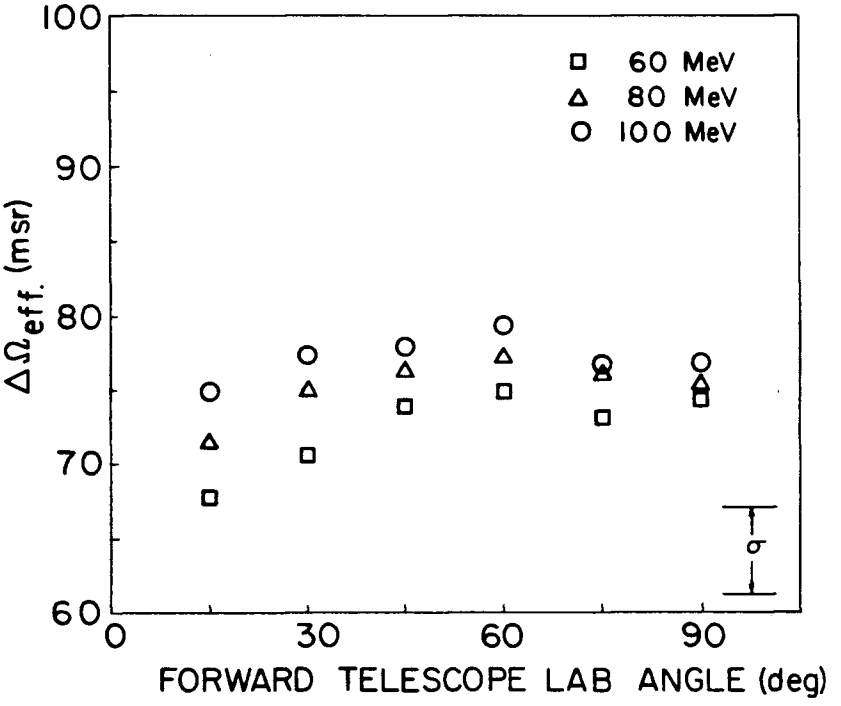

$\Delta\Omega_{eff}$ is estimated by the Monte Carlo code. Variations of $\Delta\Omega_{eff}$ with pion energy and telescope angle are due to the ^{3}He nuclei stopping prior to reaching the E counters. σ represents the relative uncertainty in $\Delta\Omega_{eff}$ due to the simulation statistics (see Subsection (4.1.2) and Appendix B).

E counters and were dependent upon the ^{3}He energies and the amount of material along the ^{3}He trajectory from within the ^{6}Li target to the telescope.

(3.2.2) Targets and Target Holder

Three targets were used in this experiment : a liquid D_2O target (within a steel container with stainless-steel foil windows) for calibrating the pulse heights from the photomultiplier tubes and the detectors' efficiencies using the $\pi^+d \rightarrow 2p$ reaction, a 95% enriched ^{6}Li target with an areal density of 112 mg/cm^2, and a background target. The areal density of the lithium target (which was sheathed in a polyethylene bag containing mineral oil in order to prevent oxidation) was measured directly and the isotopic content was provided by the manufacturer, Oak Ridge Laboratories. The background target was simply an identical plastic bag with the same amount of mineral oil.

To aid in reducing the number of background events, the target was mounted over a 7x7 cm^2 window cut in a thin vertical sheet of plastic scintillator. This 'beam-veto' counter had one photomultiplier tube observing it from each end (BV_1 and BV_2). Any event originating from within this scintillator would be outside the area covered by the target and would generate a hard-wired veto, from the 'ORed' BV_1 and BV_2 logic signals (equation (3.2d)), in the event logic.

The target was set at a 45^0 angle to the beam.

(3.2.3) Event Logic Definition

A valid event for recording was defined as,

$$EV = ((FA \cdot RA) + (FB \cdot RB) + (FC \cdot RC)) \cdot \overline{BV} \qquad (3.2a)$$

with the individual telescopes' logic defined as,

$$Fi = Fi\Delta E_1 \cdot Fi\Delta E_2 \cdot FiE \cdot \overline{FiV} \; ; \quad i = A, B, C \qquad (3.2b)$$

and,

$$Ri = Ri\Delta E_1 \cdot Ri\Delta E_2 \cdot RiE \cdot \overline{RiV} \; ; \quad i = A, B, C \qquad (3.2c)$$

The beam-veto logic definition was,

$$BV = BV_1 + BV_2 \qquad (3.2d)$$

Combining all these, an event trigger required a six-fold hardware coincidence of all six ΔE and E elements in any conjugate pair together with no signals from that pair's veto counters nor from the target holder.

Simplified NIM electronics diagrams for a single conjugate telescope pair's logic and for the control logic are shown in Figures (9) and (10). A DEC PDP-11/34

Figure (9)

Electronic Logic For a Conjugate Telescope Pair

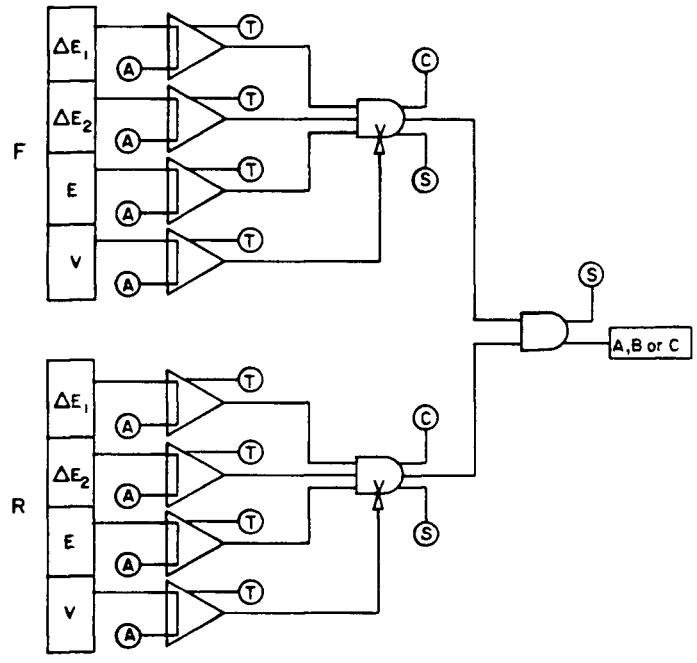

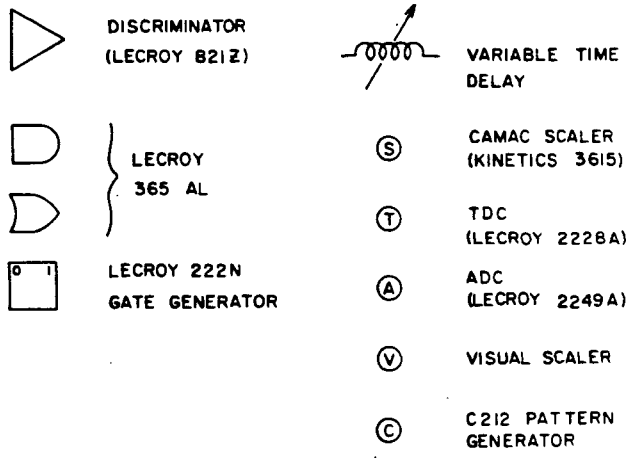

Figure (10)

Electronic Control Logic

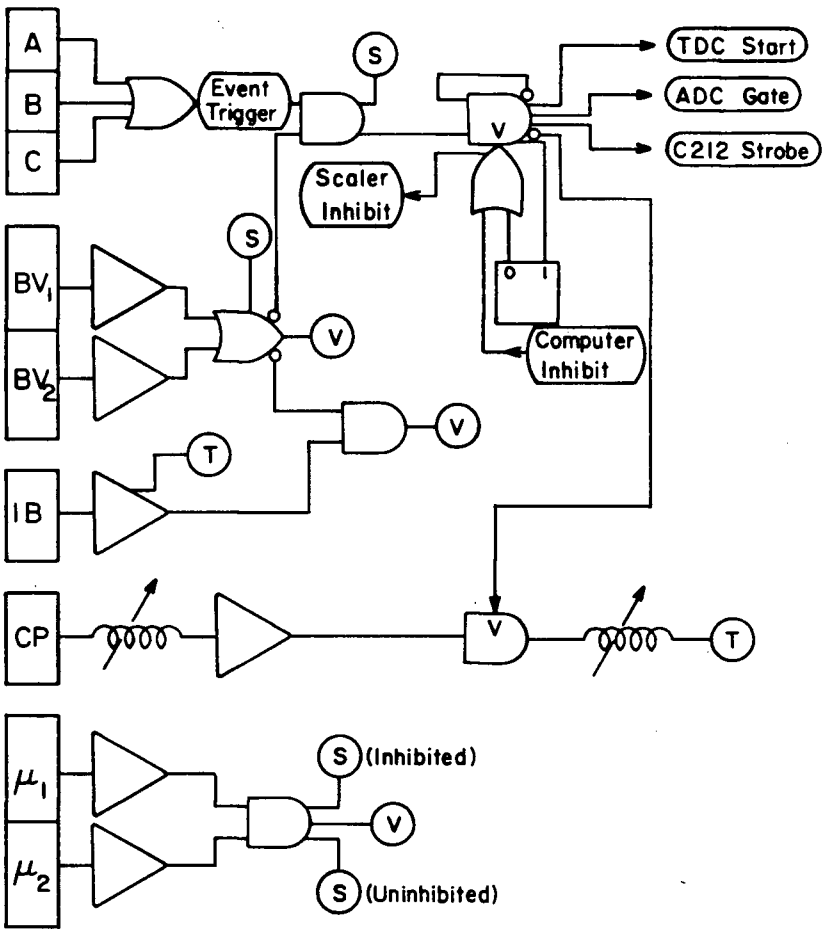

An event from any conjugate pair, in anticoincidence with (BV_1 + BV_2), generates a LAM to the computer through the C212 pattern generator strobe. IB refers to an in-beam scintillator placed downstream of the ^{6}Li target; CP refers to a capacitor probe adjacent to the 1AT1 pion production target.

minicomputer, used for data acquisition and on-line analysis, was interfaced to the CAMAC through a Kinetic Systems 3912 crate controller. The data satisfying the logic definition were written event-by-event onto magnetic tape and on-line event diagnostic analysis was performed using the TRIUMF standard MULTI software system [Miles and Satanove, 1983].

For a valid event, a 'look-at-me' (LAM) interrupt request to the computer was supplied via a strobe signal from an Ortec C212 coincidence buffer. Bits in the C212 pattern, corresponding to which telescopes had fired, were set by a valid event for later use in the off-line analysis. While the LAM was being serviced, an 'inhibit' signal generated by the computer was fed to the logic via a NIM output register in order to suppress any further events from being counted and signalling another interrupt.

Upon servicing the LAM, all ADC (LeCroy 2249A) and TDC (LeCroy 2228A) inputs were written into a buffer, as was the C212 bit pattern. Once this buffer was filled, it was then written onto magnetic tape and processed by MULTI.

Several rates were monitored with Kinetics 3615 hex CAMAC scalers : including those from the decay muon counters (for beam normalization), singles rates for each telescope and the beam-veto counts. A measure of the computer dead-time was obtained by comparing the decay muon counts read through a CAMAC scaler that was inhibited during the LAM servicing to those read through an uninhibited scaler. This dead time was usually of the order of about 7% or less.

It was not necessary to correct for this computer dead-time as the inhibited decay muon scaler was used for beam normalization. Dead-times introduced by the telescope veto and the beam-veto counters, though, did not inhibit this decay muon scaler and had to be explicitly accounted for as described in the next chapter.

All of the analog signals from the photomultiplier tubes were passed through variable attenuators so that the ^{3}He signals could be placed in a linear region of the ADC response. The discriminator threshold levels were set to exclude the low pulse height signals from the predominant background components, pions and protons. The relative timing of the counter signals in a telescope and its conjugate was set such that the event 'start' timing pulse was defined by the forward E counter. The choice of the TDC signal from the front E counter as the conjugate pair's timing reference was based on the assumption that that counter would generate the largest signal amplitude of the six counters in the telescope pair. Figure (11) shows the relative timing of the logic signals for the four counters in one telescope, for the front and rear telescopes in a conjugate pair, and for an event in a conjugate pair plus the beam-veto signal.

Figure (11)

Logic Relative Timing Signals

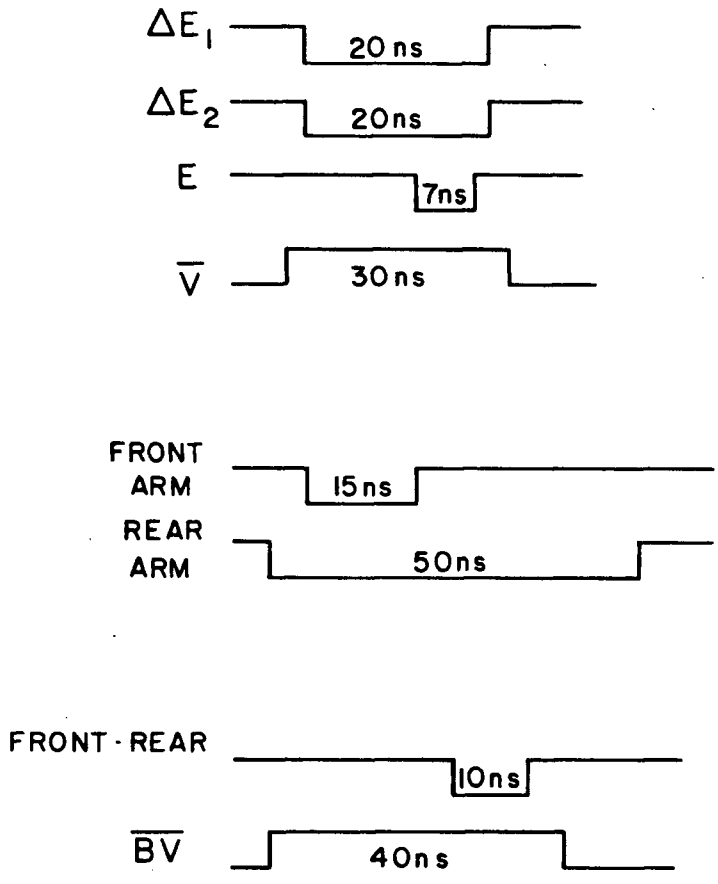

The Front E TDC pulse, being narrower than the Front ΔE_1 and ΔE_2 TDC pulses, ensures that it defines the start timing pulse for the Front telescope. As the Front arm event TDC pulse is narrower than the Rear arm event TDC pulse, the conjugate event start timing pulse is defined by the Front E counter.

(3.3) Pion Beam Normalization

The simplest method of measuring the number of pions incident on the ^{6}Li target would have been to place a thin transmission scintillator in front of the target and to directly count the pions, while also correcting for the muon and electron contamination. Because the photomultiplier tubes operated inefficiently at the beam rates demanded by this experiment (typically several MHz), this technique was obviously not viable. As a result, the beam halo, which consisted primarily of muons from $\pi \rightarrow \mu\nu$ decay and was proportional to the pion flux, was monitored by a telescope $((\mu_1 \cdot \mu_2))$ composed of two scintillation counters in coincidence [Coulson, et. al., 1972].

The count rate from this telescope was only some tens of kHz and could be easily handled by photomultiplier tubes. Although muons from π decay are produced isotropically in the center-of-mass system, those resulting from π decay in flight are pushed into a forward angular cone of about $\pm 15^0$ at the pion energies studied. Thus the $(\mu_1 \cdot \mu_2)$ telescope was placed at a 10^0 angle from the beam axis such that it was always within the maximum opening angle of the decay.

The calibration of the muon telescope against the pion flux was performed using two independent techniques : one with an in-beam counter and the other using a ^{11}C activation method. The former required a scintillator larger than the 7x7 cm^2 target hole to cover that empty window. Counts from the muon telescope $(\mu_1 \cdot \mu_2)$ and those from the in-beam

counter, in anticoincidence with the beam-veto counter ($IB \cdot \overline{BV}$), were monitored on NIM visual scalers and recorded. The ($IB \cdot \overline{BV}$) scaler was a direct count of those particles passing through the window and, effectively, those that would be incident on the ^6Li target were it in place.

The calibration ratio is defined as the pion flux normalized to the ($\mu_1 \cdot \mu_2$) count rate. For the in-beam counter technique, this ratio was,

$$R_{IB} = f_{\pi} \; P \; (IB \cdot \overline{BV}) \; / \; (\mu_1 \cdot \mu_2) \qquad (3.3)$$

where ($IB \cdot \overline{BV}$) and ($\mu_1 \cdot \mu_2$) are the scaler counts obtained over a set period of time. f_{π} is the fraction of the beam composed of pions and P is a pile-up correction factor for ($IB \cdot \overline{BV}$).

The logic pulse from the in-beam scintillator discriminator was 20 ns long. Since the time width of the beam bucket was about 5 ns, at most only one particle could be resolved per bucket by the ($IB \cdot \overline{BV}$) scaler. Consequently, a pile-up correction was necessary in order to account for the missed beam particles.

The measured average number of counts per beam burst, S, is equal to the probability of one or more counts occuring during that burst and can be calculated assuming Poisson statistics,

$$S = 1 - \exp(-\zeta) \tag{3.4a}$$

where ζ is the actual mean number of particles per beam bucket. Inverting equation (3.4a) solves for ζ,

$$\zeta = -\ln(1 - S) \tag{3.4b}$$

The pile-up correction factor, P, is the ratio of the actual rate to the measured rate,

$$P = \zeta / S \tag{3.4c}$$

This pile-up correction factor was of the order of 15% for a beam rate of about 6 MHz.

Because the $(IB \cdot \overline{BV})$ scaler was counting all of the beam particles, not just the pions, a correction for the fraction of the beam consisting of muons and electrons had to be made. The relative fractions of the beam due to π's, μ's and e's were determined by measuring the time-of-flight (TOF) between a point immediately before the pion production target and an in-beam scintillator that was situated downstream of the ^{6}Li target during all of the runs. Despite having equal momenta and almost equal trajectory lengths, the particles exiting the beam pipe had different TOF's due to their differing masses. The start of the measured TOF was defined by the arrival of a timing pulse from a capacitor probe on the primary proton beamline just adjacent to the production target. A typical beam TOF spectrum, for a

channel momentum of 169.5 MeV/c (or a pion energy of 80 MeV) is shown in Figure (12).

At T_π = 100 MeV with the pyrolytic graphite production target the beam rate was about 18 MHz, which would have resulted in pile-up corrections in excess of 50%. For the in-beam calibration at this energy only, the proton beam current was reduced to about 15 μA so as to lower the M11 beam rate. For the ^{11}C activation technique, which is not rate-dependent, the current was returned to its nominal value of about 130 μA.

The second, and independent, calibration method compared the $(\mu_1 \cdot \mu_2)$ scaler count against the pion beam rate determined from ^{11}C activation [Dropesky, et. al., 1979; Butler, et. al., 1982]. In this technique (which is briefly outlined in Appendix C), the number of ^{11}C nuclei produced after the pion irradiation of a ^{12}C target is determined. From this amount of ^{11}C, the number of pions incident during the irradiation time is then calculated. For this experiment the ^{12}C target was a plastic scintillator disk, larger than the beam spot, mounted at the ^{6}Li target position. The calibration ratio for the ^{11}C activation normalization method is,

$$R_{^{11}C} = N_\pi / (\mu_1 \cdot \mu_2) \qquad (3.5)$$

where N_π is the calculated number of pions bombarding the target during the irradiation time and where $(\mu_1 \cdot \mu_2)$ is the muon telescope scaler count during that time.

Figure (12)

TOF Spectrum for Beam Particles
At a Channel Momentum of 169.5 MeV/c

$(\beta_\pi = 0.772,\ \beta_\mu = 0.849,\ \beta_e \sim 1)$

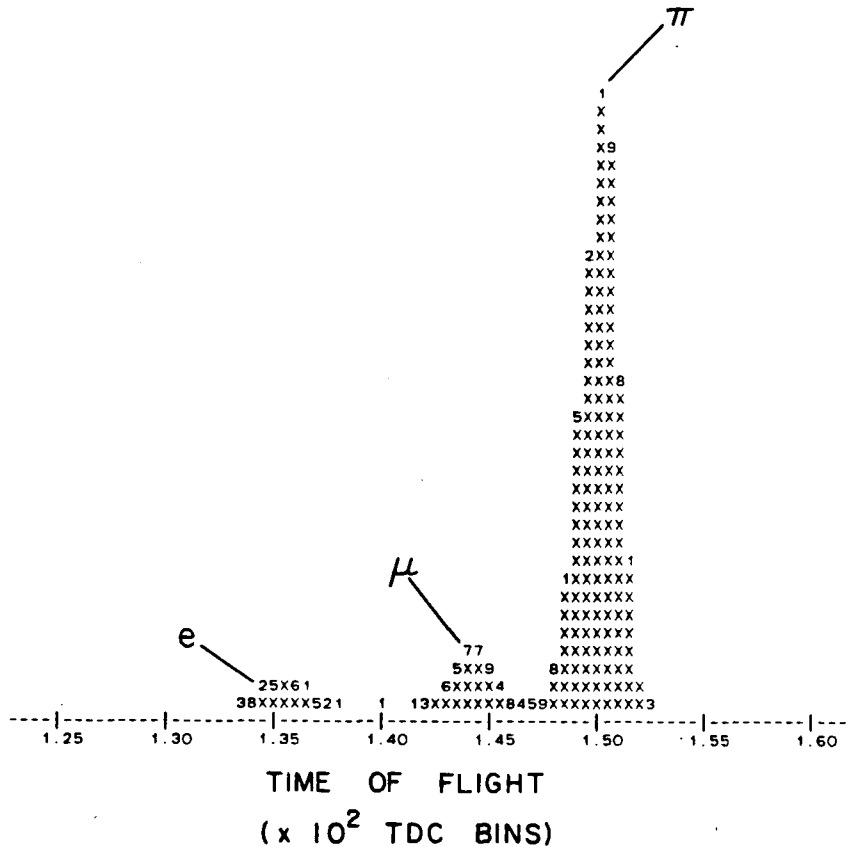

Mean values and errors for both calibration ratios, typical pion fluxes and the relative μ-e contamination for all pion energies and production targets used in this experiment are given in Table (I). It should be noted that the calibration ratios obtained from these two independent techniques agree with each other to within about 10%.

TABLE (I) M11 π^+ Beam Normalization Summary

Pion Energy (MeV)	Pion Production Target Type (1AT1)	Pion Rate ($\times 10^6$ sec^{-1})	μ-e Beam Fraction (%)	{Pion / Decay Muon} Counts	
				In-Beam Counter Calibration	^{11}C Activation Calibration
60	10mm H_2O	2.3	27	9596 ± 140	10249 ± 384
80	10mm H_2O	5.9	17	7617 ± 70	8400 ± 372
100	10mm Py.Gr.	18.2	8	6807 ± 111	6731 ± 242

(3.4) Measurement Protocol

Prior to any data taking with the ^6Li target, the D_2O target was mounted on the target holder and the $\pi^+d \rightarrow 2p$ reaction at 80 MeV was used to calibrate the photomultiplier tubes' pulse heights and the telescopes' efficiencies. These calibrations are detailed in the next section.

At each pion energy, measurements were taken at six

angles (forward telescopes at lab angles of 15°, 30°, 45°, 60°, 75° and 90°) for the ^{6}Li target and the background target. Since the six angles were measured in two groups (15°-45°-75° and 30°-60°-90°) the normal procedure was to detect events from the ^{6}Li target (at 15°-45°-75°) and then replace the ^{6}Li with the background target for about 15% to 20% of the $(\mu_1 \cdot \mu_2)$ counts accumulated during the ^{6}Li measurement. Then the telescopes were set to 30°-60°-90° (and their conjugate angles) and the entire procedure repeated. After this 'core' set of measurements was completed, they were repeated in reverse : 30°-60°-90° followed by 15°-45°-75° for both targets. Including the inevitable machine stoppages, beam calibrations, etc., the angular distribution for the ^{6}Li(π^+,^{3}He)^{3}He reaction at a single pion energy was usually measured in a period of about one hundred hours.

(3.5) Detector Calibration

(3.5.1) Response Calibration

It was originally feared that the non-linear response of the plastic scintillator to the densely ionizing ^{3}He nuclei would introduce difficulties in their identification and separation from the background. A quantitative representation of this non-linear scintillator response is given in Appendix A. In that Appendix, the scintillation

output of NE-102 is calculated as a function of particle type and energy.

The calibration procedure used was to measure the light response (i.e., the ADC value) of all of the counters to the proton signal from the $\pi^+ d \rightarrow 2p$ reaction at $T_\pi = 80$ MeV. The ADC channel value for a ^3He event from the $^6Li(\pi^+, {}^3He)^3He$ reaction could then be estimated with,

$$ADC_{^3He} = ADC_P \cdot (L_{^3He} / L_P) \qquad (3.6)$$

where ADC_P is the measured ADC response for the $\pi^+ d \rightarrow 2p$ calibration proton and $L_{^3He}$ and L_P are the calculated scintillator light outputs for ^3He and protons, respectively, and are both determined using the calculated energy losses (see, for example, Gooding and Pugh, [1960]). As equation (3.6) was only required to estimate the approximate region of the ADC response in which to search for the ^3He events, the non-linearities and offsets in the ADC response could be neglected. For the $\pi^+ d \rightarrow 2p$ calibration, each arm of a conjugate pair was sequentially placed at 50 cm from the target at $\theta^* = \pm 90^\circ$ which, for the 80 MeV pion energy used, corresponded to $\pm 80^\circ$ in the lab. As both protons from the $\pi^+ d \rightarrow 2p$ reaction at this angle had 110 MeV kinetic energy in the lab, they were energetic enough to pass through even the 2.54 cm thick E counter. So as to have these protons stop in the E counter and generate

a scintillator light response comparable to that calculated for the ^{3}He nuclei, a 1.375" thick aluminum degrader was placed between each telescope and the heavy-water target during the calibrations. This degrader reduced the mean proton energy incident on the telescope to about 30 MeV. At this energy, the proton mean range in scintillator is less than a centimeter and so, even allowing for range straggling, the protons would stop within the E counter. Including the telescopes' veto counters in anticoincidence provided further insurance that only those protons stopping in the E counters were recorded on tape for analysis. As described in Appendix A, the scintillator light output generated by stopped protons of this energy is comparable to that from the ^{3}He nuclei in the kinematic region explored.

(3.5.2) Efficiency Calibration

Because the counters in a conjugate pair were used in a six-fold coincidence (with their vetoes and beam-veto in anticoincidence) during the ^{6}Li(π^+,^{3}He)^{3}He runs, an estimate of their intrinsic efficiencies had to be made prior to data-taking. This was done during the π^+d -> 2p calibration for which a hardware-defined event in a conjugate telescope pair consisted of (any) two-fold coincidences between pairs of ΔE or E counters (during these calibration runs, the discriminator thresholds for all the counters were set as low as possible; for the ^{6}Li(π^+,^{3}He)^{3}He data-taking runs,

the threshold levels of the ΔE_1 and ΔE_2 counters were raised so as to exclude pions and most of the protons, whereas the E and telescope veto counters' thresholds were left untouched). For a single telescope composed of three counters 'i', 'j' and 'k', the efficiency of counter 'i' is given by the ratio of counts,

$$\epsilon_i = N_{ijk} / N_{jk} \tag{3.7}$$

where N_{ijk} is the number of valid $\pi^+d \rightarrow 2p$ events occurring with a three-fold coincidence between counters 'i', 'j' and 'k' in the telescope, and N_{jk} are those with a two-fold coincidence between counters 'j' and 'k'. Implicit in both of these coincidence requirements is that for each event in a single counter there be a valid three-fold coincident $\pi^+d \rightarrow 2p$ event in the conjugate telescope. During the off-line analysis, a valid $\pi^+d \rightarrow 2p$ event was defined by software cuts set on the proton ADC peak. The efficiencies of all the counters are given in Table (II); the errors shown in that Table are due to the $\pi^+d \rightarrow 2p$ reaction counting statistics. Of interest is the observation that all of the E counters had efficiencies within the range of 94% to 99%. This is believed to be partly due to the geometry of the counters within the telescope. As the E counter (8×30 cm^2) is narrower than the ΔE counters (9×30 cm^2),

TABLE (II) - Counter Efficiencies (%)

Telescope	Counter		
	ΔE_1	ΔE_2	E
FA	92.4(1.3)	100.0(0.0)	98.8(0.6)
RA	97.1(0.4)	99.9(0.1)	94.0(0.6)
FB	96.4(1.4)	100.0(0.0)	97.6(1.2)
RB	99.4(0.6)	98.7(0.9)	96.3(1.5)
FC	100.0(0.0)	100.0(0.0)	95.6(1.2)
RC	100.0(0.0)	99.9(0.1)	95.9(0.5)

- Quantities in brackets are errors from the $\pi^+ d \rightarrow 2p$ counting statistics

then the efficiency of the E counter calculated with equation (3.7) would be equal to the overlap of the areas of the ΔE and E counters, or 8/9 = 89% (neglecting other sources of inefficiencies). The fact that the E counter efficiencies are slightly larger can be attributed to the lack of perfect alignment of the counters.

In principle, the $^6Li(\pi^+,{}^3He)^3He$ runs could have been performed with such an event definition which would have

permitted the $^6Li(\pi^+,{}^3He)^3He$ detection efficiencies to be measured directly. This procedure was rejected on the basis that, firstly, the number of accumulated $^6Li(\pi^+,{}^3He)^3He$ events would be so small that determining a statistically meaningful efficiency would be unlikely. Secondly, operating in this manner would have resulted in the wasteful recording of a large number of background events on tape during the course of the long data-taking runs.

As all of the measured counter efficiencies were greater than 92%, the ^3He detection efficiency was taken to be 100%. The estimated uncertainty associated with this assumption is discussed in Subsection (4.1.3).

The inefficiencies due to nuclear reactions between the ^3He nuclei and the carbon and hydrogen in the scintillator were also estimated. A review of the literature revealed a very small amount of useful data of such inelastic interactions. An estimate of less than 500 mb for the inelastic cross-section of low-energy ^3He nuclei in scintillator was made from the published results of ^3He-^{12}C and ^3He-^1H reactions for ^3He's with energies below 150 MeV (which is in reasonable agreement with Millburn, et. al. [1954], who measured 590(±100)mb for the inelastic cross-section of 315 MeV ^3He nuclei incident on ^{12}C). For σ_{INEL} = 500 mb, a maximum of 3% of the ^3He nuclei, released by the $^6Li(\pi^+,{}^3He)^3He$ reaction at the energies studied, will undergo nuclear interactions in the detectors. Measday and Schneider [1966] have calculated the loss factors for ^4He nuclei stopping in plastic scintillator from previously

published data and showed that 4.13% of 140 MeV ^{4}He's stopping in plastic scintillator undergo nuclear interactions. This number, which is reasonably close to that estimated above for ^{3}He's, drops off sharply with decreasing energy to nearly 1.69% at 80 MeV, an effect which would also be anticipated for ^{3}He.

It is quite possible that a ^{3}He nucleus may generate enough light prior to undergoing a nuclear interaction in scintillator to be identified properly in the off-line analysis. Additionally, as a ^{3}He-^{12}C or ^{3}He-^{1}H nuclear interaction would release ionizing secondary particles, the light output may be similar to that for the non-interacting case. These arguments strongly suggest that only a small fraction of the ^{3}He nuclei estimated to interact in plastic scintillator fail to be detected. The upper limit of the uncertainty associated with nuclear absorption is discussed in Subsection (4.1.2) and Appendix B.

The fraction of ^{3}He nuclei that reach the E counter but generate a signal below the threshold level of the discriminator (and, hence, not be detected) was estimated using the Monte Carlo estimates and the scintillator responses given in Appendix A. This fraction was of the order of 1% or less, and is only significant for the furthest back counters at low pion energies. This effect was neglected.

4 ANALYSIS AND RESULTS

(4.1) Systematic Uncertainties and Dead-Time Corrections

Six major sources of systematic uncertainty in this experiment were identified and estimated, and are detailed in this Section. All errors quoted are rounded up.

(4.1.1) Pion Beam Normalization Uncertainty

The ratios of the pion flux normalized to the $(\mu_1 \cdot \mu_2)$ scaler counts, determined using two independent techniques, are given in Table (I). This Subsection will address the systematic errors associated with the in-beam counting and the ^{11}C activation calibrations. An overall uncertainty will then be assigned to the beam normalization at each energy.

As indicated by equation (3.3), there are four potential sources of error in the calculation of the in-beam calibration ratio R_{IB} : that introduced by the f_π (pion beam fraction) calculation, the pile-up correction factor (P) calculation, the $(IB \cdot \overline{BV})$ scaler count and the $(\mu_1 \cdot \mu_2)$ scaler count. The statistical error due to the $(IB \cdot \overline{BV})$ scaler count was insignificant due to the large number of counts ($> 10^6$) obtained during the calibration. The error in the pile-up correction factor calculation is also insignificant due to

this high number of counts. The error from the $(\mu_1 \cdot \mu_2)$ scaler count statistics is that given in Table (I) and is of the order of 2% or less of the calibration ratio, R_{IB}.

The uncertainty in the f_π calculation arises from the counting statistics of the beam TOF spectrum (e.g., see Figure (12)). f_π is the ratio of the number of pions, N_π, to N_T, the total number of events, in the TOF spectrum,

$$f_\pi = N_\pi / N_T \tag{4.1a}$$

Assuming binomial statistics, the relative uncertainty in f_π is estimated to be,

$$\sigma_{f\pi}/f_\pi = \sqrt{((1-f_\pi)/(f_\pi (N_T-1)))} \tag{4.1b}$$

There was a 1% maximum uncertainty in f_π for a typical TOF spectrum. Summing this result in quadrature with the $(\mu_1 \cdot \mu_2)$ uncertainty gives a maximum systematic error of 3% in R_{IB}.

Those uncertainties quoted in Table (I) for the ^{11}C activation technique incorporate the statistics associated with counting the ^{11}C decays and the error due to fitting the ^{11}C decay curve to an exponential function. The maximum relative error of the ^{11}C activation calibration ratio $R_{^{11}C}$

is 5%.

The values of R_{IB} and $R_{^{11}C}$ given in Table (I) agree with each other to within 7% at 60 MeV, 11% at 80 MeV and 2% at 100 MeV. At 60 and 80 MeV, the disagreements between the R_{IB} and $R_{^{11}C}$ values (7% and 11%, respectively) were assigned as the beam normalization uncertainties at these energies. Despite the 2% agreement between the two calibration results at 100 MeV, the 3% uncertainty of the in-beam counter calibration was defined as the 100 MeV beam normalization maximum uncertainty. For all three energies, the direct pion counting ratio, R_{IB}, was used to calculate the number of pions incident on the target.

(4.1.2) Solid Angle Estimation Uncertainty

The simulation statistics introduced a maximum 6% uncertainty in the Monte Carlo estimation of $\Delta\Omega_{eff}$ (see Appendix B for details). The front telescope, which defined the solid angle, was estimated to be aligned to within ±5 mm of its desired distance from the ^{6}Li target (50 cm). The maximum horizontal and vertical misalignments of the counters within one telescope were estimated to be ±2 mm. These geometrical misalignments introduced a maximum 4% uncertainty in $\Delta\Omega_{eff}$. The maximum uncertainty due to nuclear absorption of the ^{3}He nuclei in a conjugate pair is

(+5%,-0%) and that due to neglecting those trajectories that do not pass entirely through the E counter are (+11%,-0%) (see Appendix B). Summing all the errors in quadrature gives a maximum (+15%,-8%) uncertainty in $\Delta\Omega_{eff}$.

(4.1.3) Efficiency Calibration Uncertainty

As discussed in Section (3.5.2), the $^6Li(\pi^+,{}^3He)^3He$ detection efficiencies were assumed to be 100% on the basis of the measured $\pi^+d \rightarrow 2p$ detection efficiencies. It was estimated that the individual counters had actual $^6Li(\pi^+,{}^3He)^3He$ detection efficiencies of greater than 99%, which translates to a minimum efficiency of 94% for a conjugate pair composed of six coincident counters. Hence, an uncertainty of (+0%,-6%) was assigned to the $^6Li(\pi^+,{}^3He)^3He$ detection efficiency.

(4.1.4) Target Thickness Uncertainty

The ^6Li target was (7.5 x 7.5) cm^2 in area and weighed 6.288 gm. The uncertainty in the dimensions of the target was estimated to be ± 0.1 cm, and that of the weight of the target to be ± 0.001 gm. These yield an overall error in the areal density calculation of less than 3%. The isotopic purity uncertainty was neglected.

(4.1.5) Dead-Time Corrections and Uncertainties

As discussed in Subsection (3.2.3), the $(\mu_1 \cdot \mu_2)$ CAMAC scaler used for beam normalization was not inhibited during the dead-time generated by an event registered in any of the telescope vetoes or in the target holder beam-veto. This dead-time was dependent both upon the beam rate and the size of the beam halo.

The 'fractional dead-time' is defined as the fraction of time that the detector is 'off' due to a generated veto. The fractional dead-time due to only the beam-veto counter is,

$$f_{BV} = (dBV/dt) \cdot \tau_B \tag{4.2a}$$

where (dBV/dt) is the counting rate (in sec^{-1}) of the $(BV_1 + BV_2)$ scaler (which was measured routinely on visual scalers during the data-taking). τ_B is the time separation between beam bursts, 43 nsec. The telescope veto generated fractional dead-time is similarly calculated. For example, that due to the front A-arm veto counter, FAV, is

$$f_{FAV} = (dFAV/dt) \cdot \tau_B \tag{4.2b}$$

During the course of the data-taking, the counting rates of the telescopes' veto counters (e.g., dFAV/dt) were not routinely measured. It was realized near the conclusion of the experiment that the telescope veto dead-times were appreciable. To calculate these dead-times, the telescope veto counting rates had to be known throughout the course of the experiment. Since f_{BV} had been recorded consistently throughout the course of data-taking, the ratios of the telescope veto count to the beam-veto count rate (e.g., FAV/BV) were measured at the end of the experiment. The telescope veto dead-times were then calculated using these ratios and the measured f_{BV} values. For the example of the FAV counter, equation (4.2b) can be rewritten as,

$$\begin{aligned} f_{FAV} &= (dFAV/dt) \cdot \tau_B \\ &= (dBV/dt) \cdot (FAV/BV) \cdot \tau_B \\ &= (FAV/BV) \cdot f_{BV} \end{aligned} \tag{4.2c}$$

Further complications affecting the calculation of these telescope veto dead-times included the fact that the ratios of the telescope veto count to the beam-veto count rate were measured only at T_π = 100 MeV and for front telescope lab

angles of 15°, 45° and 75°. These ratios, by necessity, were used to calculate the 60 and 80 MeV dead-times. The dead-times at 30°, 60° and 90° were calculated using an interpolation discussed below.

The total fraction of time that a conjugate pair is 'off' is due to the dead-times generated by all three vetoes. For the example of the FA-RA conjugate pair, this fractional dead-time is,

$$f_{off} = 1 - (1-f_{FAV})\cdot(1-f_{RAV})\cdot(1-f_{BV}) \qquad (4.2d)$$

The total dead-time percentage loss at 60 MeV was calculated using equation (4.2d) to be less than 6% and less than 10% at 80 MeV. Since these two values were calculated using the assumption that the ratios of the telescope veto count to the beam-veto count rate were independent of pion energy, they were treated as systematic uncertainties in the dead-time losses for 60 and 80 MeV.

At 100 MeV, the measured dead-time percentage losses ranged between 10% and 25%, depending upon the detector angle. That is, with the front detector arm being set at progressively more forward angles, the conjugate rear arm would be set at further back angles. At these angles, the rear telescope could conceivably begin to intercept part of the beam halo thus triggering its veto counter and increasing that conjugate pair's dead-time. Such an hypothesis seems to be substantiated by Figure (13), which shows an increased f_{off} at the more forward angles. As the

100 MeV dead-time losses were measured directly, they were explicitly used to correct the 100 MeV $^6Li(\pi^+,{}^3He){}^3He$ yield. However, these losses were only measured at 15°, 45° and 75°, and explicit values at 30°, 60° and 90° were also required. Interpolating the dead-time loss values at these angles was achieved by parameterizing f_{off} at 100 MeV as a function of the front telescope's lab angle, θ. The function,

$$f_{off} = 1 - f_0(1 - \exp(- \theta / \theta_0)) \qquad (4.3)$$

where f_0 and θ_0 are constants, was found to give a good representation of f_{off}. The measured values of f_{off} at the front telescope angles of 15°, 45° and 75° were least-squares fit to equation (4.3), and the resultant fit and measurements are shown in Figure (13) for f_0 = 0.892 and θ_0 = 8.1° (this calculation is acceptable as the beam rate at 100 MeV during the 30°-60°-90° data-taking runs was the same as that during the 15°-45°-75° runs). The associated fitting error led to estimated uncertainties in f_{off} at 100 MeV of about ±4%. The quantity (1 - f_0) represents the fraction of time the system is 'off' due to the beam-veto dead-time alone (10.8% at 100 MeV).

Figure (13)

Conjugate Pair Fractional Dead-Times vs Front Telescope Lab Angle

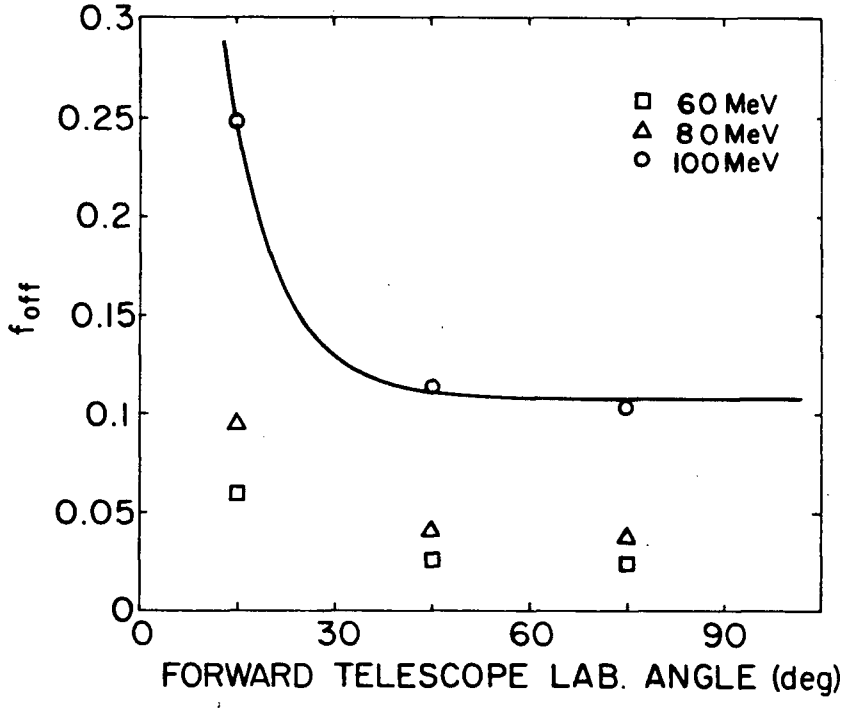

In this figure, the fractional dead-times at 15°, 45° and 75° are plotted for pion energies of 60, 80 and 100 MeV. The 100 MeV results are measured values; the 60 and 80 Mev values shown are based on assumption that the ratio of the telescope veto count rate to the beam-veto count rate is independent of the pion energy. The curve shown is the fit to the 100 MeV data given by equation (4.3).

(4.1.6) Multiple Events

The event logic, as described in Subsection (3.2.3) and shown in Figures (9) and (10), accepted an event for logging on tape only if a valid hardware-defined event was registered in both telescopes of any conjugate pair. It was possible, however, to have events registered in three or more telescopes and have them recorded on tape, provided any two of the telescopes comprised a conjugate pair. Such events amounted to less than 4% of the total number of events.

These events could either be due to real $^{6}Li(\pi^{+},{}^{3}He){}^{3}He$ events associated with random particles entering another telescope, or due to a complex break-up of ^{6}Li or the ^{12}C and ^{16}O contaminants in the polyethylene bag and mineral oil (an estimate of the former effect is discussed below). As this latter possibility could mimic the former due to the limited resolution of the detectors used, any event that occurred in more than two telescopes was simply not considered for further off-line analysis. The 4% figure representing the percentage of the total number of events that 'fired' three or more telescopes was then treated as an asymmetric uncertainty, (+4%,-0%).

The probability of a random particle being associated with a true ^{3}He-^{3}He conjugate event was estimated. For a singles rate 'R' incident on a telescope, the probability of one or more such events occurring during a time interval τ is τR (assuming Poisson statistics and a small τ relative to

R^{-1}). As described in Subsection (3.2.3), scaler tallies were kept of events registering in each telescope singly and in coincidence with its conjugate. These tallies allowed the singles and coincidence rates to be calculated. The maximum singles rate at 60 MeV was 5×10^3 sec^{-1}, 10^4 sec^{-1} at 80 MeV and 3×10^4 sec^{-1} at 100 MeV, and the corresponding coincidence rates were some three orders of magnitude less. Hence, the singles scaler count will be assumed to be essentially a measure of the 'true' singles. The time interval τ is the 10ns window of the event trigger (see Figure (11)). Thus, the maximum probabilities of one or more random events being registered in other telescopes during this window is 5×10^{-5}, 10^{-4} and 3×10^{-4} at 60, 80 and 100 MeV, respectively. These probabilities are two to three orders of magitude less than the fraction of events observed as multiples. This would seem to suggest that the multiple events registered were due to the break-up of ^6Li, ^{12}C and ^{16}O nuclei.

A summary of all of the estimated systematic errors and the quadrature sums is given in Table (III) as a function of pion energy.

TABLE (III) Maximum Systematic Errors (Estimated)

Error Source	Pion Energy		
	60 MeV	80 MeV	100 MeV
Beam Normalization	±7%	±11%	±3%
$\Delta\Omega$ Estimation	+15% -8%	+15% -8%	+15% -8%
Efficiency * Calibration	+0% -6%	+0% -6%	+0% -6%
Target Thickness	±3%	±3%	±3%
Dead-Time Loss	+6% -0%	+10% -0%	±4%
Multiple Events	+4% -0%	+4% -0%	+4% -0%
Quadrature ** Sum	+18% -13%	+22% -16%	+17% -12%

* - for a conjugate pair
** - Rounded up

(4.2) Results and Discussion

(4.2.1) Extraction of ^{3}He Yields

The ^{3}He yield from the data was determined using the FIOWA multidimensional analysis code, which is an extension of the older KIOWA code [Stetz, 1975]. FIOWA allows an event-by-event off-line analysis of the data on tape and permits event selection using software cuts. As discussed in Subsection (4.1.6), only those events which satisfied a pure 'back-to-back' configuration (i.e., in which an event is registered in one conjugate telescope pair only) were accepted for further off-line analysis. Such a configuration was identified by examining the Ortec C212 bit pattern associated with each event.

In order to extract the ^{6}Li(π^+,^{3}He)^{3}He events, software cuts on the ADC spectra were used to reject the background events in both telescopes of a conjugate pair. The approximate range of ADC channels of the ^{3}He peaks were estimated using the Monte Carlo calculation of the ^{3}He energy loss in the counters, the measured π^+d -> 2p calibration response and the calculated correction for the non-linearity of the NE-102 scintillator (as described in Subsection (3.5.1)). A candidate event was chosen by its having an ADC value appropriate for ^{6}Li(π^+,^{3}He)^{3}He in all six counters of a conjugate pair. For example, in Figure (14) ΔE_1 vs E ADC scatterplots are shown at

T_π = 80 MeV for a telescope pair with the front arm at a lab angle of 30° and the rear arm at the kinematic conjugate angle, -143°. Loose software 'slope' cuts (like that shown) have been applied to both scatterplots in order to remove the bulk of the background events with low ΔE_1, ΔE_2 and E ADC values (predominantly protons). In both arms, the band of events that may be attributed to Z=2 particles is readily apparent, as is the group of $^6Li(\pi^+,{}^3He)^3He$ events.

In Figure (15), a cross-correlation (rear E vs front E ADC) scatterplot of these same events (with the same cuts) is shown. The $^6Li(\pi^+,{}^3He)^3He$ events form a distinct group that is separable from other events. This cross-correlation plot also shows evidence for another π^+-^6Li reaction channel that yielded a ^3He nucleus in the front arm and a non-^3He particle in the rear arm. This latter event type is perhaps the signature of a more complicated π^+-^6Li reaction channel and is discussed in detail in Subsection (4.2.5). Analyzing solely the ΔE_1 (or ΔE_2) vs E ADC scatterplots would have made the identification and exclusion of this type of non-$^6Li(\pi^+,{}^3He)^3He$ event difficult. Hence, as shown here, the cross-correlation scatterplot was an integral tool in the analysis.

Figure (14)

ΔE_1 vs E ADC Scatterplots for Front and Rear Telescopes at a Pion Energy of 80 MeV and Front Telescope Lab Angle of 30^0

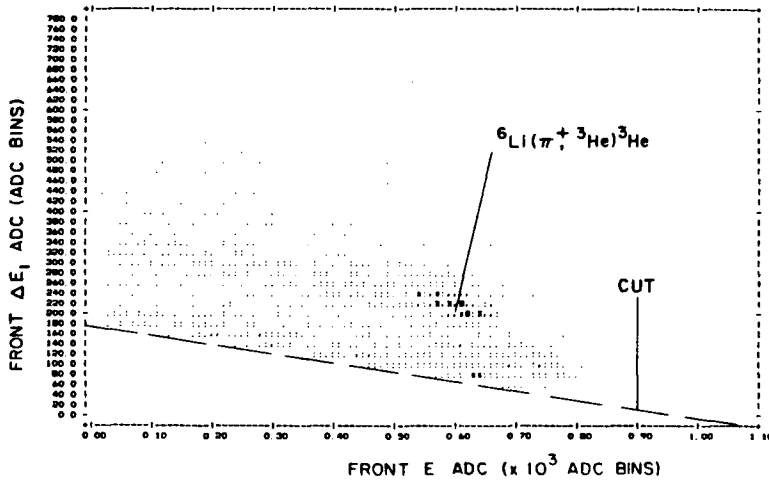

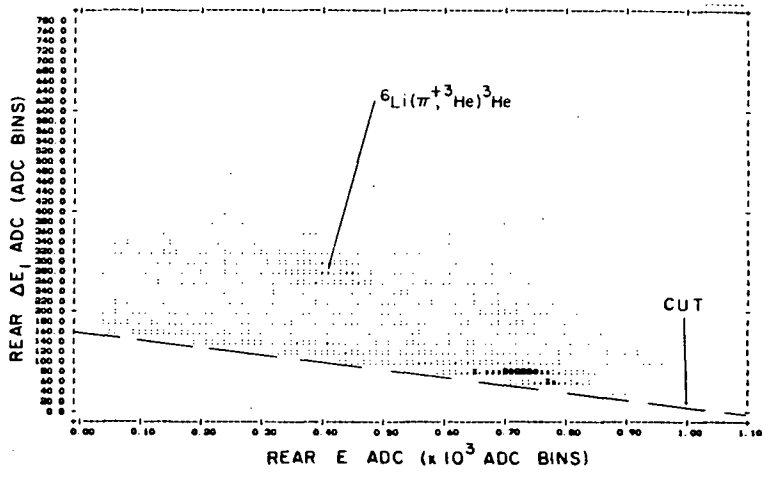

Software cuts have been applied to reject the bulk of the background events.

Figure (15)

Rear E vs Front E ADC Cross-Correlation Scatterplot at a Pion Energy of 80 MeV and Front Telescope Lab Angle of 30°

(Same software cuts as in Figure (14))

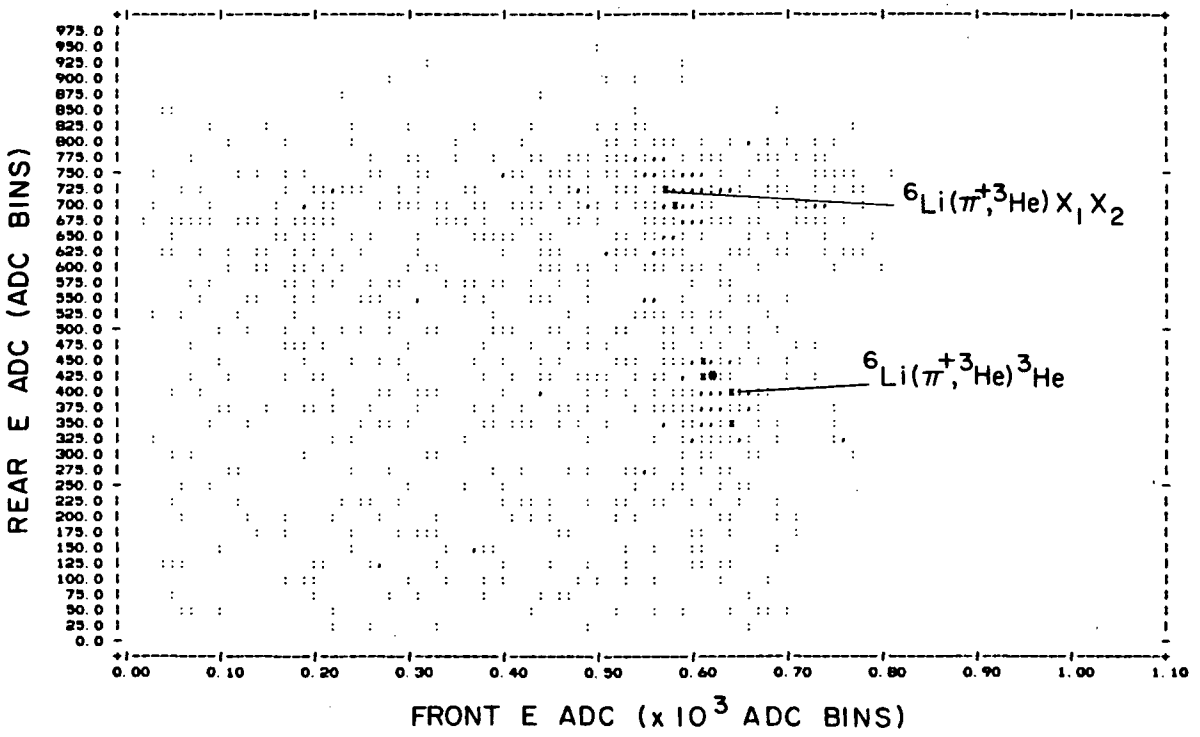

The $^6Li(\pi^+,{}^3He)^3He$ events form a distinct group. The $^6Li(\pi^+,{}^3He)X_1X_2$ events, with a ^3He in the Front arm and a non-^3He particle in the Rear arm, are perhaps due to a more complicated π^+-^6Li reaction channel. Such events are discussed in Subsection (4.2.5)

By testing this cross-correlation and sequentially applying a large number of increasingly restrictive conjugate cuts (such as the slope cut shown in Figure (14) and cuts on the individual counters' ADC spectra), the conjugate ^{3}He groups could be eventually isolated. In Figure (16), the three-dimensional ΔE_1 vs E ADC scatterplots for the conjugate arms for more restrictive cuts than those of Figures (14) and (15) are shown. Just enough of the Z=2 band is left to display the relative 'signal-to-noise ratio' of the ^{6}Li(π^+,^{3}He)^{3}He events to the background Z=2 events. To get the final ^{3}He yield, cuts are placed around the peaks in these two scatterplots (and in the front and rear ΔE_2 vs E ADC and rear E vs front E ADC scatterplots) in order to isolate the ^{6}Li(π^+,^{3}He)^{3}He events. The number of ^{3}He-^{3}He pairs that remain within these peaks is then counted.

With the software cuts centered on the ^{6}Li(π^+,^{3}He)^{3}He peaks still in place, the background target runs (with only the polyethylene bag and mineral oil) were then analyzed in order to extract the relative number of ^{3}He-^{3}He pairs that were actually due to π^+ absorption on the background target constituents.

Figure (16)

Three-Dimensional ΔE_1 vs E Scatterplots for Front and Rear Telescopes at a Pion Energy of 80 MeV and Front Telescope Lab Angle of 30^0

(With more restrictive software cuts than those in Figures (14) and (15))

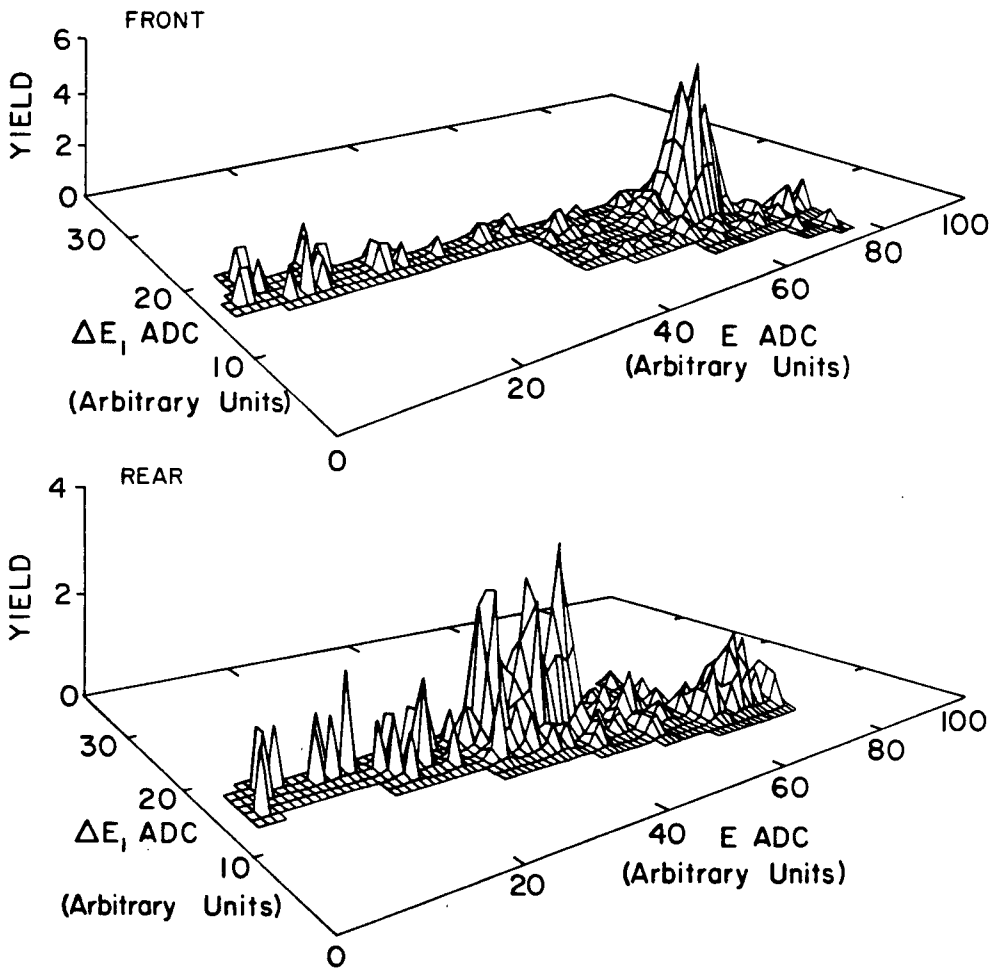

The $^6Li(\pi^+, {}^3He)^3He$ peaks are readily visible among the Z=2 continuum events.

(4.2.2) Angular Dependence of the $^6Li(\pi^+,{}^3He)^3He$ Differential Cross-Section at 60, 80 and 100 MeV

The $^6Li(\pi^+,{}^3He)^3He$ center-of-mass differential cross-sections were calculated from the measured ^3He yields using the equation,

$$d\sigma/d\Omega^* = N_{^3He}(1-B) / \{R_{IB} N_{\mu} \rho_{eff} (1-f_{off}) J(d\Omega) \Delta\Omega_{eff}\} \quad -(4.4a)$$

where $N_{^3He}$ is the measured yield of ^3He-^3He fission pairs. B is the fraction of these pairs attributed to events originating from non-^6Li material, such as the pion-induced break-up of the ^{12}C and ^{16}O nuclei in the mineral oil and the polyethylene bag covering the ^6Li target. Including this (1-B) factor in equation (4.4a) is a formality as no events were registered that satisfied the software cuts selecting the $^6Li(\pi^+,{}^3He)^3He$ spectrum in the background target analysis. R_{IB} is the calibration ratio determined from the in-beam counter normalization method for the appropriate pion energy (see Table (I)) and N_{μ} is the $(\mu_1 \cdot \mu_2)$ telescope scaler total for the analyzed runs. The product $(R_{IB} N_{\mu})$ is the number of pions incident on the ^6Li target. ρ_{eff} is the ^6Li effective areal density in nuclei/cm^2,

$$\rho_{eff} = \sqrt{2} \cdot \rho \qquad (4.4b)$$

where ρ is the actual areal density and the $\sqrt{2}$ factor comes from the 45° target angle with respect to the beam axis. $(1 - f_{off})$ is the fraction of time the conjugate telescope pair is 'on'; at 60 and 80 MeV, f_{off} was set equal to zero and the estimated fraction of events lost due to the detection system's dead-times was treated as a systematic uncertainty, as described in Subsection (4.1.5). At 100 MeV, equation (4.3) was used to explicitly calculate this $(1 - f_{off})$ factor. $\Delta\Omega_{eff}$ is the conjugate pair's effective lab solid angle, calculated by the Monte Carlo code. $J(d\Omega)$ is the Jacobian of the solid angle transformation between the lab and center-of-mass frames,

$$J(d\Omega) = d\Omega^* / d\Omega_{lab} \qquad (4.4c)$$

and is calculated from the reaction kinematics. For example, its value at T_π = 60 MeV and at a lab angle of 15° is 1.20.

The differential cross-sections determined using equation (4.4a) for the measured ^{3}He yields are tabulated in Tables (IV), (V) and (VI) for T_π = 60, 80 and 100 MeV. (preliminary values for the 60 and 80 MeV differential cross-sections have been presented in McParland, et. al., [1985]). The errors given are statistical only and are for a

68.3% confidence interval; estimates of the systematic uncertainties are given in Table (III). At some angles, small numbers of events were obtained which did not permit a Gaussian approximation to be used for the data distribution. In these cases, the Poisson distribution is used which generates asymmetric errors about the mean [Helene, 1984]. Angular distributions of $d\sigma/d\Omega^*$ at each pion energy are plotted in Figures (17), (18) and (19) as functions of $\cos^2\theta^*$ because of the identical particle nature of the ^{3}He's and the subsequent reaction symmetry about $\theta^* = 90^\circ$.

TABLE (IV)

^{6}Li(π^+,^{3}He)^{3}He Differential Cross-Sections (60 MeV)

θ (Lab) (degrees)	θ^* (degrees)	$d\sigma/d\Omega^*$ (nb/sr)
15	16.5	391.9 ± 42
30	32.8	269.4 ± 32
45	49.0	179.9 ± 24
60	64.9	141.4 ± 24
75	80.5	61.8 (+19,-16)
90	95.7	89.8 (+22,-19)

TABLE (V)

$^6Li(\pi^+,{}^3He)^3He$ Differential Cross-Sections (80 MeV)

θ (Lab) (degrees)	θ^* (degrees)	$d\sigma/d\Omega^*$ (nb/sr)
15	16.7	189.5 ± 17
30	33.2	124.8 ± 13
45	49.5	76.2 ± 10
60	65.6	36.4 ± 8
75	81.2	46.3 ± 9
90	96.4	34.5 (+9,-8)

TABLE (VI)

$^6Li(\pi^+,{}^3He)^3He$ Differential Cross-Sections (100 MeV)

θ (Lab) (degrees)	θ^* (degrees)	$d\sigma/d\Omega^*$ (nb/sr)
15	16.8	60.3 ± 8
30	33.5	49.4 ± 5
45	50.0	17.5 ± 4
60	66.1	7.9 ± 2
75	81.8	11.6 (+4,-3)
90	97.0	3.1 ± 1

Figure (17)

Angular Distribution of the $^6Li(\pi^+,{}^3He)^3He$ Differential Cross-Section at 60 MeV

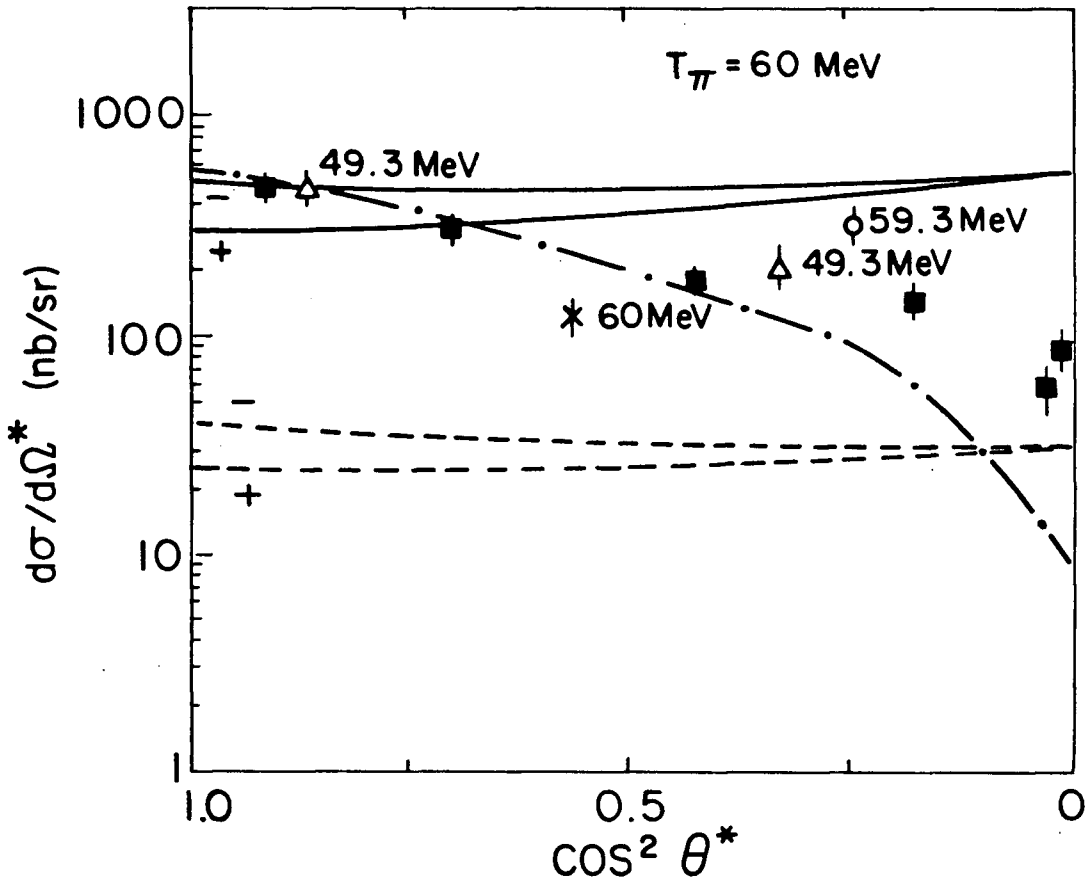

■: this work
Δ: Saclay data [LeBornec, et. al., 1983]
o: LAMPF data [Barnes, et. al., 1983]
X: previous TRIUMF data [Lolos, et. al., 1983]

Full Curve : GW Woods Saxon calculation
Dashed Curve : GW Harmonic-Oscillator calculation
(+/- refer to relative signs of imaginary components of the complex variables used in the $^3He(p,\pi^+)^4He$ parameterization)

Dot-Dash : EB calculation

Errors shown are statistical only and are for a 68.3% confidence interval.

Figure (18)

Angular Distribution of the $^6Li(\pi^+, {}^3He)^3He$ Differential Cross-Section at 80 MeV

(Symbols are the same as in Figure (17))

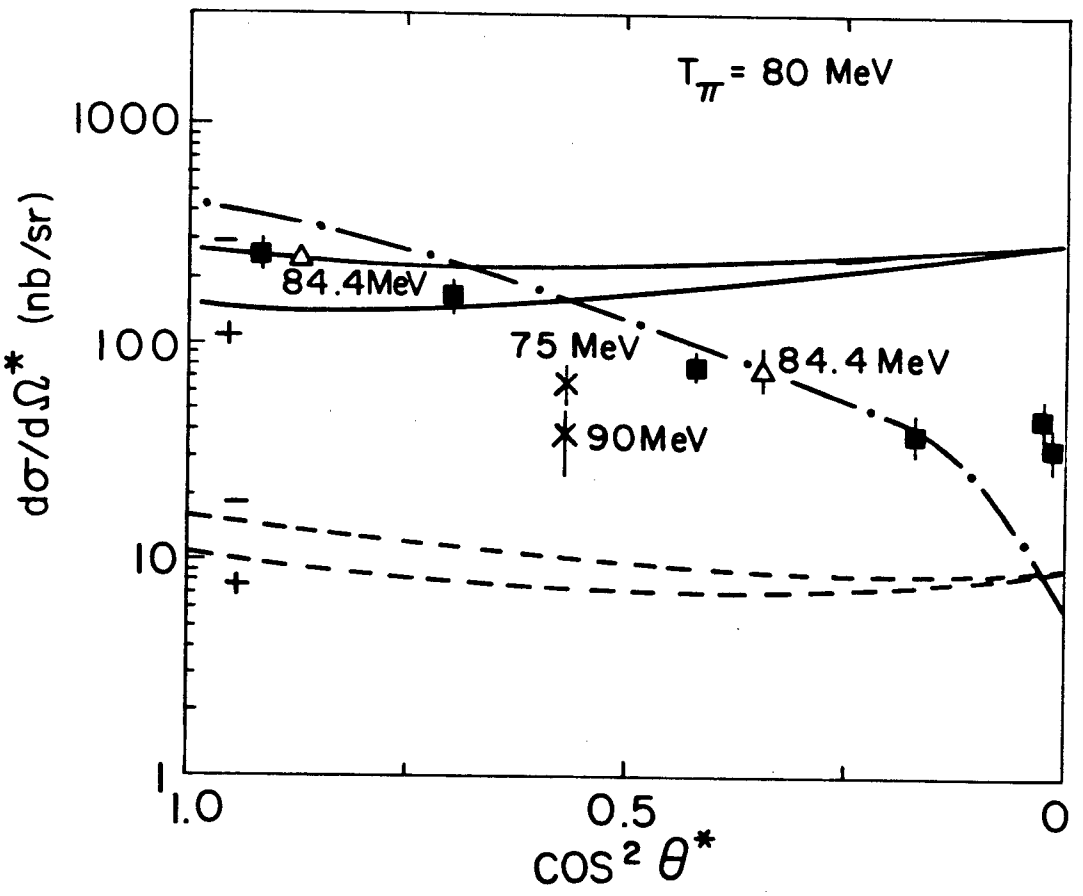

Figure (19)

Angular Distribution of the $^6Li(\pi^+, {}^3He)^3He$ Differential Cross-Section at 100 MeV

(Symbols are the same as in Figure (17))

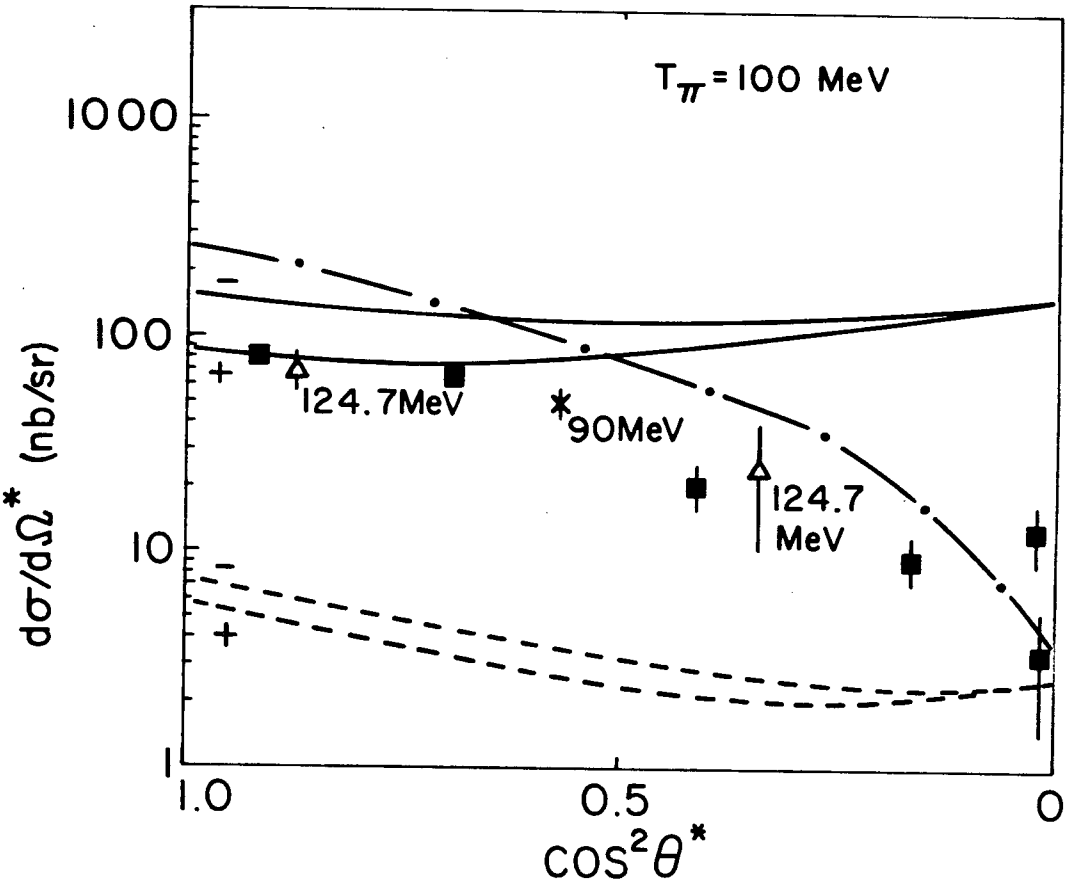

Data from the Saclay measurements of the $^3He(^3He,\pi^+)^6Li(g.s.)$ reaction [LeBornec, et. al., 1983] have been transformed via detailed-balance (using equation (2.11)) and are included, along with the equivalent pion energies, for comparison. Data from LAMPF [Barnes, et. al., 1983] and TRIUMF [Lolos, et. al., 1983], at the same or similar pion energies, are also plotted. The center-of-mass differential cross-sections measured here exhibit a smooth exponential decrease with decreasing $\cos^2\theta^*$ (or increasing momentum-transfer). The LAMPF data point at 59.3 MeV is about three standard deviations greater than that expected from our 60 MeV data. Conversely, the old TRIUMF data point at 60 MeV is about five standard deviations less. The differences between the data measured here, the LAMPF data and the older TRIUMF result are believed attributable to the inherent difficulty in measuring a low cross-section pion absorption reaction in a counter experiment.

The curves shown in these figures correspond to the Erlangen-Bonn and Germond-Wilkin theoretical calculations. The GW curves are for the harmonic-oscillator and Woods-Saxon forms used to describe the ^6Li nuclear wavefunction. As noted in Section (2.2), there is an uncertainty in the relative signs of the imaginary parts of the two complex variables used to parameterize the $^3He(p,\pi^+)^4He$ input data. This ambiguity further splits each GW calculation into two subsets (+ and -) corresponding to the relative signs. Comparing the theory with data, the

Erlangen-Bonn curves, overall, appear to give a qualitatively better representation of the shape of the angular distributions at these three energies than do the Germond-Wilkin curves. It is worthwhile to note the following points that result from a comparison between the data and the two theories :

(1) The quantitative discrepancy between the EB model and the data, at the forward angles, increases with pion energy. As T_π is raised, the predicted Erlangen-Bonn angular distribution begins to overestimate the data over most of the range of $\cos^2\theta^*$.

(2) The GW Woods-Saxon curves give a generally good representation of the data for all three energies at the forward angles (i.e. $\cos^2\theta^* > 0.75$ or $\theta^* < 30^\circ$), but do not predict the steep dependence of the data upon $\cos^2\theta^*$. No real distinction can be made between the two subsets (+ or -) of the Woods-Saxon prediction.

(3) The GW harmonic-oscillator curves greatly underestimate the cross-section, although they do approach the measurements at the back angles. The measured angular distributions straddle the two GW wavefunction type predictions (see Section (2.3) for a discussion of Woods-Saxon vs. harmonic-oscillator wavefunctions).

Another useful feature to examine is the energy dependence of $d\sigma/d\Omega^*$ at a fixed center-of-mass angle ('excitation function'). Since the detectors were set at fixed lab angles which, of course, corresponded to different CMS angles with differing pion energies, the differential cross-section had to be interpolated between these angles in order to determine the value of $d\sigma/d\Omega^*$ at a fixed CMS angle. This interpolation was made by first fitting the data to an analytical function which is described in the next subsection. Such a function will be shown to generate some interesting results of its own.

(4.2.3) Legendre Polynomial Fits to Data

The differential cross-section for $^6Li(\pi^+,{}^3He)^3He$ may be written as a series of even-order orthogonal Legendre polynomials. This polynomial type was selected because of the relative insensitivity of the series coefficients to the order of the series truncation [Niskanen, 1980; Jones, 1982] and, because of the reaction's symmetry about $\theta^* = 90^\circ$, the expansion is restricted to only the even-ordered polynomials.

As only six data points were measured per angular distribution, the series was limited to three terms. The measured differential cross-sections were least-squares fit to the form,

$$4\pi\cdot(d\sigma/d\Omega^*) = a_0 + a_2P_2(u) + a_4P_4(u);\ u = \cos\theta^* \qquad (4.5a)$$

The Legendre polynomials, P_i, have the normalization,

$$\int_{-1}^{1} P_m(u)P_n(u)\,du = 2/(2m+1)\ \delta_{mn} \qquad (4.5b)$$

where δ_{mn} is the Kronecker delta function.

The 4π normalization factor in equation (4.5a) allows the total reaction cross-section to be extracted directly from the fit,

$$\sigma_T = a_0 / 2 \qquad (4.5c)$$

where a_0 must be divided by two because of the indistinguishability between the two exiting ^{3}He nuclei.

At Orsay, the ^{3}He(^{3}He,π^+)^{6}Li(g.s.) reaction was measured at center-of-mass angles of 30.8°, 60.3° and 87.3° at a ^{3}He energy of 282 MeV, which corresponds to a pion energy of 15.4 MeV in the ^{6}Li(π^+,^{3}He)^{3}He direction [LeBornec, et. al., 1981]. These three points were transformed by detailed-balance to yield ^{6}Li(π^+,^{3}He)^{3}He cross-sections and were then fit to the Legendre polynomial series,

$$4\pi\cdot(d\sigma/d\Omega^*) = a_0 + a_2P_2(u);\ u = \cos\theta^* \qquad (4.5d)$$

Because only three measurements were available, the expansion was truncated at two terms.

In Table (VII), the a_2 and a_4 terms, normalized to a_0, the χ^2/ν of the fit (where ν is the number of degrees of freedom) and σ_T are given for each pion energy. In Figure (20), the fits given by equation (4.5a) for the 60, 80 and 100 MeV data and the data points are plotted along with the data against $\cos^2\theta^*$. The requirement of the a_4 coefficient for fitting the 60, 80 and 100 MeV data was tested by fitting that data to the two-coefficient Legendre polynomial expansion of equation (4.5d). The χ^2/ν of these two-coefficient fits are also given in Table (VII). These latter χ^2/ν values are larger than those for the three-coefficient fits of equation (4.5a), thus indicating the need for the a_4 coefficient.

The coefficients a_2 and a_4, normalized to a_0, are plotted against the pion beam energy in Figure (21). Dividing by a_0 normalizes a_2 and a_4 to the total reaction cross-section. Of course, only the a_2/a_0 ratio is available from the Orsay fit. In Figure (22), the reaction total cross-section, σ_T, calculated from equation (4.5c), is also plotted against incident pion energy.

The monotonic increase of the ratios a_2/a_0 and a_4/a_0 with the incident beam energy in Figure (21) can be attributed to the introduction of higher order partial waves

with rising energy. A non-zero a_2 coefficient indicates the presence of p-wave pions and a non-zero a_4 coefficient is indicative of d-wave pions. For 60, 80 and 100 MeV, the a_2 term is larger than both the a_0 and a_4 terms. It appears that the a_4 term is not significant below 60 MeV. At 15.4 MeV, the a_0 term now exceeds a_2.

In Figure (22), σ_T appears to exhibit a simple exponential decrease with increasing T_π. This feature is discussed in the next Subsection.

TABLE (VII)

Summary of Legendre Polynomial Fits

Pion Energy (MeV)	Ratios of Coefficients		χ^2/ν of fit	σ_T (nb)
	a_2/a_0	a_4/a_0		
(*) 15.4	0.643 (0.161)	(**) ---	1.86	13609 (1019)
60	1.250 (0.165)	0.192 (0.190)	1.10 (1.20)	1062.9 (67)
80	1.402 (0.159)	0.562 (0.184)	0.71 (2.95)	464.8 (27)
100	2.149 (0.251)	0.595 (0.224)	1.84 (3.21)	129.5 (10)

- Quantities in brackets (except for χ^2/ν) are $\pm 1\sigma$.

- Quantities in brackets in χ^2/ν column are those χ^2/ν values for a fit to only a_0 and a_2 terms.

(*) - Equivalent pion energy

(**) - Orsay data for $^3He(^3He,\pi^+)^6Li(g.s.)$ transformed via detailed-balance, [LeBornec, et. al., 1981]; fit only to a_0 and a_2 terms.

Figure (20)

Angular Distributions of the $^6Li(\pi^+, {}^3He)^3He$ Differential Cross-Section at 60, 80 and 100 MeV and Legendre Polynomial Fits

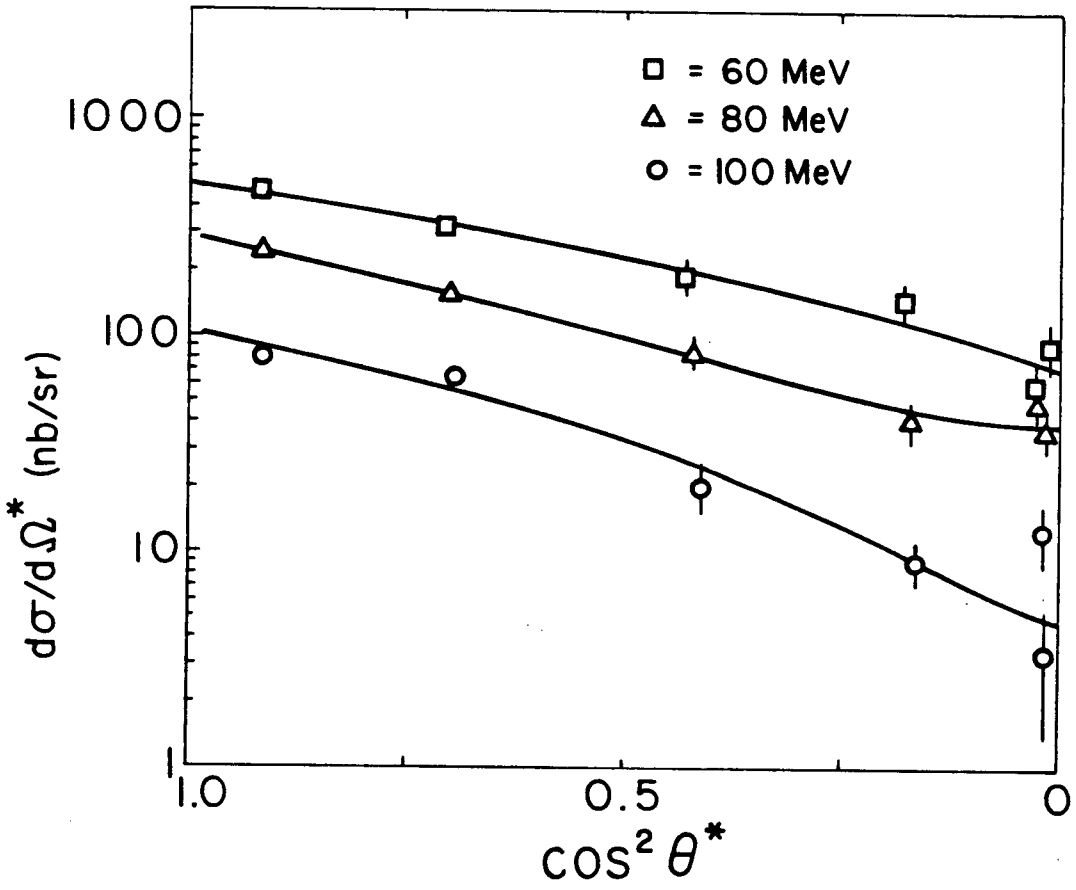

Figure (21)

Ratios of Legendre Polynomial Coefficients vs Incident Pion Beam Energy

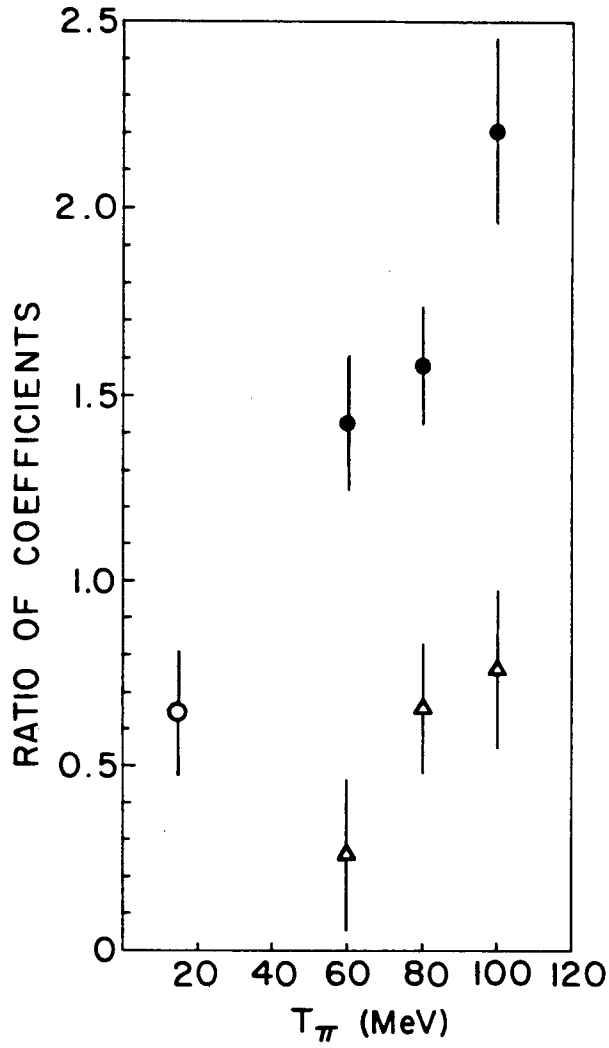

•: a_2/a_0 from this work
o: a_2/a_0 from LeBornec, et. al., [1981]
Δ: a_4/a_0 from this work

Figure (22)

$^6Li(\pi^+,{}^3He)^3He$ Total Reaction Cross-Section vs Incident Pion Beam Energy

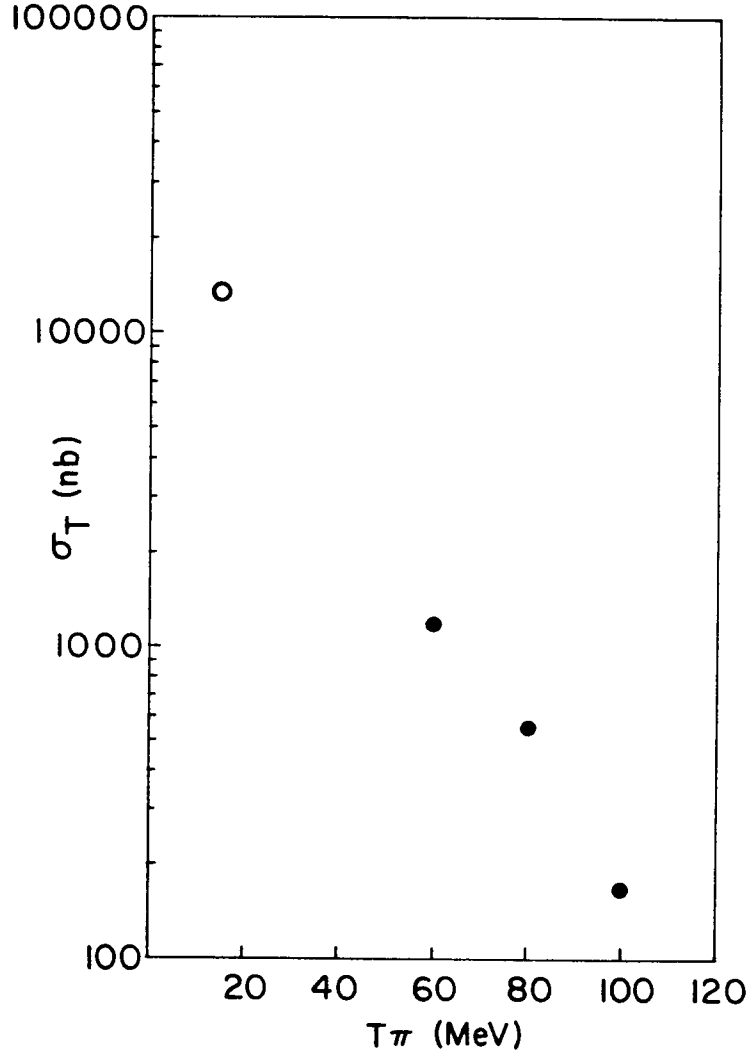

•: this work
o: from LeBornec, et. al., [1981]
(Statistical error bars are smaller than the symbols)

(4.2.4) Energy Dependence of the $^6Li(\pi^+,{}^3He)^3He$ Differential Cross-Section at $\theta^* = 15^\circ$, 45° and 90°

Using the Legendre polynomial expansions of equations (4.5a) and (4.5d), and the coefficients in Table (VII), the interpolated differential cross-sections at $\theta^* = 15^\circ$, 45° and 90° were calculated for $T_\pi = 15.4$, 60, 80 and 100 MeV. These are plotted against pion energy for each of the three angles in Figures (23), (24) and (25), along with the predicted excitation functions calculated by the Erlangen-Bonn and Germond-Wilkin models. The data point at $T_\pi = 39$ MeV and $\theta^* = 90^\circ$ is a measurement from the LAMPF experiment [Barnes, et. al., 1983].

Of particular interest in Figures (22), (23), (24) and (25) is the exponential-like dependence of the total and center-of-mass differential cross-sections upon the incident pion beam energy. The cross-sections from this thesis and the Orsay 15.4 MeV data were least-squares fit to an exponential function of the form,

$$k \exp(-T_\pi/T_0)$$

The slope parameter, T_0, is given in Table (VIII) for σ_T and for the center-of-mass differential cross-sections at center-of-mass angles of 15°, 30°, 45°, 60°, 75° and 90°.

The extracted T_0 from the differential cross-sectioins decreases with increasing angle (or increasing momentum-transfer). Unfortunately, it is not yet known if there is a connection between this systematic feature and the reaction mechanism.

The features resulting from the comparison between the data and the theories can be summarized :

(1) The GW Woods-Saxon curves give a fairly good representation of the 60, 80 and 100 MeV fitted data at $\theta^* = 15^\circ$. This agreement deteriorates at 45°, although the slope is still fairly well approximated. At $\theta^* = 90^\circ$, there is no ambiguity between the + and - subsets of the calculation. The Woods-Saxon curve at this angle overestimates the data from 39 MeV on, by about an order of magnitude.

(2) The EB prediction overestimates the 80 and 100 MeV points at 15° and 45°, but agrees with the 60 MeV value at both of these angles rather well.

Figure (23)

Energy Dependence of the $^6Li(\pi^+, {}^3He)^3He$ Differential Cross-Section at $\theta^* = 15^0$

(All the points are calculated from the Legendre polynomial fits of equations (4.5a) or (4.5d))

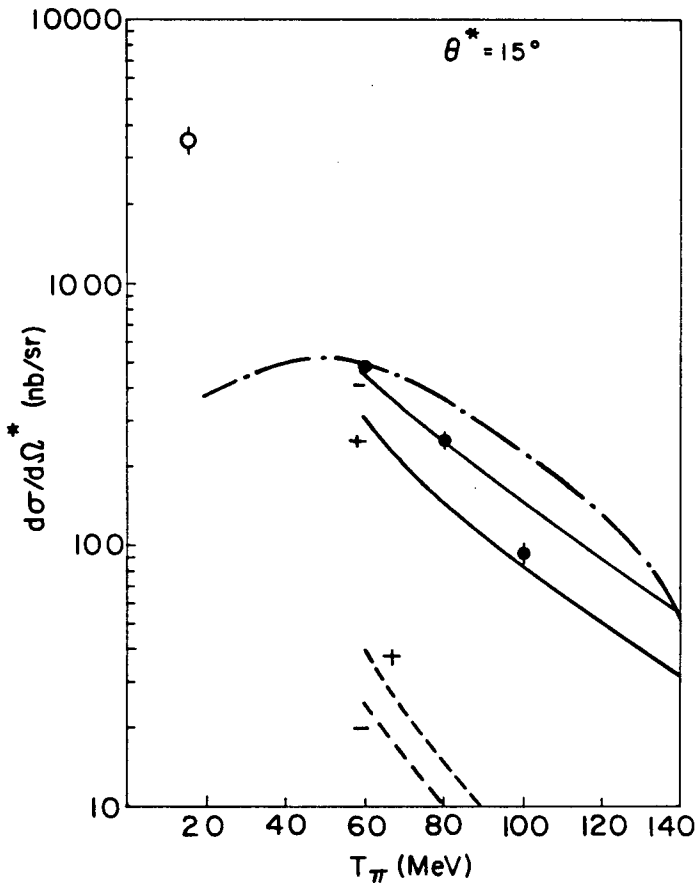

•: this work
o: from LeBornec, et. al., [1981]

(Curves are the same as in Figure (17))

Figure (24)

Energy Dependence of the $^6Li(\pi^+, {}^3He)^3He$ Differential Cross-Section at $\theta^* = 45^0$

(All the points are calculated from the Legendre polynomial fits of equations (4.5a) or (4.5d))

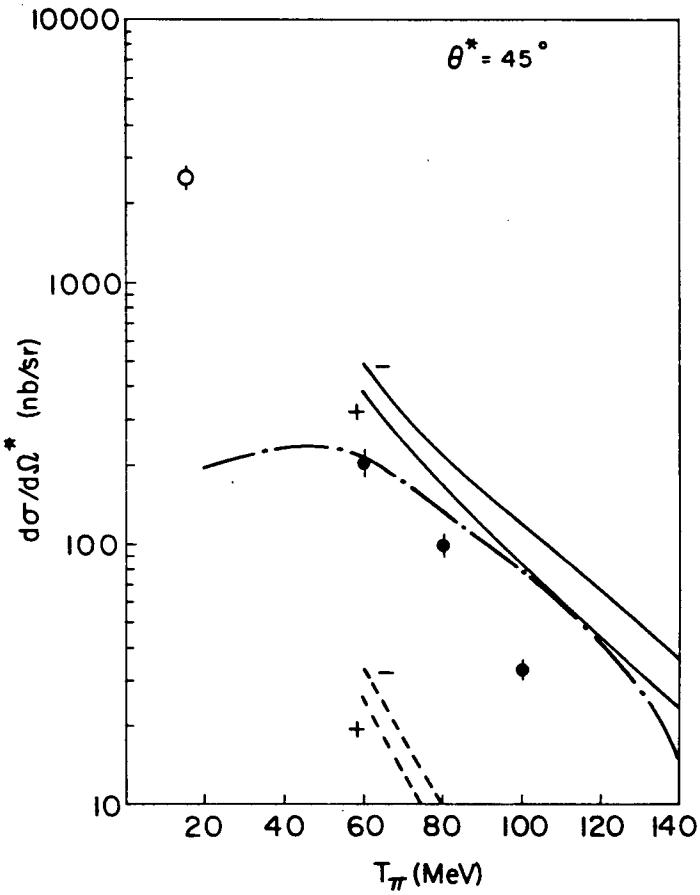

•: this work
o: from LeBornec, et. al., [1981]

(Curves are the same as in Figure (17))

Figure (25)

Energy Dependence of the $^6Li(\pi^+,{}^3He)^3He$ Differential Cross-Section at $\theta^* = 90^0$

(All the points are calculated from the Legendre polynomial fits of equations (4.5a) or (4.5d); except that at $T_\pi = 39$ MeV)

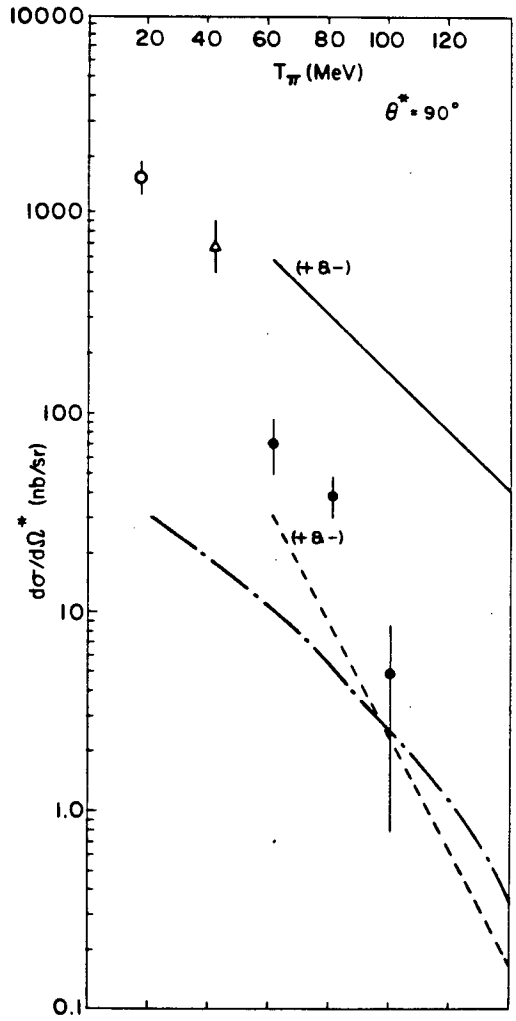

•: this work
o: from LeBornec, et. al., [1981]
Δ: measured datum from Barnes, et. al., [1983]

(Curves are the same as in Figure (17))

TABLE (VIII)

Summary of Slope Parameters

θ^* (°)	T_0 (MeV)	χ^2/ν of fit
15	22.1 (0.7)	2.5
30	20.9 (0.6)	2.8
45	18.7 (0.5)	0.8
60	16.8 (0.5)	0.9
75	15.7 (0.7)	3.0
90	15.7 (1.0)	2.3
σ_T	18.5 (0.4)	4.7

- Quantities in brackets are $\pm 1\sigma$.

(3) The Erlangen-Bonn curve peaks at about $T_\pi = 50$ MeV for the 15° and 45° angles. Such a peaking, which reflects the model's accounting for the presence of the Δ_{33} resonance within the nucleus, is no longer visible at $\theta^* = 90^\circ$. From the data points, there is no obvious indication of such a peaking at any of the three angles.

(4.2.5) Possible Evidence for ^3He-^2H Coincidences

The ^3He-^3He outgoing channel represents only a small fraction of the possible π^+-^6Li reaction channels, as exemplified by the measured branching ratios ranging between 2×10^{-4} and 6.5×10^{-4} for the charge-symmetric $^6Li(\pi^-,{}^3H)^3H$ reaction at threshold. Other possible fission modes include the prominent $^6Li(\pi^+,2p)^4He$ reaction, where the pion is absorbed on a correlated p-n pair in the ^6Li nucleus, mimicking a $\pi^+d \rightarrow 2p$ process, while the ^4He cluster acts as a spectator [Arthur, et. al., 1975]. Measurements of the $^7Li(\pi^+,{}^3He)^3He+n$ and $^7Li(\pi^+,{}^3He)^3H+p$ reactions at 59.3 MeV [Barnes, et. al., 1983] have suggested that there is an enhancement in the reaction yield corresponding to that region of phase space where the single nucleon is at rest and all of the momentum is carried away by the two clusters. Of particular interest, though, was the observation that the $^7Li(\pi^+,{}^3He)^3He+n$ yield was only about 25% that of its analog $^7Li(\pi^+,{}^3He)^3H+p$.

At SIN, Sennhauser, et. al. [1982], observed single and coincident charged particles resulting from π^- absorption on ^{6}Li and ^{7}Li. There was clear evidence in the ^{3}H energy spectrum from ^{6}Li(π^-,^{3}H)X_1X_2 for π^- absorption on the ^{4}He cluster with a quasideuteron acting as a spectator. There was even a further suggestion that π^- absorption on a ^{5}He cluster was detected, with the proton acting as a spectator. A yield of 0.0109(±0.0023) triton-deuteron coincident pairs (with energies greater than 20 MeV) per stopped pion was measured. The features of pion absorption on the lithium isotopes, as measured at LAMPF and SIN, suggest that a complex and interesting variety of exit channels are available in π^+ absorption on ^{6}Li in addition to the ^{6}Li(π^+,^{3}He)^{3}He binary fission studied in this thesis.

Germond and Wilkin [1982a, 1984] have remarked on the requirement for a ^{6}Li(π^+,^{3}He)^{3}He theoretical model to be able to explain the ^{6}Li(π^+,^{3}He)^{2}H+p channel. In fact, if one considers the measured SIN branching ratios of 0.065% and 1.09% for the ^{6}Li(π^-,^{3}H)^{3}H and ^{6}Li(π^-,^{3}H)^{2}H+n fission modes, respectively, then one could surmise that the fission ^{6}Li(π^+,^{3}He)^{2}H+p is significantly more probable than the ^{6}Li(π^+,^{3}He)^{3}He channel.

Although the detector angles, event logic and discriminator threshold settings for this experiment were optimized and set for the ^{6}Li(π^+,^{3}He)^{3}He reaction, and the resolution and non-linear response of the NE-102 scintillator would make discrimination between protons and deuterons of arbitrary energy difficult, an attempt was made

to see if evidence for this $^6Li(\pi^+,{}^3He)^2H+p$ process was present among the data recorded on tape (as discussed in Subsection (4.2.1), there were indications noted of ^3He nuclei coincident with another type of particle). The signature of this channel would be a ^3He detected in one telescope in coincidence with either a proton or a deuteron in the conjugate telescope.

As an example, Figure (26) shows the ΔE_1 vs E ADC scatterplots for the front and rear arms at $T_\pi = 60$ MeV and for the front arm at 15^0. Loose software cuts have been applied to reject low ΔE_1, ΔE_2 and E background events.

The coincident ^3He-^3He events are readily apparent. Of interest, though, is a second grouping, in the front arm ΔE_1 vs E scatterplot, at a higher E ADC and lower ΔE_1 ADC channel than the $^6Li(\pi^+,{}^3He)^3He$ events. In the conjugate rear arm ΔE_1 vs E ADC scatterplot, there is another diffuse grouping of events separated from the $^6Li(\pi^+,{}^3He)^3He$ events. These latter two clusters are clearly not ^3He-^3He fission pairs, but are presumably protons or deuterons, although the detector resolution does not permit a conclusive identification.

In Figure (27), a cross-correlation plot of the rear vs front E counter ADC spectra is given for the same pion energy, detector angle and software cuts. Three peaks are obvious. The first consists of coincident ^3He-^3He pairs and is easily associated with the $^6Li(\pi^+,{}^3He)^3He$ reaction. The second peak is apparently due to coincident protons in both arms and could indicate a $(\pi^+,2p)$ process on ^6Li with the

protons depositing enough energy in the counters to exceed the discriminator threshold settings while also not being energetic enough to reach the telescopes' veto counters. The third peak, which smears into this (π^+,2p) peak, is composed of events which yield a ^{3}He in the front telescope and a non-^{3}He particle in the rear telescope. This latter particle yields a scintillator response about three times that of the ^{3}He from ^{6}Li(π^+,^{3}He)^{3}He. This peak is strongly suggestive of ^{6}Li(π^+,^{3}He)^{2}H+p, although it is not at all clear if the rear arm is detecting the deuteron or the proton.

Figure (26)

ΔE_1 vs E ADC Scatterplots for Front and Rear Telescopes at a Pion Energy of 60 MeV and Front Telescope Lab Angle of 15^0

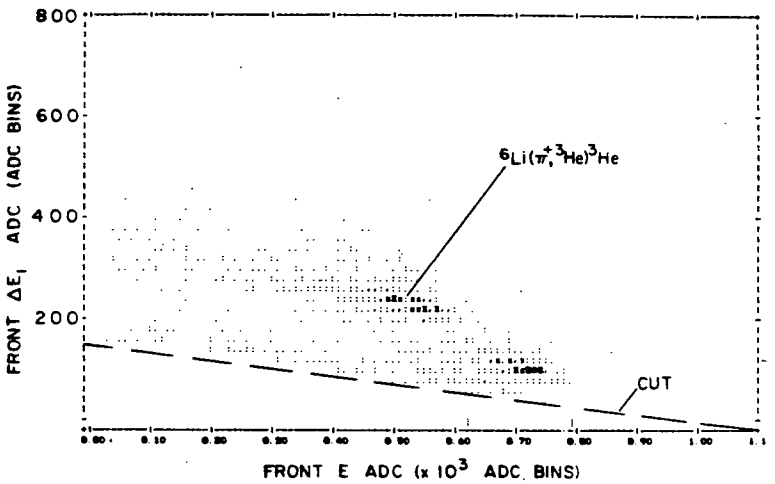

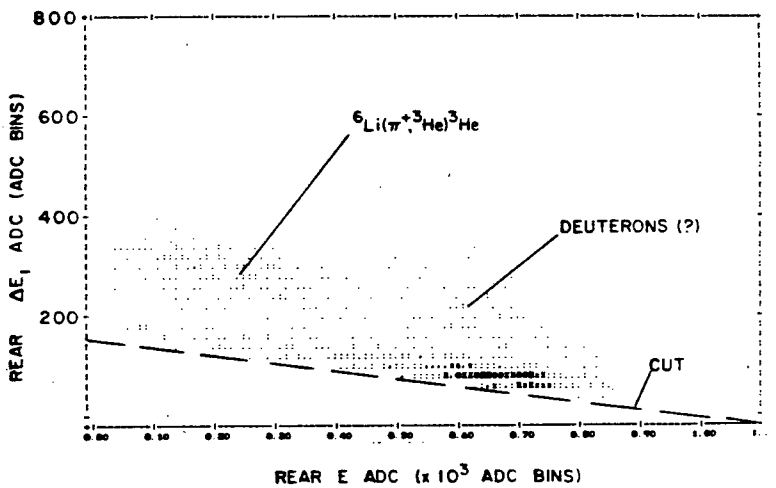

Software cuts have been applied to reject the background events with low ΔE_1 and low E ADC values.

Figure (27)

Rear E vs Front E ADC Cross-Correlation Scatterplot at a Pion Energy of 60 MeV and Front Telescope Lab Angle of 15°

(Same software cuts as in Figure (28))

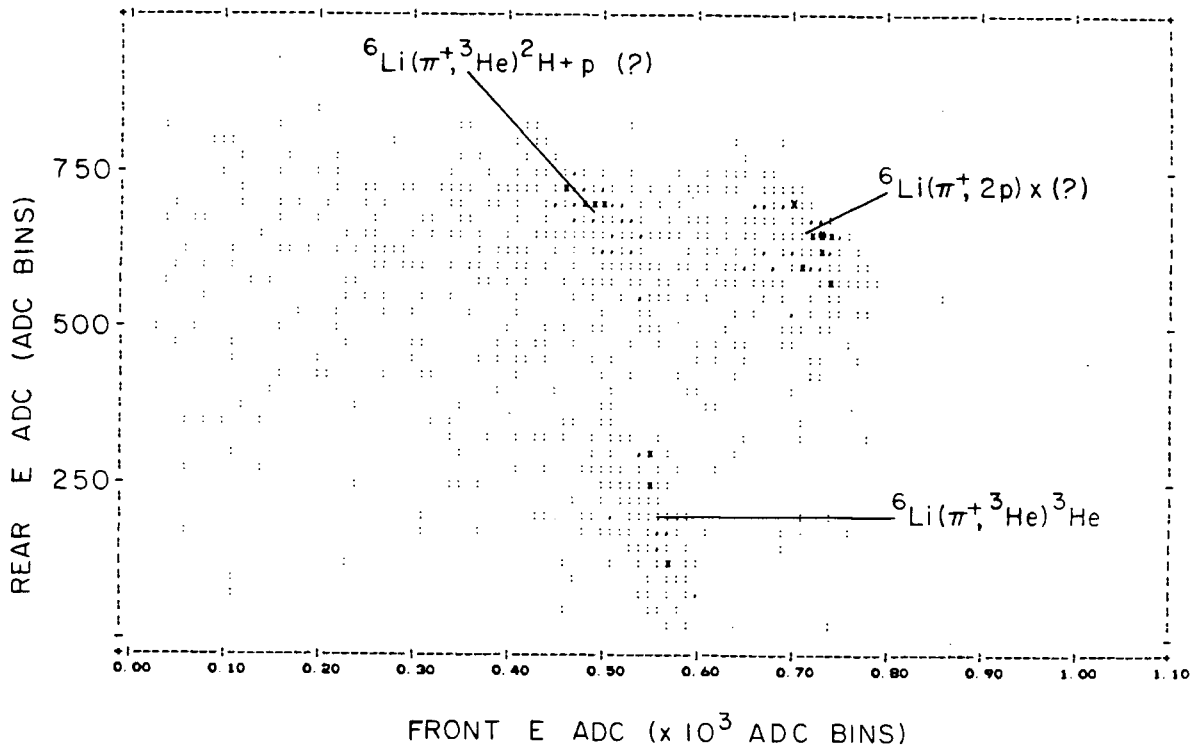

(4.2.6) Systematics of the $^3He(^3He,\pi^+)^6Li$ and $^6Li(\pi^+,^3He)^3He$ Reactions

Originally conceived as a tool for nuclear structure study, proton-induced pion production is now of interest because of the remaining nescience of the reaction mechanism. Theory has been unable to give a suitable microscopic description of coherent pion production and, so, various experimental studies have been executed in an attempt to guide it. Measurements of the doubly coherent $(^3He,\pi)$ reactions at Orsay and Saclay, the precursors to the experiment described in this thesis, are examples of such studies. In another attempt to direct theory, a phenomenological analysis of the available nuclear (p,π) experimental data was begun recently by Couvert [1983, 1984] in the hope of detecting any systematic effects that may reveal common features among the data.

In that (p,π) analysis, effort was made to remove as much as possible the effects of the reaction kinematics. As the exclusive (p,π) reaction is characterized by both a phenomenally high momentum transfer and a cross-section that strongly decreases with target mass, the reaction kinematics could be expected to strongly influence experimental observables such as the differential cross-section. Rather than look at such observables, one may remove the effects of the kinematics by instead examining the Lorentz-invariant matrix element for the reaction. The squared-amplitude of

this matrix element can be extracted from the measured differential cross-section.

The squared-amplitude of this matrix element, Γ^2, for the reaction A(a,b)B is given by [Review of Particle Properties, 1984],

$$\Gamma^2 = (2s_a + 1)(2J_A + 1) \cdot PS \cdot d\sigma/d\Omega^* \qquad (4.6a)$$

where s_a is the spin of particle 'a' and J_A is the nuclear spin of nucleus 'A'. PS is a phase-space factor,

$$PS = (8\pi \sqrt{s} / \hbar c)^2 \cdot (k_a^*/k_b^*) \qquad (4.6b)$$

where $\sqrt{s}$ is the total energy in the center-of-mass and,

$$\hbar c = 197.33 \text{ MeV-fm}$$

Although the (^{3}He,π) and (π,^{3}He) world data base is small, a phenomenological analysis similar to that done for the (p,π) case has been performed for the ^{3}He(^{3}He,π^+)^{6}Li and ^{6}Li(π^+,^{3}He)^{3}He reactions. Following Couvert, the Mandelstam t-variable (the 4-vector momentum-transfer-squared),

Figure (28)

Γ^2 vs t for
the $^6Li(\pi^+, {}^3He)^3He$ Reaction

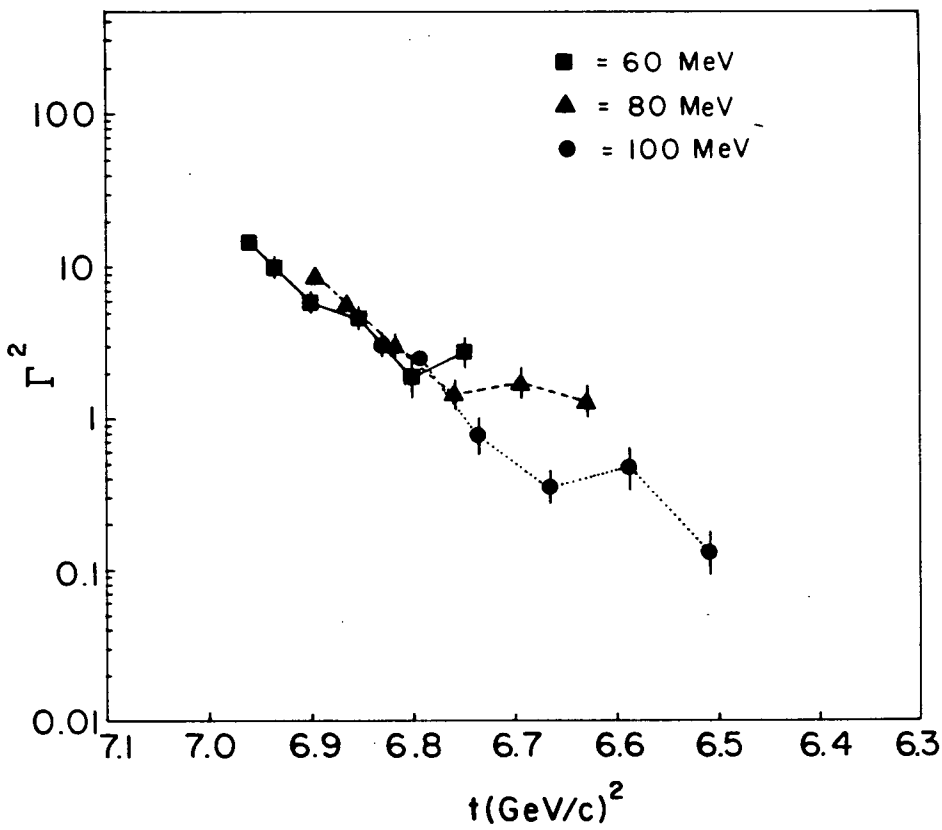

T_π = 60 MeV -> $\sqrt{s}$ = 5.799 GeV

T_π = 80 MeV -> $\sqrt{s}$ = 5.818 GeV

T_π = 100 MeV -> $\sqrt{s}$ = 5.838 GeV

(Extracted from the thesis data)

Lines connecting points of same $\sqrt{s}$
are to guide the eye only.

Figure (29)

Γ^2 vs t for
the $^3He(^3He,\pi^+)^6Li(\nu)$ Reaction
(ν = 1^+, 3^+, 0^+)

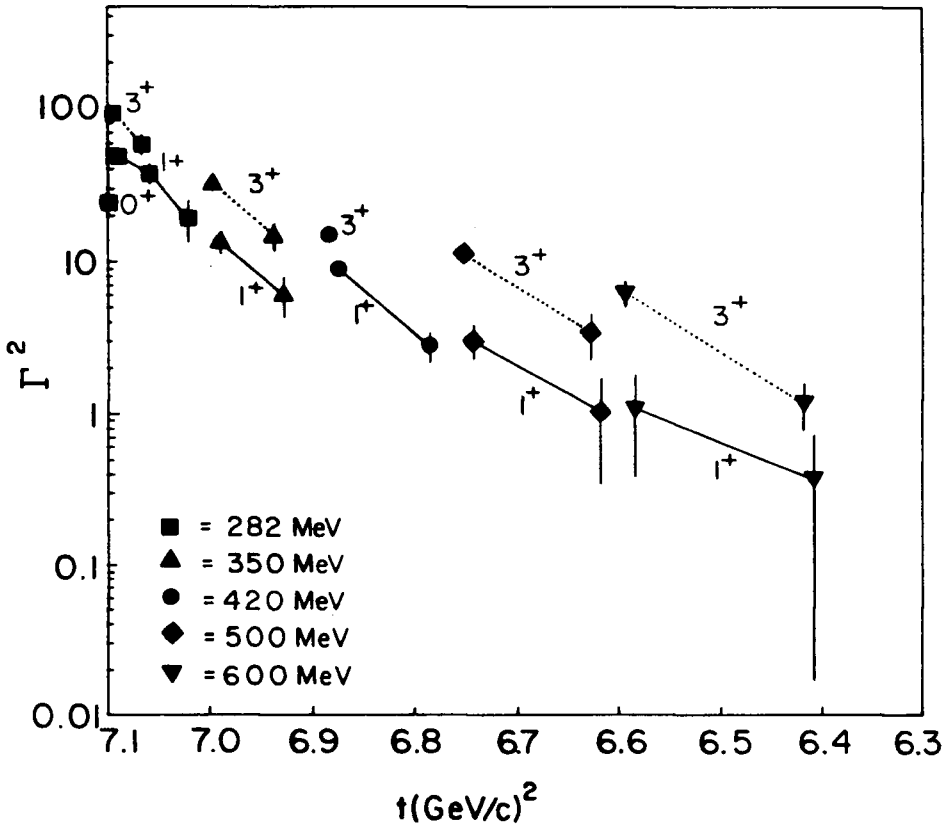

$T_{^3He}$ = 282 MeV -> $\sqrt{s}$ = 5.756 GeV
$T_{^3He}$ = 350 MeV -> $\sqrt{s}$ = 5.764 GeV
$T_{^3He}$ = 420 MeV -> $\sqrt{s}$ = 5.823 GeV
$T_{^3He}$ = 500 MeV -> $\sqrt{s}$ = 5.861 GeV
$T_{^3He}$ = 600 MeV -> $\sqrt{s}$ = 5.909 GeV

(Extracted from data from
LeBornec, et. al., [1981, 1983])

Lines connecting points of same $\sqrt{s}$
and same angular momentum are exponential interpolations.

$$t = (q_a - q_b)^2$$

$$= m_a^2 + m_b^2 - 2E_a E_b + 2p_a p_b \cos\theta^* \qquad (4.7)$$

was chosen for the kinematical observable, where q_i and p_i are the 4- and 3-momenta of particle 'i', respectively, and m_i and E_i are its rest-mass and total energy.

In Figure (28), the Γ^2 extracted from this thesis' data are plotted against t. Γ^2 generally decreases exponentially with t and, between 6.95 and 6.8 $(GeV/c)^2$, appears to exhibit no dependence upon $\sqrt{s}$. However, for t less than 6.8 $(GeV/c)^2$, Γ^2 seems to be lower for a higher value of $\sqrt{s}$. It should be noted, though, that these lower values of t correspond to the center-of-mass angles approaching 90° where the experimental uncertainties are larger.

Couvert has noted that the experimental data from the $^9Be(p,\pi^+)^{10}Be$ reaction at 410 and 605 MeV, and the $^{28}Si(p,\pi^+)^{29}Si$ reaction near threshold, exhibit a dependence upon the spin-states of the exit channels. The ratio of the squared-amplitudes of the matrix element for a final state with total angular momentum J_α, Γ_α^2, to that with total angular momentum J_β, Γ_β^2, was found to agree with the ratio of the total spin projections of the daughter nucleus,

$$\Gamma_{\alpha}^{2}/\Gamma_{\beta}^{2} = (2J_{\alpha}+1)/(2J_{\beta}+1)$$

for the same $\sqrt{s}$ and t. This phenomenological rule was reported not to hold for the data from the $^{6}Li(p,\pi^{+})^{7}Li$ reaction at 600 MeV, an effect that was attributed to the complicated nuclear structure of ^{7}Li (a similar type of spin-state selectivity, albeit for the entrance channels, was studied in an analysis performed by Londergan [1982] comparing the $^{16}O(\pi^{+},p)^{15}O$, $^{16}O(\gamma,n)^{15}O$, $^{16}O(^{3}He,^{4}He)^{15}O$ and $^{16}O(p,d)^{15}O$ reactions). It was noted in Couvert's review that this phenomenological rule had also been observed in high enery (d,p) stripping data. From this unexpected observation, it was decided to see if such a phenomenological scaling was present in the $^{3}He(^{3}He,\pi^{+})^{6}Li(1^{+};3^{+};0^{+})$ data.

In Figure (29), Γ^{2} is plotted against the 4-momentum-transfer-squared for $^{3}He(^{3}He,\pi^{+})^{6}Li(\nu)$, where ν refers to the final state of the ^{6}Li nucleus : the $J^{\pi} = 1^{+}$ ground state or the $J^{\pi} = 3^{+}$ and $J^{\pi} = 0^{+}$ excited states. The data were extracted from Orsay and Saclay measurements taken at five different values of $\sqrt{s}$ [LeBornec, et. al., 1981, 1983]. As in the (p,π) reaction, for a given $\sqrt{s}$ and t the Γ^{2} (and, hence, the differential cross-section) for a state with high angular momentum (e.g., 3^{+}) is larger than that for one with low angular momentum (1^{+} or 0^{+}). This result has two qualitative explainations [Hoistad, 1979; Measday and Miller; 1979]. Because of the high momentum transferred

to the pion, one would expect the ^{6}Li nucleus to be left with a high spin value so as to balance the angular momentum mismatch. Secondly, if the pion were created near the center of the ^{6}Li nucleus (i.e., with a small impact parameter), the angular momentum given to the nucleus would be small. But, such a pion would also have a high probability of being absorbed while travelling to the outside of the nucleus. If, instead, the pion were produced near the nucleus' periphery (with a larger impact parameter), it has a greater chance of escaping the nucleus - but now with the cost of inducing a high spin in the nucleus. These effects will tend to 'filter' out those final states with low angular momenta.

In Figure (30), the ratios of the matrix elements' squared-amplitudes, for different center-of-mass energies $\sqrt{s}$, are plotted against t. These ratios were obtained from the data in Figure (29) using an exponential interpolation between points of the same $\sqrt{s}$ and angular momentum, but with different values of t. The ratio of the number of spin projections of the 0^+ excited state to that of the 1^+ ground state is 1/3, and that for the 3^+ excited state to the ground state is 7/3.

For 7.1 $(\mathrm{GeV/c})^2 > t > 6.9$ $(\mathrm{GeV/c})^2$, the experimental uncertainties are relatively small and the ratios $\Gamma_3{}^2/\Gamma_1{}^2$ and $\Gamma_0{}^2/\Gamma_1{}^2$ are consistent with the ratios of the number of spin projections (7/3 and 1/3, respectively). For 6.8 $(\mathrm{GeV/c})^2 > t$, the uncertainties balloon - although the error bars of the $\Gamma_3{}^2/\Gamma_1{}^2$ ratios tend to encompass the 7/3 value.

That this phenomenon appears in both the (^{3}He,π^+) and (p,π^+) data would perhaps seem to suggest a common feature between these two processes. It is not at all clear, at this point, if this agreement is due to the underlying reaction mechanism, or (since Couvert has noted that this feature is also observed in (d,p) stripping reactions) if it is symptomatic of a high momentum transfer.

To summarize the results of this phenomenological analysis :

(1) The ^{3}He(^{3}He,π^+)^{6}Li(ν) reaction, like the 'simpler' (p,π) reaction, tends to leave the final nucleus (^{6}Li) in a high spin-state. Quantitative explanations of this phenomena in the (p,π) case are applicable to this reaction.

(2) From the available ^{3}He(^{3}He,π^+)^{6}Li(ν) data, it was found that the squared-amplitude of the Lorentz-invariant matrix element for a given final state of ^{6}Li is related to that of another final state by the ratio of the numbers of spin projections for each state. This phenomena can be confidently said to have been observed for 4-momentum-transfer-squared values greater than 6.9 (GeV/c)^2. Below this value, the experimental uncertainties are large, although, the results are still consistent with this observation.

(3) The squared-amplitude of the invariant matrix

element for the $^{6}Li(\pi^{+},{}^{3}He){}^{3}He$ and $^{3}He({}^{3}He,\pi^{+}){}^{6}Li$ reactions decreases with increasing t, but it is difficult to say if there is also a dependence upon $\sqrt{s}$.

Figure (30)

Ratios of Γ^2 vs t
for the $^3He(^3He,\pi^+)^6Li$ Reaction

(Same symbols as in Figure (29))

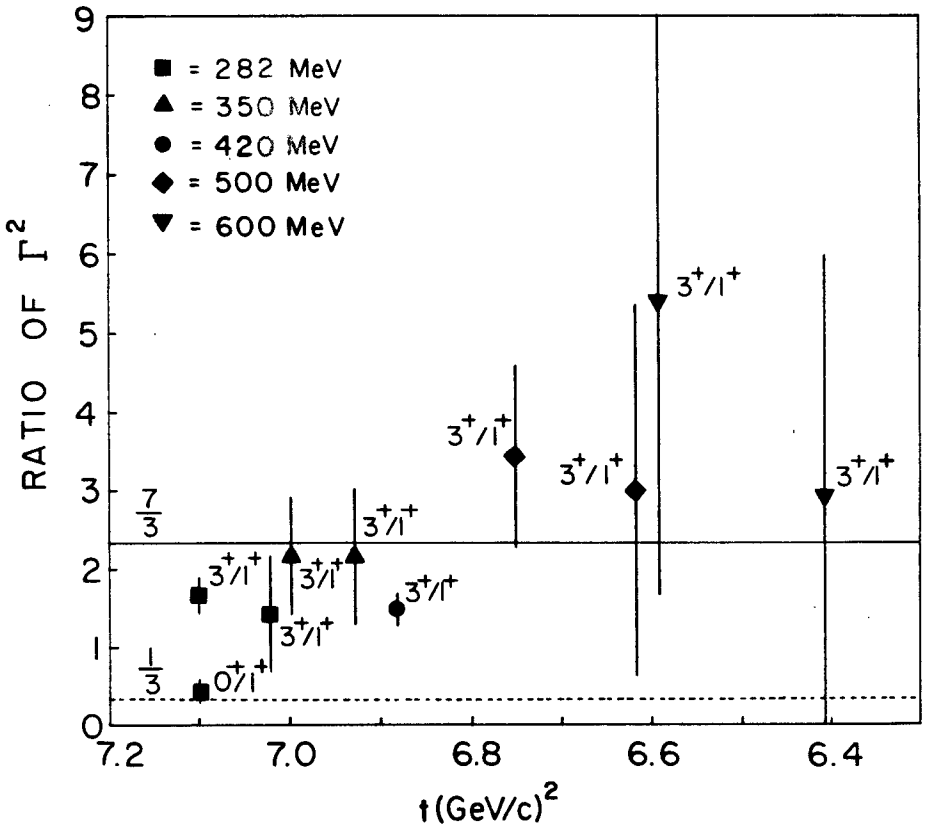

The ratios are calculated from the data of Figure (29) where an exponential interpolation is used between two points of different t, but same $\sqrt{s}$ and final angular momentum value.

5 SUMMARY AND CONCLUSIONS

Coherent pion production from nuclei has been studied predominantly with proton beams. In recent years, the use of deuteron and ^{3}He beams have also enabled the field of doubly coherent pion production, or 'pionic fusion', to be explored.

Experimental measurements of doubly coherent pion production have been primarily with ^{3}He beams incident on light nuclear targets, such as ^{3}He and ^{4}He, and at beam energies between threshold and 282 MeV. Experiments with heavier targets and higher beam energies have suffered from a rapidly dropping differential cross section which strongly suggests that the higher energy region can be more conveniently examined in the time-reversed direction of 'pionic fission'. Not only are these cross sections larger due to phase space, but higher center-of-mass energies can be achieved for relatively lower beam energies.

The most extensively studied $(^3\mathrm{He},\pi^+)/(\pi^+,^3\mathrm{He})$ reaction is $^3\mathrm{He}(^3\mathrm{He},\pi^+)^6\mathrm{Li(g.s.)}$ which, prior to this thesis, had a world data base consisting of a mere twelve data points at ^{3}He energies between 268.5 and 600 MeV and five data points for the $^6\mathrm{Li}(\pi^+,^3\mathrm{He})^3\mathrm{He}$ channel at equivalent ^{3}He energies between 329 and 431 MeV. These scant data were characterized by a lack of detailed and systematic measurements of the reaction's angular dependence.

Two models, the Erlangen-Bonn and Germond-Wilkin, have

been developed to theoretically describe doubly coherent ($^3He,\pi^+$) reactions. Different predictions for the case of $^3He(^3He,\pi^+)^6Li$ are yielded by these models. However, the exiguous data had made it difficult to conclude the usefulness of either model in their applications to this reaction. The main intention of this thesis was to expand the data base of the $^3He(^3He,\pi^+)^6Li$(g.s.) and $^6Li(\pi^+,^3He)^3He$ reactions in the energy region above 350 MeV ^3He beam energies (or 50 MeV pion beam energies) where little data had previously existed. It was also hoped that the provision of good quality data from this reaction would allow a decision to be made upon the validity of the two theoretical models. To that end, this thesis has documented the first measurements of the angular distributions of the $^6Li(\pi^+,^3He)^3He$ differential cross section at pion energies of 60, 80 and 100 MeV, corresponding to 371, 411 and 451 MeV for the $^3He(^3He,\pi^+)^6Li$(g.s.) reaction. These energies are all well below the free NN -> NNπ threshold. The three angular distributions, and one measured previously at Orsay for $^3He(^3He,\pi^+)^6Li$(g.s.) at an equivalent pion energy of 15.4 MeV, were expanded in Legendre polynomial series which have allowed the energy dependence of the $^6Li(\pi^+,^3He)^3He$ total cross section between 15.4 and 100 MeV to be determined.

In summary, the main results documented in this thesis are :

(1) The $^6Li(\pi^+,^3He)^3He$ differential cross-section at

60, 80 and 100 MeV decreases exponentially with $\cos^2\theta^*$.

(2) The $^6Li(\pi^+,{}^3He)^3He$ total cross section, σ_T, and the center-of-mass differential cross-section at a fixed center-of-mass angle were found to exhibit an exponential dependence upon pion energy. For the differential cross-section, the slope of this dependence was found to decrease with increasing angle.

(3) The fitting of the data to a Legendre polynomial series has displayed the growing importance of higher-order partial-waves with increasing pion beam energy.

(4) The squared-amplitudes of the Lorentz-invariant matrix element extracted from this data decrease exponentially with decreasing 4-momentum-transfer-squared. It is not possible to conclude if there is also a dependence upon the total energy in the center-of-mass.

(5) A phenomenological analysis of the $^3He(^3He,\pi^+)^6Li(\nu)$ data from Saclay and Orsay has indicated that there is a final spin-state selectivity in the reaction which is the same as that observed previously in proton-induced exclusive pion production.

(6) There is some evidence to suggest that the $^6Li(\pi^+,{}^3He)^2H+p$ channel was observed as a background component to the $^6Li(\pi^+,{}^3He)^3He$ reaction. Unfortunately, the apparatus design and set-up did not allow any extraction of the relative ^3He-^2H yields from this former fission mode.

The modes used by this thesis to compare the two theories with the data were the angular dependence at 60, 80 and 100 MeV and the energy dependence between 15.4 MeV and 100 MeV at fixed center-of-mass angles. The results of these comparisons can be summarized as follows :

(1) The most obvious theoretical success is that of the Erlangen-Bonn model reproducing the measured angular distribution at 60, 80 and 100 MeV with a fair quantitative agreement.

(2) Although the Germond-Wilkin calculation incorporating the Woods-Saxon representation of the ^6Li nuclear wavefunction does not predict the exponential dependence of $d\sigma/d\Omega^*$ upon $\cos^2\theta^*$ observed, it does reasonably agree with the data for $\cos^2\theta^* > 0.75$. The Germond-Wilkin calculation using the harmonic-oscillator form for the ^6Li nuclear wavefunction underestimates the data over most of the range of $\cos^2\theta^*$. For $\cos^2\theta^* < 0.1$, however, this calculation is of the same order of magnitude

as the data.

(3) The $d\sigma/d\Omega^*$ energy dependence for $^6Li(\pi^+,{}^3He)^3He$, at least for the forward angles, is better described by the Germond-Wilkin Woods-Saxon model than by its harmonic-oscillator form or by the Erlangen-Bonn calculation. At $\theta^* = 90^\circ$, none of the calculations reproduce the measured energy dependence.

(4) In the Erlangen-Bonn model, the presence of the Δ_{33} resonance within the nucleus is manifested by a broad peak in the $^6Li(\pi^+,{}^3He)^3He$ differential cross section at pion energies of about 50 MeV. There is no experimental evidence from the measurements provided by this thesis or from those obtained elsewhere to suggest that such a peak actually exists.

It would also be worthwhile at this point to list some further studies that can be recommended on the basis of the results from this thesis.

(1) $^{6}Li(\pi^{+},{}^{3}He)^{3}He$ for 15 MeV < T_{π} < 60 MeV :

Figures (22)-(25) make obvious the need for $^{6}Li(\pi^{+},{}^{3}He)^{3}He$ (or $^{3}He(^{3}He,\pi^{+})^{6}Li(g.s.)$) data in this energy range. Angular distributions of the $^{6}Li(\pi^{+},{}^{3}He)^{3}He$ reaction should be measured at at least two pion energies between 15 and 60 MeV. This could be performed using the same apparatus (modified to account for the lower energy ^{3}He nuclei) on the M13 low-energy pion channel at TRIUMF. Such a measurement would also prove conclusively whether or not there is a 'hump' in the data at T_{π} = 50 MeV as predicted by the Erlangen-Bonn calculation.

(2) $^{7}Li(\pi^{+},{}^{3}He)^{4}He$ for 15 MeV < T_{π} < 100 MeV :

Barnes, et. al. [1983], have measured this reaction at 39 and 59.3 MeV and there is some data, obtained at Orsay, for the inverse reaction at an equivalent pion energy of about 15 MeV. As the apparatus used for this thesis' experiment can also be used to measure this reaction (with essentially no modifications required), it would be almost incumbent to provide data for the reaction between 15 and 100 MeV pion beam energies.

(3) Three-Body Final States Resulting from π^+ Absorption on ^{6}Li and ^{7}Li :

As discussed in Subsection (4.2.5), Barnes, et. al., [1983], have provided data on ^{7}Li(π^+,^{3}He)^{3}He+n and ^{7}Li(π^+,^{3}He)^{3}H+p for a pion energy on 59.3 MeV. Additionally, Sennhauser, et. al. [1982], have provided multi-body final state data for π^- absorption on ^{6}Li and ^{7}Li. Three-body final states should be measured for π^+ energies in the range of 15 to 100 MeV in order to complement, and improve upon, that data. Such reactions could, in principle, be detected using the same apparatus as used in this thesis' experiment. Unfortunately, the resolution of NE-102 plastic scintillator would make p-d-t-^{3}He-^{4}He discrimination difficult. Hence, one should either obtain a more thorough quantitative understanding of NE-102 scintillator non-linearities than that described in Appendix A, or else the apparatus should be redesigned using, e.g., NaI(Tl) scintillator or semiconductor detectors.

(4) Pionic Fission With Heavier Targets :

Several experiments performed with ^{2}H and ^{3}He beams incident on targets such as ^{6}Li, ^{7}Li, ^{9}Be, ^{10}B and ^{12}C have been described in Chapter 1. It would also be of interest to extend this work by looking at the time-reversed cases of the pionic fission of nuclei with values of A between 8 and

16. Such an experiment should not be restricted solely to two-body final states. This class of experiment would also be technically challenging requiring high-resolution semiconductor detectors, very thin targets and a vacuum scattering chamber.

REFERENCES

Altman, A., et. al., Phys. Rev. Lett. 44:1033 (1983)

Amann, J.F., et. al., Phys. Rev. Lett. 40:758 (1978)

Arthur, E.D., et. al., Phys. Rev. 11:332 (1975)

Aslanides, E., et. al., Phys. Rev. Lett. 43:1466 (1979) {errata - 45:1738 (1980)}

Aslanides, E., et. al., Phys. Lett. 108B:91 (1982)

Aslanides, E., et. al., Nucl. Phys. A 393:314 (1983)

Barnes, P.D., et. al., Nucl. Phys. A 402:397 (1983)

Bent, R.D., ed., 'Pion Production and Absorption in Nuclei - 1981', (AIP Conference Proceedings 79), 1982

Bimbot, L., et. al., Phys. Lett. 114B:311 (1982)

Bimbot, L., et. al., Phys. Rev. C 30:739 (1984)

Birks, J.B., The Theory and Practice of Scintillation Counting, (Pergamon Press : London), 1964

Bressani, A., et. al., Phys. Rev. C 30:1745 (1984)

Butler, G.W., et. al., Phys. Rev. C 26:1737 (1982)

Carchon, R., et. al., Nucl. Instr. and Meth. 128:195 (1975)

Cohen, R.C., et. al., Phys. Lett. 14:242 (1965)

Coulson, L.V., et. al., Nucl. Instr. and Meth. 101:247 (1972)

Couvert, P., in 'Studying Nuclei with Medium Energy Protons', (TRIUMF Report TRI-83-3), 287, 1983

Couvert, P., TRIUMF Preprint TRI-PP-84-46 (1984)

Craddock, M.K., Erdman, K.L. and Sample, J.T., Nature 270:671 (1977)

Craun, R.L. and Smith, D.L., Nucl. Instr. and Meth. 80:239 (1970)

Daehnick, W.W. and Fowler, J.M., Phys. Rev. 11:1309 (1958)

Donnelly, T.W. and Walker, G.E., Phys. Rev. Lett. 22:1121 (1969)

Dropesky, B.J., et. al., Phys. Rev. C 20:1844 (1979)

Eggerman, J., et. al., Z. Physik A 273:381 (1975)

Eisenberg, J.M. and Koltun, D.S., Theory of Meson Interactions with Nuclei, (New York : Wiley), 1980

Evans, H.C. and Bellamy, E.H., Proc. Phys. Soc. 74:1483 (1959)

Fearing, H.W., Prog. Part. Nucl. Phys. 7:113 (1981)

Gardner, E. and Lattes, C.M.G., Phys. Rev. Lett. 74:1236A (1948)

Germond, J.-F. and Wilkin, C., Phys. Lett. 106B:449 (1981)

Germond, J.-F. and Wilkin, C., in 'Pion Production and Absorption in Nuclei - 1981', (AIP Proceedings 79), 411, 1982a

Germond, J.-F. and Wilkin, C., Helv. Phys. Acta. 55:248 (1982b)

Germond, J.-F. and Wilkin, C., J. Phys. G 10:745 (1984)

Gooding, T.J. and Pugh, H.G., Nucl. Instr. and Meth. 7:189 (1960) {errata - 11:365 (1961)}

Goulding, F.S. and Harvey, B.G., Ann. Rev. Nucl. Sci. 25:167 (1975)

Groom, D.E. and Hauser, M.G., Nucl. Instr. and Meth. 46:301 (1967)

Helene, O., Nucl. Instr. and Meth. in Phys. Res. 228:120 (1984)

Hibou, F., 'Production de pions dans des collisions noyau-noyau aux energies intermediaires'; Centre de Recherches Nucleaires de Strasbourg, CRN-PN 83/10, 1983

Hoistad, B., Adv. Nucl. Phys. 11:135 (1979)

Huber, G.M., et. al., Nucl. Instr. and Meth. in Phys. Res. 227:54 (1984)

Huber, M.G. and Klingenbeck, K., in 'Pion Production and Absorption in Nuclei - 1981', (AIP Proceedings 79), 389, 1982

Huber, M.G., Klingenbeck, K. and Hupke, R., Nucl. Phys. A 396:191c (1983)

Hupke, R., et. al., Contribution I50 to the Particle Particles and Nuclei International Conference X, Heidelberg, 1984

Jones, G., in 'Pion Production and Absorption in Nuclei - 1981', (AIP Proceedings 79), 15, 1982

Kisslinger, L.S. and Wang, W., Ann. Phys. 99:374 (1976)

Klingenbeck, K., in 'From Collective States to Quarks in Nuclei', Lecture Notes in Physics 137 (eds. A. Ahrenovel and A.M. Saruis), Springer, Berlin, 102 (1981)

Klingenbeck, K., Dillig, M. and Huber, M., Phys. Rev. Lett. 47:1654 (1981)

LeBornec, Y., et. al., Phys. Rev. Lett. 47:1870 (1981)

LeBornec, Y., et. al., Phys. Lett. 133B:149 (1983)

Lolos, G.J., et. al., Phys. Lett. 126B:20 (1983)

Londergan, J., in 'Pion Production and Absorption in Nuclei - 1981', (AIP Proceedings 79), 215, 1982

McKeown, R.D., et. al., Phys. Rev. Lett. 44:1033 (1980)

McParland, B.J., et. al., Phys. Lett. 156B:47 (1985)

Marmier, P. and Sheldon, E., Physics of Nuclei and Particles (New York : Academic Press), 1970

Measday, D.F. and Schneider, R.J., Nucl. Instr. and Meth. 42:26 (1966)

Measday, D.F. and Miller, G.A., Ann. Rev. Nucl. Part. Sci. 29:121 (1979)

Miles, T. and Satanove, A., IEEE Trans. Nucl. Sci. NS-30:3746 (1983)

Millburn, G.P., et. al., Phys. Rev. 95:1268 (1954)

Minehart, R.C., et. al., Phys. Rev. 177:1455 (1969)

Nagamiya, S. and Gyulassy, M.,
Adv. Nucl. Part. Phys. 13:201 (1984)

Niskanen, J.A., Proc. 5th Intl. Symp. on Polarization
Phenomena in Nuclear Physics (Santa Fe), 77, 1980

Ohlsen, G.G., Rep. Progr. Phys. 35:717 (1972)

Prescott, J.R. and Rupaal, A.S., Can. J. Phys. 39:221 (1961)

Rasmussen, J.O., in 'Short Distance Phenomena
in Nuclear Physics', D.H. Boal and
R.M. Woloshyn, eds., (New York:Plenum Press), 275, 1983

Ramsberg, L.P., Ann. Rev. Nucl. Sci. 17:347 (1967)

Redwine, R.P., Nucl. Phys. A 434:239c (1985)

Review of Particle Properties, Rev. Mod. Phys. 56,
No.2, Part II, 1984

Rossi, B., High Energy Particles, (Prentice-Hall,
New York), 1952

Schiffer, J., Comm. Nucl. Part. Phys. 10:243 (1981)

Schiffer, J., Comm. Nucl. Part. Phys. 14:15 (1985)

Segre, E., Nuclei and Particles,
(Benjamin/Cummings : Reading) 1977

Sennhauser, U., et. al., Nucl. Phys. A 368:429 (1982)

Shyam, R. and Knoll, J., Phys. Lett. 136B:221 (1984)

Stetz, A.W., Univ. of Alberta Internal Report 81 (1975)

Stinson, G.M., 'Design Configuration of the
M11 Channel at TRIUMF', TRIUMF Design-Note
TRI-DNA-80-5, 1980

Walden, P., private communication (1985)

Wall, N.S., et. al., Nucl. Phys. A 268:459 (1976)

Willis, N., et. al., Phys. Lett. 136B:334 (1984)

Wright, G.T., Phys. Rev. 91:182 (1953)

Yang, M.J., et. al., Nucl. Instr. and Meth. 185:115 (1981)

APPENDIX A

The Response of NE-102 Plastic Scintillator to Protons and ^{3}He Nuclei

The light response of plastic scintillator to a charged particle is reduced if the incident particle is densely ionizing. This quenching effect for heavily-ionizing radiations may be attributed to the interactions between adjacent sites of molecular excitations and ionizations that lead to a non-radiative dissipation of the deposited energy [Birks, 1964]. As this non-linear response could make identifying the ^{3}He events resulting from the ^{6}Li(π^+,^{3}He)^{3}He reaction with plastic scintillator counters difficult, a quantitative measure of this effect was necessary for the analysis. A parameterization of the light response of NE-102 scintillator and its application to identifying the ^{6}Li(π^+,^{3}He)^{3}He events are discussed in this Appendix.

By assuming the above quenching mechanisms, Wright [1953] derived the differential light output per path length 'dx' of an organic scintillator as a function of the stopping power,

$$dL/dx = \lambda \cdot \ln(1 + a \cdot dE/dx) \qquad \text{(A.1a)}$$

where λ and 'a' are constants for the scintillator. Some authors have used the more commonly seen parameterization,

$$dL/dx = S\cdot(dE/dx) \;/\; (1 + kB\cdot dE/dx) \qquad (A.1b)$$

where 'S' is the scintillation efficiency and 'kB' is a measure of the response non-linearity induced by a heavily-ionizing particle. 'k' is the probability that quenching rather than fluorescence will occur and B·(dE/dx) is the number of damaged molecules per undamaged molecule [Prescott and Rupaal, 1961]. For a small dE/dx value, equation (A.1a) is approximated by equation (A.1b), where,

$$kB = a \;/\; 2$$

Although the parameters in equation (A.1a) are more difficult to assign physical interpretations to, this equation is particularly amenable to numerical calculation. λ can be defined as an arbitrary normalization constant and 'a' can then be found from best fits to measured data. However, a review of the relevant literature showed that there is a fairly broad selection of values of 'a' to choose from. Craun and Smith [1969] have tabulated values of kB(= a/2) for NE-102 that were published between 1958 and 1967. Except for one measurment with a deuteron beam, 'a' was determined by measuring the response of NE-102 scintillator only to protons. For example, Gooding and Pugh [1960] presented a calculation of the scintillation response to stopping protons, deuterons, tritons and alphas. That calculation used a = 23.6(±2) $mg\cdot cm^{-2}\cdot MeV^{-1}$, on the basis of

measurements using low-energy protons (< 14 MeV) by Evans and Bellamy [1959]. For 120 MeV protons and deuterons, Gooding and Pugh measured a = 26.5(±5) $mg \cdot cm^{-2} \cdot MeV^{-1}$ which, to within experimental error, agreed with the value derived from the low-energy proton data. These two values were also in fair agreement with all but two of the other measurements. Daehnick and Fowler [1958] determined 'a' to be as low as 4 $mg \cdot cm^{-2} \cdot MeV^{-1}$ and Groom and Hauser [1967] measured 'a' to be in the range of 7 to 15 $mg \cdot cm^{-2} \cdot MeV^{-1}$. Despite these two rather extreme results, Gooding's and Pugh's selection for 'a' was used in the calculation described by this Appendix.

The light output for a charged particle traversing R $gm \cdot cm^{-2}$ of scintillator was determined by integrating equation (A.1a),

$$\Delta L = \lambda \int_0^R \ln(1 + a \cdot (dE/dx))\, dx \qquad (A.2)$$

A code was developed which numerically integrated equation (A.2) (using a finite summation) over 50μ steps. This step-size was an optimal value that gave an accurate result for a reasonable expenditure of computer time. dE/dx was calculated directly from the Bethe-Bloch equation for carbon and hydrogen, and then Bragg's additivity rule [Review of Particle Properties, 1984] was used to determine the energy loss in NE-102 (CH_{1104}), as described in the Appendix B. As a test of this code, Gooding's and Pugh's

original calculations (which had used a power-law approximation for dE/dx for protons, deuterons, tritons and alphas stopping in NE-102) were repeated with excellent agreement.

Figure (A.1) shows the scintillation light output calculated by this code for protons and ^{3}He nuclei stopping in NE-102 scintillator. In this case, R in equation (A.2) is the range of the bombarding particle. The arbitrary normalization from Gooding's and Pugh's paper of a unity light output for a stopped 160 MeV proton was also used here. The data are the measured ^{3}He responses which are given by,

$$L_{^3He} = L_P \cdot (ADC_{^3He} / ADC_P) \qquad (A.3)$$

where L_P is the calculated light response for the stopped $\pi^+d \rightarrow 2p$ calibration proton and ADC_i is the measured mean of the ADC response for particle 'i'. Non-linearities and a non-zero offset in the ADC response were neglected. The deposited energies of the ^{3}He nuclei were estimated from the Monte Carlo code described in Appendix B. This Monte Carlo code was also modified for the $\pi^+d \rightarrow 2p$ calibration reaction and used to calculate the deposited proton energies, from which L_P was calculated by solving equation (A.2) for protons.

The errors shown in Figure (A.1) are only those due to

the uncertainty in the estimation of the proton and ^{3}He ADC means. The sample standard deviations were of the order of two to three times the uncertainties shown. In general, there is a fair agreement between the data and the calculation for deposited energies below 80 MeV. Above this point, the relative scintillation output measured is significantly less than that calculated.

This observation could perhaps be interpreted as an increased quenching effect at higher deposited energies (i.e., 'a' increases with deposited energy). As the value of 'a' used for calculating the light response was determined from low-energy proton data, it is possible that there is an energy and/or particle dependence. This disagreement would be best examined using a calibrated ^{3}He beam. Despite this discrepancy at the higher ^{3}He energies, equations (A.2) and (A.3) were useful in estimating the ADC response of the ^{3}He's from the ^{6}Li(π^+,^{3}He)^{3}He reaction.

The relative light outputs in NE-102 for protons and ^{3}He nuclei are plotted against incident energy for a stopping counter in Figure (A.2) and for a 1 mm thick transmission counter in Figure (A.3). The range of the ^{3}He and calibration proton energies studied in this experiment (as discussed in Subsection (3.5.1)) are also shown.

Figure (A.1)

Response of Protons and ^{3}He Nuclei Stopping in NE-102 Plastic Scintillator

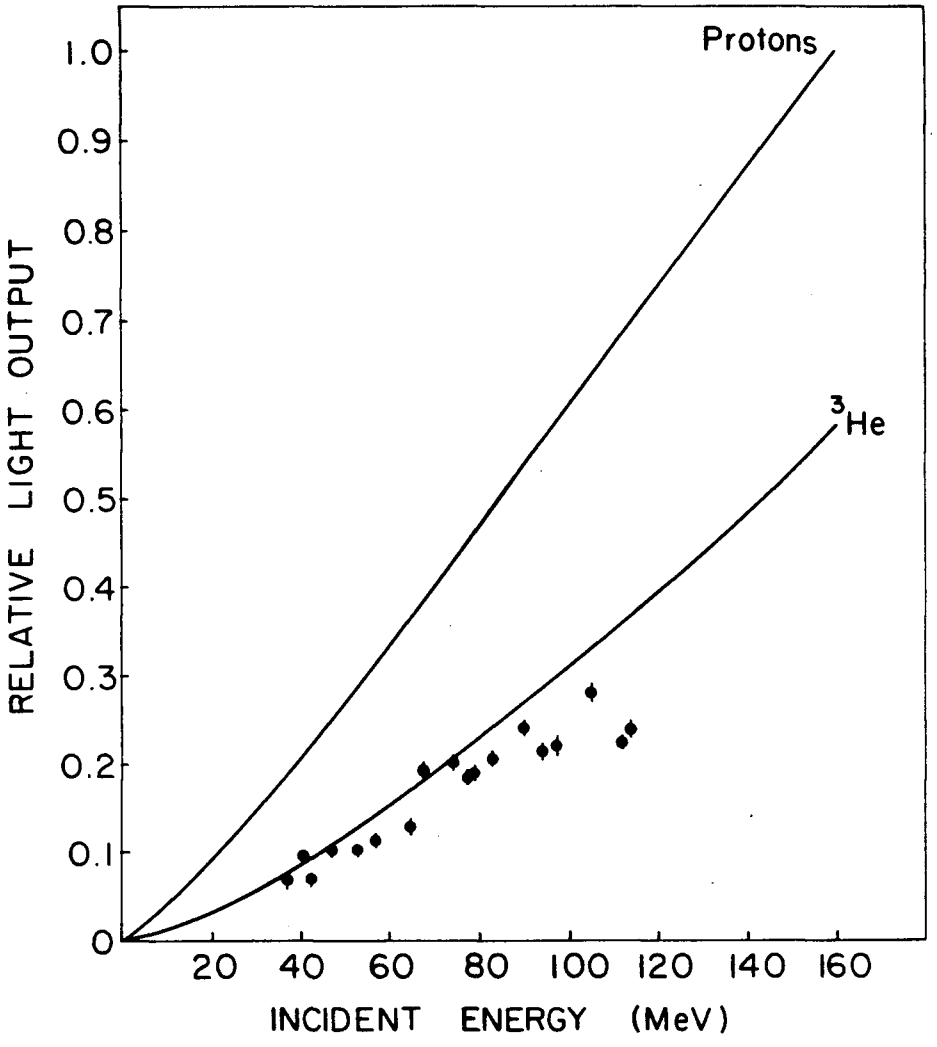

The curves are calculated from equations (A.2) and (A.3) using a = 23.6 mg·cm^{-2}MeV^{-1}. Measured points are for ^{3}He nuclei from the ^{6}Li(π^+,^{3}He)^{3}He reaction. Error bars shown represent only the uncertainties due to estimating the mean of the ADC responses (see discussion in text).

Figure (A.2)

Relative Light Response of Protons and ^{3}He Nuclei Stopping in NE-102 Plastic Scintillator

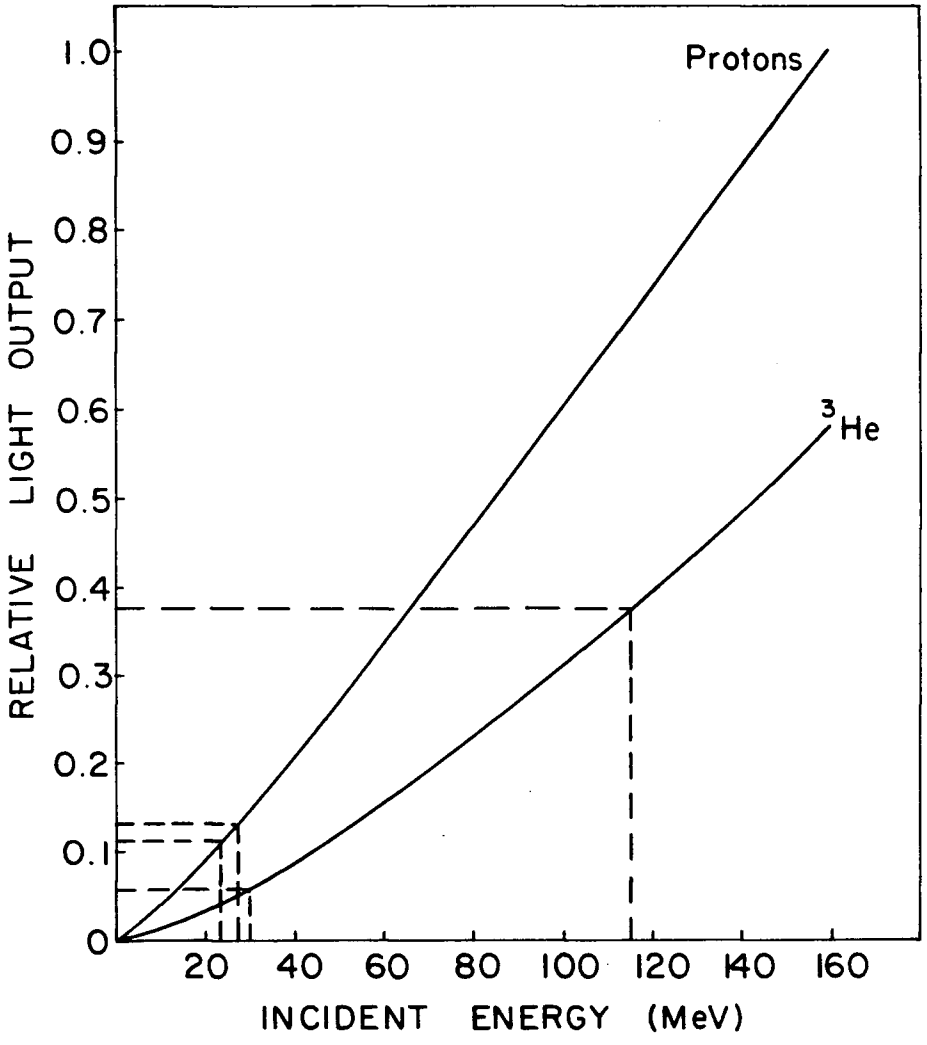

The energy range shown for the protons corresponds to that of the $\pi^+ d \rightarrow 2p$ calibration; that for the ^{3}He's corresponds to the range calculated by the Monte Carlo code for the $^6Li(\pi^+, {}^3He)^3He$ reaction.

Figure (A.3)

Relative Light Response of Protons and ^{3}He Nuclei Passing Through a 1 mm Thick NE-102 Plastic Scintillator Counter

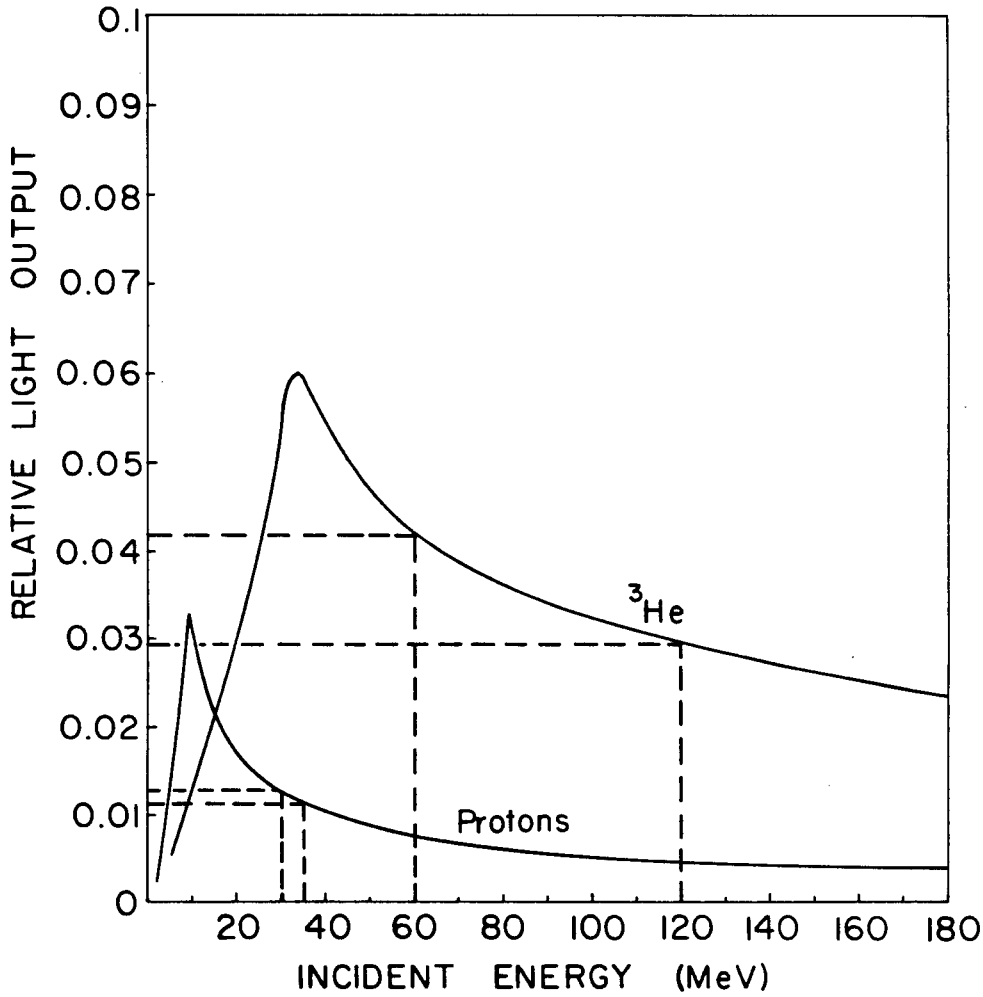

The energy range shown for the protons corresponds to that of the $\pi^+d \rightarrow 2p$ calibration; that for the ^{3}He's corresponds to the range calculated by the Monte Carlo code for the $^6Li(\pi^+,{}^3He)^3He$ reaction.

APPENDIX B

Monte Carlo Estimation of the Effective Lab Solid Angle

A Monte Carlo code was used to estimate the effective solid angle of a conjugate telescope pair in the laboratory reference frame, $\Delta\Omega_{eff}$. The procedure used by this code followed the basic principles described by Carchon, et. al., [1975]. However, the algorithm described in that paper estimated the solid angle for only a single-arm detector system and did not account for any effects introduced by a finite target thickness, the reaction kinematics, the incident beam momentum spread, the energy losses suffered by the particles nor by a detector composed of several counters. These complications are included within the code developed for this two-arm experiment.

The flow-chart for this program is given in Figure (B.1). The procedure followed by the code is to generate a random trajectory, emanating from a random point within the ^{6}Li target and defined by the beam spot, into a solid angle ($\Delta\Omega_0$) surrounding the detector. Those trajectories that intercept both the front and rear detectors, and the corresponding ^{3}He nuclei reaching and stopping within both E counters, define $\Delta\Omega_{eff}$.

Figure (B.1)

Flow-Chart of the Monte Carlo Code
Used to Estimate the Effective Lab Solid Angle

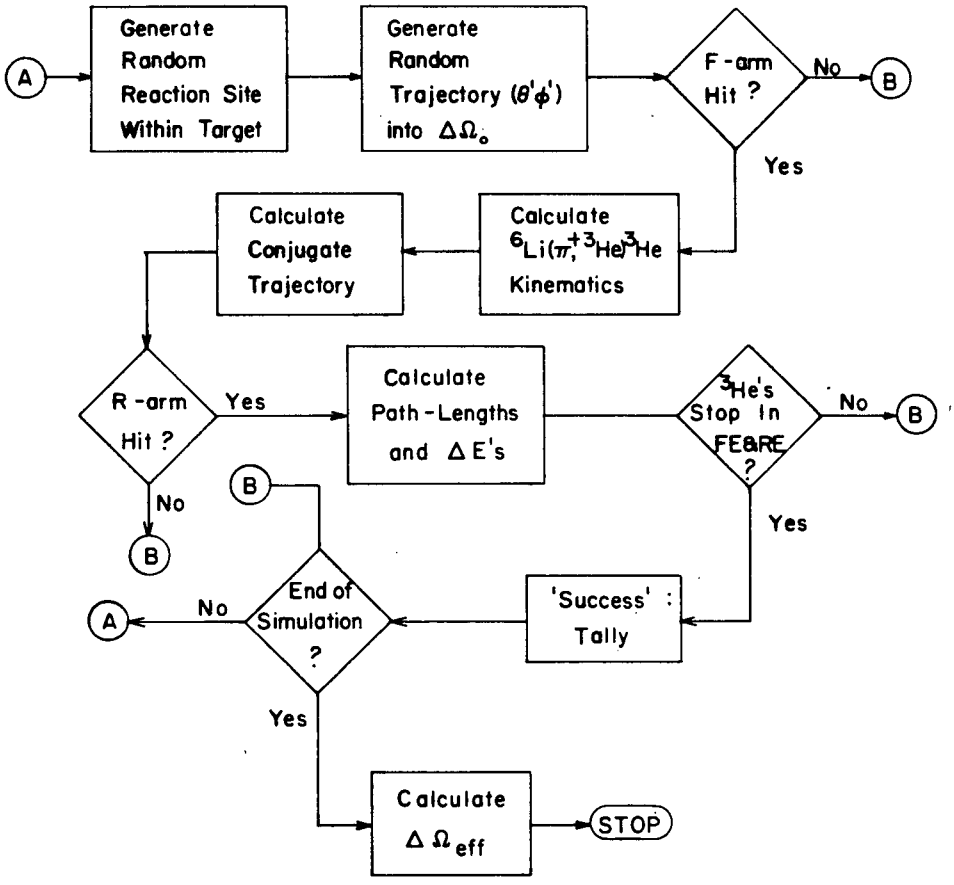

The geometry employed by this simulation is shown in Figure (B.2). The x-axis is coincident with the beam, the z-axis is normal to the scattering plane (defined by the x- and y-axes) and the ^{6}Li target is set at a 45^0 angle to the beam axis. The random point within the target, corresponding to a ^{6}Li(π^+,^{3}He)^{3}He reaction site, is given by the coordinates,

$$x_0 = \sqrt{2} \cdot (1 - 2\xi)t/2 - y_0 \qquad \text{(B.1a)}$$

$$y_0 = r_0 \cos\psi_0 \qquad \text{(B.1b)}$$

$$z_0 = r_0 \sin\psi_0 \qquad \text{(B.1c)}$$

where ξ is a random number uniformly distributed on the unit-interval and 't' is the target thickness (in cm). The $\sqrt{2}$ factor arises from the 45^0 angle of the target to the beam axis. r_0 is the radial distance between the reaction site and the beam axis, and ψ_0 is the azimuthal angle in the yz-plane.

Figure (B.2)

Geometry Used in the Monte Carlo Code

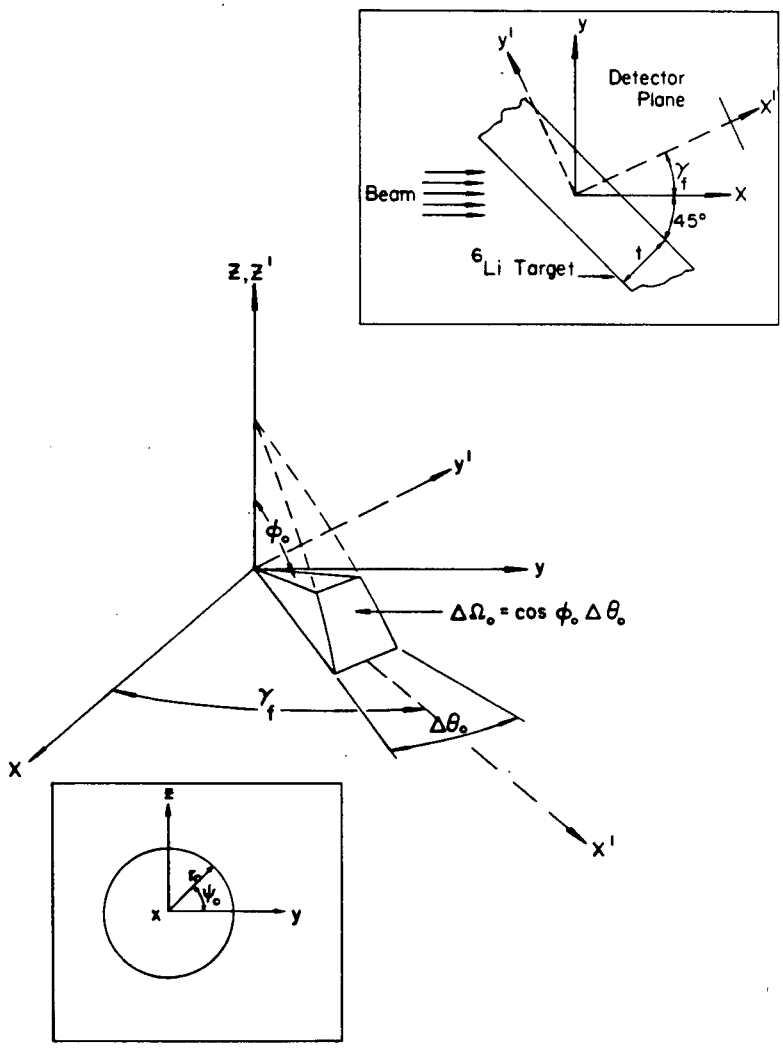

From the measured beam profile (see Section (3.1)), it was recognized that the actual beam spot could be well approximated by a Gaussian and, for the purposes of this Monte Carlo code, the beam spot was taken to have a distribution of the form,

$$\exp(-x^2/c^2)$$

The half-width at 10% of the maximum (x_{10}) was taken to be 1.75 cm, a choice based upon the beam-profile measurements. This gives,

$$c = x_{10} / \sqrt{(\ln(10))}$$

and substituting the numerical values,

$$c = 1.15 \text{ cm}$$

r_0 can then be found by inverting

$$\xi = \exp(-r_0^2/c^2) \qquad \text{(B.2b)}$$

where ξ is a random number uniformly distributed between 0 and 1,

$$r_o = c\sqrt{} / (-\ln(\xi)) \tag{B.2c}$$

ψ_o is assumed to uniformly distributed between 0 and 2π radians, or,

$$\psi_o = 2\pi\xi \tag{B.2d}$$

where, again, ξ is a random number on the unit-interval.

After having being generated, the (x_o, y_o, z_o) coordinates are then rotated about the z-axis to the primed coordinate system where the x'-axis is coincident with the target-detector axis,

$$x_o' = x_o \cdot \cos\gamma_f + y_o \cdot \sin\gamma_f \tag{B.3a}$$

$$y_o' = -x_o \cdot \sin\gamma_f + y_o \cdot \cos\gamma_f \tag{B.3b}$$

$$z_o' = z_o \tag{B.3c}$$

where γ_f is the angle between the beam axis and the target-detector axis.

A random ray is generated with the starting point (x_o', y_o', z_o') into a solid angle $\Delta\Omega_o$ that surrounds the 'upper' half of the forward detector. Only the 'upper' half (i.e., $z' > 0$) need be considered in the simulation due to the symmetry about the scattering plane. $\Delta\Omega_o$ is found by

integrating

$$d\Omega = \sin\phi \, d\phi \, d\theta$$

for ϕ between ϕ_0 and 90° and for θ between $-\Delta\theta_0/2$ and $+\Delta\theta_0/2$,

$$\Delta\Omega_0 = \cos\phi_0 \cdot \Delta\theta_0 \qquad \text{(B.4)}$$

$\Delta\Omega_0$ must be optimized, however. It obviously must not only encompass the front telescope, but it must also not be so large so as to reduce the probability of the random ray intercepting the telescope (and, hence, making the simulation time excessive). The maximum angular width of the front telescope is defined by the face of ΔE_1 counter nearest the ^{6}Li target, and is given by,

$$\Delta\theta = 2 \cdot \tan^{-1}(4.5 \text{ cm} / 50 \text{ cm}) = 10.3^\circ$$

where 4.5 cm is the half-width of the counter and 50 cm is the separation betweeen the counter and the target. Similarly, its maximum angular half-height of the front telescope is,

$$\Delta\phi_{max} = \tan^{-1}(15 \text{ cm} / 50 \text{ cm}) = 16.7^{\circ}$$

$\Delta\Omega_0$ must encompass these dimensions. Hence, the value chosen for $\Delta\theta_0$ was 15° and an angular half-height of 20° was selected. This latter choice yields

$$\phi_0 = 90^{\circ} - 20^{\circ} = 70^{\circ}$$

and, thus,

$$\cos\phi_0 = \cos(70^{\circ}) = 0.342$$

giving,

$$\Delta\Omega_0 = 89.54 \text{ msr}$$

The random ray generated, then, has angles θ' and ϕ' limited to $\pm 7.5^{\circ}$ and between 70° and 90°, respectively. Or,

$$\theta' = (1 - 2\xi)\ \Delta\theta_0/2 \qquad \text{(B.5a)}$$

and, since it is the cosine of ϕ' that is uniformly distributed between 0 and $\cos\phi_0$,

$$\phi' = \cos^{-1}(\xi \cdot \cos\phi_0) \tag{B.5b}$$

where the ξ's are again different random numbers on the unit interval.

The coordinates (y',z') of the point given by the intersection of the ray emanating from (x_0',y_0',z_0') and a plane normal to the x'-axis at a distance λ from the origin measured along the x'-axis is,

$$y' = y_0' + (\lambda - x_0')\cdot\tan\theta' \tag{B.6a}$$

$$z' = z_0' + (\lambda - x_0')\cdot\cot\phi'\cdot\sec\theta' \tag{B.6b}$$

The code calculates the point (y',z') and checks if it lies within the plane defined by the face of the forward E counter furthest away from the target (i.e., the 'exit face'). If so, the ray is claimed to have successfully traversed the detector telescope. In this particular case, λ would be the sum of the target-telescope separation distance (50 cm) and the depth of the exit face (2.74 cm). The thicknesses of the ^{6}Li target, the polyethylene bag and the aluminum wrapping are neglected relative to these two distances. If the ray has successfully traversed the front telescope, θ' is then transformed into the unprimed coordinate system by a rotation of $-\gamma_f$ about the z-axis. As the rotation is about the z-axis, the ϕ and ϕ' angles are, of course, the same. The relativistic kinematics of the

$^6Li(\pi^+,{}^3He)^3He$ reaction are then calculated with the incident pion causing this event having a momentum within the beam momentum bite Δp,

$$p_\pi = p_0 \cdot + (1 - 2\cdot\xi)\Delta p/2 \qquad (B.7)$$

where p_0 is the mean pion momentum. For the experiment described in this thesis, $\Delta p = 0.05\cdot p_0$. In order to reduce the computation time, this narrow momentum distribution was approximated by a uniform distribution, as shown in equation (B.7). The energy loss of the pion travelling through the ^6Li target to the interaction site is assumed to be negligible relative to the energy spread induced by Δp. The center-of-mass angle, θ^*, corresponding to the forward scattering angle is calculated from the kinematics and the forward ^3He's angles. From these, the θ and ϕ angles of the rear ^3He nucleus' trajectory are then calculated. The procedure used in the front arm geometry calculation is then repeated for the rear ray and if this conjugate ^3He successfully traverses the entire rear telescope a 'good geometry' event is defined by the code to have occurred.

For each such event, the path lengths through the ^6Li target, the polyethylene bag, air, scintillation counters and aluminum wrap are then determined. Along each path length, the energy loss is calculated by dividing up the path length into segments and performing a finite summation of the differential energy loss calculated for each segment using the Bethe-Bloch equation,

$$\Delta E = \Sigma\ (dE/dx)\ \Delta x \qquad (B.8)$$

where Δx is the segment thickness. For the polyethylene bag (CH_2), air (80% N_2 and 20% O_2) and scintillator ($CH_{1.104}$), Bragg's additivity rule is used to calculate the compounds' energy losses,

$$(1/\rho)(dE/dx)_{CMPD} = \Sigma\ (1/\rho \cdot dE/dx)_i\ f_i \qquad (B.9)$$

where f_i is the fractional weight of element 'i' in the compound.

The ^3He nucleus is claimed by the code to have stopped when the cumulative ΔE exceeds the incident energy. A 'success' is defined as those 'geometrically good' events which have both the front and rear ^3He's reach, and stop in, the E counters of the telescopes. The effective lab solid angle of the telescope pair is then given by,

$$\Delta\Omega_{eff} = 2\ \epsilon\ \Delta\Omega_0 \qquad (B.10a)$$

where the 'efficiency' of the simulation is the ratio of the number of 'successes' to 'attempts',

$$\epsilon = S\ /\ A \qquad (B.10b)$$

The factor of 2 in equation (B.10a) comes from the fact that the simulation was for only half of the detector. Assuming

binomial statistics, the statistical error in $\Delta\Omega_{eff}$ is estimated by,

$$\sigma_{\Delta\Omega} = \sqrt{(\epsilon(1 - \epsilon)/(A-1))} \cdot (2 \cdot \Delta\Omega_0) \qquad \text{(B.10c)}$$

The effects due to nuclear absorption of the ^{3}He nuclei (discussed in Subsection (3.5.2)) were not included in the Monte Carlo calculation but rather treated as a systematic uncertainty. The maximum percentage of ^{3}He nuclei lost due to absorption in a single telescope is 3% and that for a conjugate telescope pair is the quadratic sum, or 5% (rounded up).

To simplify the code, the energy straggling of the ^{3}He nuclei was also neglected. A calculation of the Landau distribution of the energy loss of a ^{3}He nucleus [Rossi, 1952] (in the energy range studied) traversing a transmission counter showed that the distribution could be well approximated by a Gaussian with a standard deviation ranging between 2% and 5% of the mean energy loss. Consideration of the multiple scattering of the ^{3}He nuclei was also omitted from the Monte Carlo. The justification for this is discussed below.

In Subsection (3.2.1), it was noted that the geometrical solid angle of a conjugate pair is defined by the forward telescope. Because of this, multiple scattering of the ^{3}He nuclei between the ^{6}Li target and the forward telescope will have no effect upon the solid angle (the

number of particles scattered out being exactly compensated by the number scattered in). The omission of multiple scattering can be justified if the rear arm solid angle, $\Delta\Omega_R$, is larger than the solid angle defined by a multiple scattering process, $\Delta\Omega_S$ [Walden, 1985].

$\Delta\Omega_S$ is the solid angle of an angular cone of half-width Θ_0,

$$\Delta\Omega_S = 2\pi\cdot(1 - \cos\Theta_0) \qquad \text{(B.11)}$$

Here, the standard deviation of the Gaussian approximation to the distribution from the Moliere theory is used for Θ_0. The Rossi formula [Review of Particle Properties, 1984] gives an approximation to Θ_0 for a particle traversing an absorber of thickness 'L',

$$\Theta_0 = (14.1/p\beta)\cdot Z_{inc}\cdot f(L,L_R) \qquad \text{(B.12a)}$$

where

$$f(L,L_R) = \sqrt{(L/L_R)}\cdot\{1 + (1/9)\cdot\log_{10}(L/L_R)\} \qquad \text{(B.12b)}$$

and where Θ_0 is in radians, 'p' and β are the incident particle's momentum (in MeV/c) and velocity (normalized to 'c'), respectively. L_R is the absorber's radiation length.

The upper limit of Θ_0 is given by the lowest ^{3}He momentum expected upon exiting the ^{6}Li target in the energy range studied in this experiment (148 MeV/c). This gives,

$$\Theta_0 < 0.5^\circ$$

which, in turn, yields an upper-limit to $\Delta\Omega_S$,

$$\Delta\Omega_S < 0.24 \text{ msr}$$

A measure of the effect of the multiple scattering upon the solid angle calculation is given by the ratio,

$$\Delta\Omega_S^* / \Delta\Omega_R^*$$

where $\Delta\Omega_R^*$ is the rear counter's solid angle in the CMS. As both solid angles are calculated in the lab reference frame, this ratio is,

$$\Delta\Omega_S^* / \Delta\Omega_R^* = (\Delta\Omega_S / \Delta\Omega_R) \cdot (J_F / J_R) \qquad \text{(B.13)}$$

where J_F and J_R are the Jacobians of the solid-angle transformation for the forward and rear ^{3}He nuclei, respectively,

$$J = d\Omega^* / d\Omega$$

It is desirable to have the ratio given by equation (B.13) as small as possible (i.e., the multiple-scattering solid angle much less than the rear detector solid angle). Hence, the worst case will arise for J_R small and J_F large, which occurs at the forward angles. An upper limit for this ratio of solid-angles was calculated using the limits of the quantities in equation (B.13). The extreme values of the Jacobians occur at T_π = 100 MeV and at a front telescope lab angle of 15^0,

$$J_F = 1.252$$

$$J_R = 0.782$$

The geometric solid angle of the rear telescope in the lab can be estimated using the approximation,

$$\Delta\Omega_R = A/r^2 = (8 \times 30) / (37.74)^2 = 169 \text{ msr}$$

where (8 x 30) cm^2 is the area of the E counter and 37.74 cm is the distance from the ^6Li target to the exit face of the rear E counter (for the rear telescope at its furthest distance from the target). These values yield,

$$\Delta\Omega^*_S / \Delta\Omega^*_R < 2.2 \times 10^{-3}$$

thus justifying the omission of multiple-scattering.

Another uncertainty that arises in the Monte Carlo estimation of $\Delta\Omega_{eff}$ is due to the fact that the calculation only considers those rays that traverse the entire E counter. That is, the rays that enter the E counter, but exit through the sides, are excluded from the calculation. The ^{3}He nuclei following these trajectories, while perhaps not stopping in the E counter, may generate enough scintillation light output to be registered as a valid event. The maximum percentage of such ^{3}He trajectories was estimated using an A/r^2 approximation for the geometric solid angle of the front E counter. The entrance face of this counter has an approximate geometric solid angle,

$$\Delta\Omega'_F = (8 \times 30) / (50.2)^2 = 95.2 \text{ msr}$$

where the finite thickness of the ^{6}Li target, the polyethylene bag and the aluminum wrapping are neglected. The approximate geometric solid angle of the exit face is,

$$\Delta\Omega'_R = (8 \times 30) / (52.74)^2 = 86.3 \text{ msr}$$

The maximum percentage of the ^{3}He nuclei that enter the E counter, but exit from the sides, and generate a light output that could be counted in the experiment is,

$$((\Delta\Omega'_F - \Delta\Omega'_R) / \Delta\Omega'_R) \times 100\% < 11\%$$

This is treated as an asymmetric systematic uncertainty.

APPENDIX C

π^+ Beam Normalization Using ^{11}C Activation

Chapter 3 discussed the two methods of pion flux measurement used for calibrating the $(\mu_1 \cdot \mu_2)$ telescope : direct pion counting and ^{11}C activation. In this Appendix, the details of the ^{11}C activation technique are briefly reviewed.

In this method, a ^{12}C sample is irradiated by a π^+ beam for a set period of time (usually about five minutes). The number of ^{11}C nuclei produced via either the neutron knock-out reaction, $^{12}C(\pi^+,\pi^+n)^{11}C$, or the pion absorption, $^{12}C(\pi^+,p)^{11}C$, is measured and the number of pions required to create this amount of ^{11}C is then estimated.

A 0.635 cm thick and 5.08 cm diameter plastic scintillator (CH_{1104}) disk was used as the ^{12}C target and was placed perpendicular to the beam at the ^6Li target position. The disk's diameter was larger than the typical 3.5 cm diameter beam spot size. The number of ^{11}C nuclei produced from ρ ^{12}C nuclei/cm^2 at the end of an exposure time, t_E, is,

$$Q_0 = I_0 \rho \sigma \tau (1 - \exp(-t_E/\tau)) \qquad (C.1)$$

where I_0 is the average rate of pions incident on the target

during t_E, σ is the total cross section for $^{12}C(\pi,X)^{11}C$ and τ is the ^{11}C decay time constant. After the irradiation, the number of ^{11}C nuclei decays exponentially,

$$Q(t) = Q_0 \exp(-t/\tau) \tag{C.2a}$$

where t is the post-irradiation time. The number of disintegrations in a time period starting at $t = t_0$ and ending at $t = t_1$ is,

$$\Delta Q(t_0,t_1) = Q(t_0)\cdot(1 - \exp(-(t_1-t_0)/\tau)) \tag{C.2b}$$

In a calibration facility at TRIUMF, the ^{11}C activity of the disk is measured for a period of about an hour in time intervals of $(t_1 - t_0)$ seconds and a plot of the activity is fit to equation (C.2b), yielding Q_0. Equation (C.1) is then used to calculate the pion average beam rate, I_0.

^{11}C is a β^+-emitter with a decay time constant of τ = 29.344 minutes. The cross sections for $^{12}C(\pi,X)^{11}C$ used in equation (C.1) are from Dropesky, et. al. [1979], and Butler, et. al. [1982], and the post-irradiation activity Q(t) is measured using the β-γ coincidence method described by Ramsberg [1967].

The scintillation, within the disk, from a β^+ produced from a decaying ^{11}C nucleus is detected directly by a photomultiplier tube, yielding C_β counts in $(t_1 - t_0)$ seconds. This positron annihilates with an electron and

generates two 511 keV photons, one of which is detected by a NaI crystal that is isolated from the scintillator disk by a light-tight copper cap. This γ-ray detector yields C_γ counts in $(t_1 - t_0)$ seconds. $C_{\beta\gamma}$ is the number of β-γ coincidences during this time interval. These count rates are related to $Q(t_0)$ via,

$$C_\beta = k_\beta \, Q(t_0) \, (1 - \exp(-(t_1 - t_0)/\tau)) \qquad \text{(C.3a)}$$

$$C_\gamma = k_\gamma \, Q(t_0) \, (1 - \exp(-(t_1 - t_0)/\tau)) \qquad \text{(C.3b)}$$

$$C_{\beta\gamma} = k_\beta k_\gamma \, Q(t_0) \, (1 - \exp(-(t_1 - t_0)/\tau)) \qquad \text{(C.3c)}$$

where k_β and k_γ are the β and γ detection efficiencies. From these counts, $Q(t_0)$ is found independently of these detection efficiencies,

$$Q(t_0) = (C_\beta C_\gamma / C_{\beta\gamma}) / (1 - \exp(-(t_1 - t_0)/\tau)) \qquad \text{(C.4)}$$